

PONTIFICIA UNIVERSIDAD CATÓLICA DEL PERÚ

Escuela de Posgrado



Design, implementation and characterization of an Optical Coherent Tomography system based on a swept infrared laser source for the structural and biomechanical measurement of ocular and skin tissues.

Tesis para optar el grado académico de Maestro en
Física Aplicada que presenta:

Roger Agustin Valencia Rivera

Asesor:

José Fernando Zvietcovich Zegarra

Lima, 2025

Informe de Similitud

Yo, **José Fernando Zvietcovich Zegarra**, docente de la Escuela de Posgrado de la Pontificia Universidad Católica del Perú, asesor de la tesis titulada “Design, implementation and characterization of an Optical Coherent Tomography system based on a swept infrared laser source for the structural and biomechanical measurement of ocular and skin tissues” del autor **Roger Agustin Valencia Rivera**, dejo constancia de lo siguiente:

- El mencionado documento tiene un índice de puntuación de similitud de 8%. Así lo consigna el reporte de similitud emitido por el software *Turnitin* el 24/04/2025.
- He revisado con detalle dicho reporte y la Tesis o Trabajo de Suficiencia Profesional, y no se advierte indicios de plagio.
- Las citas a otros autores y sus respectivas referencias cumplen con las pautas académicas.

Lugar y fecha:

San Miguel, 24 de abril de 2025

Apellidos y nombres del asesor: <u>José Fernando Zvietcovich Zegarra</u>	
DNI: 45303268	Firma 
ORCID: 0000-0003-2467-4168	

Resumen

El queratocono y el cáncer de piel son enfermedades que afectan los sentidos de la vista y el tacto. El queratocono comienza como un trastorno refractivo, que puede causar ceguera si no se trata a tiempo. El cáncer de piel es mortal en pocos casos, pero puede afectar la calidad de vida de las personas si no se trata en etapas tempranas. Estas dos enfermedades pueden tratarse, con muy buenos resultados, si el tratamiento se inicia en estadios tempranos. Actualmente el queratocono se diagnostica mediante el análisis de deformaciones en la topografía corneal. El cáncer de piel en sus primeras etapas, se diagnostica mediante el método de inspección ABCDE, un examen visual que clasifica los lunares según su topología y apariencia. Algunos estudios demuestran que, para el queratocono y el cáncer de piel, las propiedades biomecánicas cambian antes de que se vea afectada la morfología. Para detectar estos cambios, se puede utilizar la elastografía. Teniendo en cuenta las dimensiones de los ojos y la piel, y el hecho de que las áreas afectadas en las primeras etapas son muy pequeñas, la técnica de imagen utilizada para este tipo de diagnóstico debe tener una resolución micrométrica y, además, ser capaz de adquirir imágenes en un par de segundos. La Tomografía de Coherencia Óptica cumple estas condiciones y añade características como la obtención de imágenes de capas profundas. No solo es posible mapear y trazar la topografía de la superficie del tejido, sino también capas más profundas (hasta aproximadamente 1 mm). Esta tesis abarca el proceso de diseño e implementación de un sistema de Tomografía de Coherencia Óptica de Fuente de Barrido que puede utilizarse para la elastografía por ultrasonido.

Abstract

Keratoconus and skin cancer are diseases that affect the senses of sight and touch. Keratoconus starts as a refracting disorder, but can cause blindness if not treated early. Skin cancer only treads life in few cases, but it can affect people's quality of life if not detected at earlier stages. These two diseases can be treated with very good results if treatment starts as early as possible. Currently, keratoconus is diagnosed by analyzing deformations on corneal topography. Skin cancer at the first level is diagnosed using the ABCDE screening method, a visual examination that classifies moles according to their topology and appearance. Some studies show, for keratoconus and skin cancer, that biomechanical properties change before the morphology is affected. In order to detect these changes, elastography can be used. Taking into account the dimensions of the eyes and skin and the fact that affected areas in the early stages are very small, the imaging technique used for this type of diagnostic must have a resolution in the order of micrometers and also be able to acquire images in a couple of seconds. Optical Coherence Tomography fulfills these conditions and adds features such as deeper layer imaging. Not only can the tissue surface topography be mapped and traced, but also deeper layers (up to 1 mm approximately). This thesis covers the design and implementation process for a Swept Source Optical Coherence Tomography system that can be used for ultrasound elastography.

Acknowledgments

I would like to thank my family for their continuous support and understanding. To my mother, I cannot be who I am without you. To my sister and brothers, you made me keep moving forward. To my nieces and nephews, I hope I meet your standards. To my wife, you showed me a new life. To my daughter, I am nothing without you.

My special appreciation to my professor and advisor, Dr. Fernando Zvietcovich. His patience and understanding helped me achieve one of my dearest and longest desires. Thanks to the GiBio group members, I have learned things from every conversation we have had.

To my Applied Physics professors, thanks for all the knowledge you shared, for the understanding and dedication you placed in your classes; it helped me a lot.

Finally, thanks to all the people I had the opportunity to meet during this stage of my life. It has been a pleasure and a privilege.

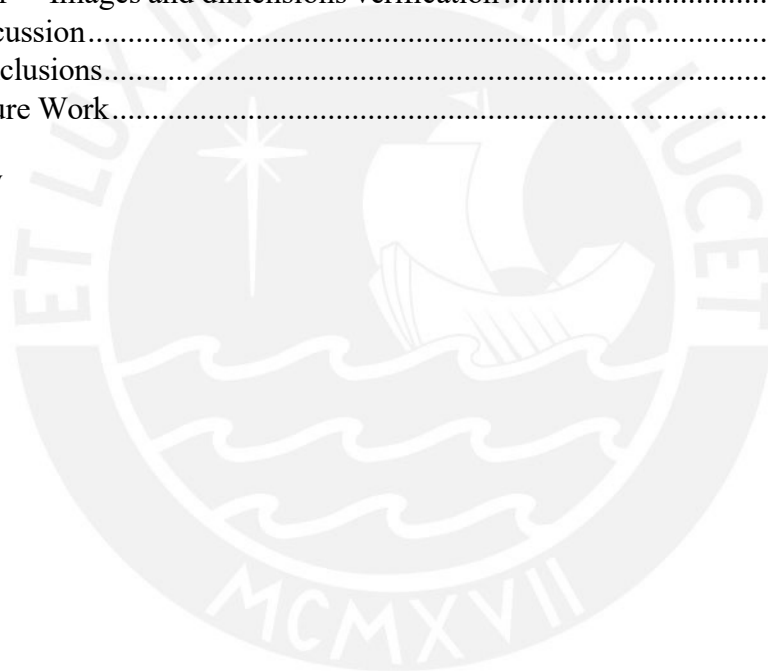
This work was funded by CONCYTEC through the PROCIENCIA program under the competition E041-2023-02 "Applied Research Projects 2023-02", according to the contract PE501082168-2023 "Development of the first coherent optical tomography system with elastography in Peru for the early detection of Keratoconus and other ocular diseases"

Contents

Resumen	ii
Summary	iii
Acknowledgment	iv
Contents	v
List of Figures	viii
List of Tables	xxii
I Introduction	1
1.1 Problem Statement	3
1.1.1 Keratoconus	3
1.1.2 Skin cancer	5
1.2 State of the Art	8
1.2.1 Clinical standard for diagnosing keratoconus	8
1.2.2 Clinical standard for diagnosing skin cancer.....	11
1.3 Proposal	14
1.4 Objectives	15
1.4.1 General Objective.....	15
1.4.2 Specific Objectives.....	15
1.5 Scope and limitations	15
1.5.1 Scope.....	15
1.5.2 Limitations	16
1.6 Expected Results.....	16
II Theoretical Background	17
2.1 Optical Coherence Tomography (OCT).....	17
2.1.1 Optical Coherence	18
2.1.2 Time Domain OCT.....	20
2.1.3 Spectral Domain OCT.....	24
2.1.4 Swept Source OCT.....	27
2.2 Optical Coherence Elastography (OCE)	31
2.3 Acquisition Modes and Protocols	32
2.3.1 B-mode Acquisition	32

2.3.2	M-mode Acquisition	33
2.3.3	MB-mode Acquisition.....	33
2.4	Data processing.....	34
2.4.1	DC Removal.....	35
2.4.2	Remapping on k-domain (k-linearization)	36
2.4.3	Windowing.....	37
2.5	Scanning patterns.....	37
III System Design and Implementation		39
3.1	Design Considerations	39
3.1.1	Parameters Selection	39
3.1.2	Light Source Selection	40
3.1.3	Interferometry Array	42
3.1.4	Photodetector	44
3.2	OCT Design	44
3.2.1	Interferometer	45
3.2.2	Reference Arm	46
3.2.3	Sample Arm	49
3.2.4	Optical Path Length (OPL)	52
3.2.5	Acquisition and processing	52
3.2.6	Embedded Acquisition Devices	54
3.2.7	Synchronization	55
3.2.8	OCT Design Results	58
3.3	OCT Design Adjustment	59
3.3.1	Modified Design Results	61
IV System Characterization and first images		62
4.1	Alignment	62
4.1.1	Reference Arm Alignment	62
4.1.2	Sample Arm Alignment	63
4.1.3	Working Distance	64
4.2	OCT Characterization	64
4.2.1	Lateral Characterization	65
4.2.2	Depth Characterization	69
4.2.3	Axial Depth Adjustment	71
4.2.4	Lateral Resolution	71
4.2.5	Axial Resolution	72
4.2.6	Axial Depth Range	73
4.2.7	Roll-Off	73
4.2.8	Sensitivity - Signal to Noise Ratio (SNR)	74
4.2.9	Optical Power Safety	74
4.3	OCT Images	75
4.3.1	Glass slides	75
4.3.2	Synthetic Model Eye	76

V	Results and Conclusions	78
5.1	Results	78
5.1.1	Requirements	78
5.1.2	Design	78
5.1.3	Implementation	78
5.2	System characterization summary	79
5.2.1	Lateral Characterization	79
5.2.2	Depth (axial) characterization	79
5.2.3	Axial maximum depth.....	79
5.2.4	Roll-off.....	79
5.2.5	Sensitivity - Signal-to-noise ratio (SNR)	79
5.2.6	Axial Resolution.....	80
5.2.7	Summary Table	80
5.3	OCT Images.....	80
5.3.1	Images and dimensions verification	81
5.4	Discussion.....	81
5.5	Conclusions.....	82
5.6	Future Work.....	82
	Bibliography	83



List of Figures

1.1	Parts of a human eye. Image taken from "Natural Eye Care" [6]	3
1.2	Figure (a) shows the optic configuration for distant objects; the lens has a "thin" configuration. Figure (b) shows a near object configuration, like the one used for reading; in this scenario the lens has increase its thickness.	3
1.3	Normal and most common refractive errors eyes. Figure (a) shows a normal vision case. Figure (b) shows a myopia case; images are formed before reaching the retina. Figure (c) shows a hyperopia case; images are formed after the retina. Figure (d) shows an astigmatism case; images reach the retina, but there are not correctly formed - Myopia and hyperopia can be caused by an abnormal eye length or by abnormal cornea or lens shape. Astigmatism can be caused by abnormal cornea or lens shape.	4
1.4	Left picture shows a normal eye. The right picture shows an eye affected by keratoconus. The cornea thickness is thinner than the normal ones; also, the shape of the keratoconus affected cornea becomes steepened - Image taken from "Dupage Optical" [7]	4
1.5	Chemical, mechanical and biological protection provided by the skin - Image taken from "Trucos de Belleza" [8].	5
1.6	Depth penetration by UV type. Type A penetrates up to the deepest layers of the dermis, while type B only reaches the epidermis - Image taken from "Radiacion UVA y UVB: La Importancia de la Proteccion Solar" [9].	5
1.7	Peruvian Cancer Distribution in the first quarter 2022 - Image taken from "Sala Situacional del Cáncer en el Perú, January-April 2022" [13].	6
1.8	Punch biopsy consist in extracting a section of the skin tissue with a special probe. Figure shows the punch biopsy procedure which requires a special probe to extract a small section of the skin. The surface area is not significant, but it can go up to 4mm deep. The affected area can take up to 2 months for full recover. This procedure is required after a health professional executes the ABCDE screening procedure and is the final diagnostic exam. A non-invasive diagnostic tool that can display and analyze the affected area without the need of removing it from the patient may help physicians as well as allow patients to continue their normal lives - Image taken from "Melanoma Treatment (PDQ®)–Patient Version" [14]	7

1.9	Cancer stages depth. The higher the stage is, the deeper the affected tissues spread. Earlier stages affect only epidermis, but later ones can go up to the dermis layer with almost 4 mm depth. Melanoma presents itself in melanocytes, cells that provide color to the skin. Other skin cancer types can also present in squamous and basal cells; these two are called Non-Melanoma Skin Cancer. In order to identify earlier stages of skin cancer, the most superficial epidermis layers need to be analyze. - Image taken from "Melanoma Treatment (PDQ®)–Patient Version" [14]	7
1.10	Placido disc projection in an eye. The projection of concentric circles over the corneal are analyzed to evaluate its optical properties. Abnormal formations in the cornea surface will produce different patterns; the closer the rings the more pronounced the inclination. The flatter the cornea, the wider the rings will be. - Image taken from "Corneal Topography" [17]	8
1.11	Figure (a): Placido disc eye ring pattern reflection from a normal eye. Figure (b): Placido disc eye ring pattern reflection from a keratoconus eye. This method cannot detect small deformations and can be deceived by other disorders like stromal ulcers and epithelial defects as they will produce abnormal reflection - Image taken from "Corneal Topography" [17].	9
1.12	Parallel Slit scanning technique performed by an Orbscan system - Image taken from "Corneal Topography" [17].	9
1.13	Figure (a) shows how an Oculus Pentacam system takes 20 meridian scans (each rotated 9° degrees) to cover the cornea. Figure (b) shows the system processing the 20 scans information gathered, analyzing their reflection, in order to create a surface and thickness map. Figure (c) shows the system extrapolating a topology map by combining all the scans.	9
1.14	A Zeiss Cirrus HD-OCT was used to scan the eye anterior side. Figure (a) shows the Chamber view. Figure (b) shows a high definition corneal image. Figure (c) shows a detail view of the lens and iris. Image taken from "Cirrus HD-OCT 5000/50 booklet"[19].	10
1.15	Figures (a) and (b) show air puff stimulus applied to an <i>in vivo</i> human cornea with a crosshair pattern. Figure (a), the green section, corresponds to the horizontal scan at two moments; at rest state and the bottom one when the air puff caused its maximum deformation. Figure (b), the orange section, shows the same two conditions but on the vertical scan. OCT can also display the transition from rest to maximum deformation and vice-versa. Figures (c) and (d) were taken using an <i>ex vivo</i> porcine eyes; one of them was artificially modified to mimic a keratoconic eye. Figure (c) shows the analysis performed on the normal eye. Figure (d) shows the same analysis performed in the keratoconic eye. - Images adapted from "Multi-meridian corneal imaging of air-puff induced deformation for improved detection of biomechanical abnormalities" [20].	10
1.16	Figure (a) shows the ABCDE screening performed by a health professional, using an amplifier tool. Figure (b) shows the table used to identify melanoma from normal moles. - Images taken from "Skin Cancer Foundation" [22].	11

1.17	For Histology exams the extracted tissue is laminated, placed in a slide and colored to identify cancer cell morphology. Sampled tissues are colored and examined under microscope. Cell morphology will reveal abnormal cell formations and its quantity. Figure shows different types of anomalous cells like squamous cell carcinoma and sebaceous tumors - Image taken from "Dual Role of Inactivating Lef1 Mutations in Epidermis: Tumor Promotion and Specification of Tumor Type" [23].	12
1.18	Sub-figure A shows a Basal Center Carcinoma section; fat white arrows mark the BCC border while the thin white arrow points to a necrotic center. Sub-figure B shows a Polarity-Sensitive OCT (PS-OCT) from a portion of the same area. Sub-figure C shows a normal skin image and sub-figure D shows a PS-OCT capture; the black bar is the same area in C and D - Images taken from "Assessment of Optical Coherence Tomography Imaging in the Diagnosis of Non-Melanoma Skin Cancer and Benign Lesions Versus Normal Skin" [25].	12
1.19	Air puff OCE system. A Thorlabs LSM54-1310 scan lens is used for the optical components. Below the lens a conical structure allows air puff to hit the skin without obstructing the optical axis. Two samples were scanned, a healthy sample at the top (Control) and an illd one (a case of Systemic sclerosis skin) at the bottom. Scanned images show the skin structure obtained with OCT and small sections located at the bottom right corner show the wave propagation. Image taken from "Translational optical coherence elastography for assessment of systemic sclerosis" [26].	13
1.20	Diagnose Confusion Matrix shows the possible outcomes for ABCDE screening.	13
1.21	OCT has between 2 to 10 μm resolution with a penetration of up to 1 or 2 mm; this resolution provides enough details of corneal tissues and skin. 1 mm penetration covers the whole cornea thickness; it provides the depth required to locate stages 0 and I skin cancer cases. Ultrasound, high resolution CT and MRI does not have the resolution to generate corneal images. Confocal microscopy has better resolution than OCT, but it can only penetrate tissues a couple of hundreds micrometers. [28].	14
2.1	Figure (a) shows a cross section image from a skin sample (2D image). Figure (b) shows a volumetric image, created by multiple cross sectional images from the same skin sample (3D image) - Images taken from "A measurement of epidermal thickness of fingertip skin from OCT images using convolutional neural network" [29].	17
2.2	OCT principle is that light will be refracted in a different speed due to its refractive index (n_x). Figure (a) shows a skin diagram receiving an incident light beam. This beam will be, partially, reflected and dispersed (backscattered); the rest will be transmitted (refracted) through this layer until it reaches the following one. This behavior repeats until the intensity is completely absorbed by the tissues - Image modified from "Skin and its histology applied" [30]. Figure (b). As the incident light beam travels through each layer of the tissue, backscattered beams will be generated, each one of them attenuated compared to the previous one. Each backscattered beam will be delayed to the ones generated in upper tissue layers.	18

2.3	Spatially dependent interference pattern caused by a single wavelength (high coherence).....	18
2.4	Figure (a): An interference pattern created by eight slightly different wavelength (λ_1) signals (1% difference). Figure (b) shows interference patterns created by 16 different wavelength signals. Figure (c) expands the number of signals to 50. The resultant temporal coherence interference signal has a pronounced amplitude and a Gaussian shape.	19
2.5	Figure (a) shows a pattern with $g_{(\tau)} \approx 1$. Figure (b) shows a low coherence pattern. Their coherence periods have the following relation $\tau_{c(a)} > \tau_{c(b)}$	19
2.6	Time Domain OCT basic diagram. The mobile mirror identifies these types of system. Other techniques use a fixed mirror on the reference arm.	20
2.7	TD-OCT diagram and variable definition for interference calculation.	21
2.8	When a low coherence light source is used, one interference signal results when the Optical Path Lengths (OPL), reference and sample, are the same. These three interference signals correspond to sample layer 1, Figure 2.7 Z_{S_1} , layer 2 to Z_{S_2} and layer 3 to Z_{S_3} ; these signals were captured when the reference mirror was displaced along its axis. l_c stands for length of coherence and corresponds to the distance over which the wave maintains its coherence. It is measured at half the maximum (Full Width Half Maximum).....	21
2.9	OCT system are characterized by the lateral and axial field of view and the lateral and system resolution. These parameters depend on the light source and the sample scan lens parameters like, wavelengths and Numeric Aperture (NA) - Image taken from "Optical Coherence Tomography Technology and applications"[32].	24
2.10	Spectral Domain OCT diagram. The reference mirror is now not mobile.	24
2.11	Basic SD-OCT schematic with a Michelson Morley interferometer. The detector array (a CCD camera) with an N number of bins to receive an N number of wavelengths - Image taken from "Introduction to OCT"[28].....	25
2.12	SD-OCT Interference. Each sample layer reflects the light beam from a different depth as shown in figure 2.2.....	25
2.13	Swept Source OCT diagram. Spectrometer and CCD camera are replaced by a photo-detector and a swept source laser.....	27
2.14	Swept Source OCT system basic schematic diagram. Two fiber couplers (bidirectional beam splitters) and two circulators are used to configure a Mac-Zehnder interferometer schema. With this arrangement the first fiber coupler is used to split the swept source beam, one for reference and the other for the sample, and the second one is used to combine (interfere) signals from reference and sample. SS - OCT requires a synchronization with the computer to acquire the scanned information at the swept start - Image taken from "Wave-based optical coherence elastography: the 10-year perspective" [33].....	28
2.15	SS-OCT Interference. Each sample layer reflects the light beam from a different depth as shown in figure 2.2.....	29

2.16	Figure (a) shows an OCE system analyzing a tissue. The OCT probe (red rays) is responsible for capturing the tissue structure and its response to the mechanical stimulus (green rays). The tissue receives the mechanical waves and propagate it through the axial (Z) and lateral (X) axes. Figure (b): From the cross section scan obtain in figure (a), an horizontal (X) section is analyzed at a specific moment (t_0). Figure (c) analyzes the same (X) section from figure (b), but in a time period. With this information a speed map can be generated - Image taken from "Wave based OCE the 10 year perspective" [33].	31
2.17	On this OCE Prototype air puff module (yellow arrow) has an aperture that let the optical axis (red arrow) from the OCT scanning lens (green section) reach the eye; besides the optical-air puff confocal alignment, the air stimulus has to be synchronized with the OCT data capture process so the system can generate images for the complete tissue movement. This arrangement is used, also in other elastography-OCT systems - Image taken from "Multi-meridian corneal imaging of air-puff induced deformation for improved detection of biomechanical abnormalities" [20].	31
2.18	Ultrasound OCE Lens Array - Image taken from "Confocal air-coupled ultrasonic optical coherence elastography probe for quantitative biomechanics" [34].	32
2.19	B-Scan on a tissue - Image adapted from " Wave-based optical coherence elastography: the 10-year perspective" [33].	32
2.20	M-Mode Acquisition - Image taken from "Wave-based optical coherence elastography: the 10-year perspective" [33].	33
2.21	M-Mode Analysis. From the multiple A-scans obtained, we can calculate the inverse of the wave velocity by calculating the pendent between the time period and the distance difference Δz in the same period. The image is generated with colors based on the color bar assumed - Image modified from "Wave-based optical coherence elastography: the 10-year perspective" [33].	33
2.22	MB-Scan - Image taken from "Wave-based optical coherence elastography: the 10-year perspective" [33].	34
2.23	MB-mode acquisition scan process - Image taken from "Wave-based optical coherence elastography: the 10-year perspective" [33].	34
2.24	Figure (a) shows an interference signal, from a cornea, captured by an OCT system. Figure (b) shows the image generated from the interference signal, using the Fourier Transform (generating a mirror image).	35
2.25	Figure (a) shows the calculated DC component (in yellow). After subtracting DC from the raw signal, the interference is showed at the bottom of that figure. Figure (b) shows the new image from the data without the DC component and without the mirror image.	35

2.26	k-linearization process: from λ domain to k domain. Figure (a) shows the interference spectrum captured by an oscilloscope. The signal runs in time domain. Wavelengths are also equally distributed in time; the correspondence between wavelength and wave number is provided by equation $k = \frac{2\pi}{\lambda}$. The k value for each sample is not equally distributed. Figure (b): From Intensity equation 2.18, the Intensity at the detector depends on wave number (k), not in wavelength domain. A regular k distribution is required, an interpolation can be applied.....	36
2.27	K-linearization example. $k_1, k_2, k_3, \dots, k_n$ have an irregular distribution. After the signal is interpolated, a new set of k values are generated ($k'_1, k'_2, k'_3, \dots, k'_n$) .	36
2.28	Figure (a) shows the image generated from the raw data. Figure (b) shows the image generated from the processed data (DC subtraction, k remapping and windowing).	37
2.29	Voltages applied to X and Y mirrors to create a Crosshair scan pattern. Blue line shows the voltage pattern applied to the X-axis mirror. Red line corresponds to the Y -axis mirror. The synchronization clock (yellow pattern), indicates the mirror movement duration as well as the sample data acquisition (green pattern).	37
2.30	Figure (a) show the result for the applied voltage pattern on figure 2.29. Figure (b) shows the same pattern applied from the system on an IR detector Card. The transition lines, showed as dotted in figure (a), are not taking in consideration for image processing.	38
2.31	Figure (a) shows the scan pattern for a 3D image. Figure (b) shows a bright red line at the top of a dark rectangular section on the IR detector card . This IR card becomes a dark after an IR beam is received; the dark rectangular section was hit by the IR line beam one line at a time.	38
3.1	OCT/E System Block Diagram showing its main components, sample and reference arm, beam splitter, mixer, photo-detector, acquisition and processing and the elastography module.	39
3.2	The optical window figure shows the light absorption caused by the principal components of biological tissues - Melanin and oxyhemoglobin(HbO_2). Around 1300 nm the absorption from the biological tissue components is minimum. At the same time, the water has a relative absorbance between 1 and 2. Longer wavelengths have higher absorbance - Image modified from "Effect of wavelength and beam width on penetration in light-tissue interaction using computational methods"[35].	40
3.3	A source emits a light beam (red) that is splitted in two by a beam splitter (O). One of the new beams (blue) goes to mirror 1 (M_1) where it is reflected back; this beam and its reflection travels through a compensator block (C) in order to compensate the beam splitter thickness traveled by the second created beam (pink). This second beam travels to mirror 2 (M_2) and then it is reflected back to the interferometer through which it will reach the detector (D). If the distances to mirrors M_1 and M_2 , positive interference patterns will be created at the detector (in this case concentric circles) - Image modified from "Optics - Fifth edition"[37]	42

3.4	The source (red) is splitted in two light beams. One of the new beams (pink) goes to one mirror and then it reaches a second beam splitter that serves as a combination arrangement. The other light beam (blue) goes to the second mirror and then to the last beam splitter to be combined with the other light beam - Image modified from "Optics - Fifth edition"[37].....	43
3.5	Thorlabs Fiber Optic Coupler Flow. This coupler has a bidirectional configuration with two ends at each side; they can be used in both directions. The center wavelength must match the source laser (1300 nm) as well as its connectors type - Image adapted from "Thorlabs web site" [36].	43
3.6	Thorlabs PDB480-AC External Dual Balanced Photo-detector - Image taken from "Thorlabs web site" [36].	44
3.7	OCT design using a swept laser source and a Michelson interferometer array. An Optic circulator is being used as an isolator to protect the laser source from back-reflection coming from the reference arm. Fiber coupler described in figure 3.5 are used as fiber couplers 1 and 2.....	44
3.8	OCT system sections. The interferometer section, composed by the Fiber Coupler 1 is enclosed in the pink section. The reference arm is enclosed in the green section; it is composed by a collimator, a mirror and a focus lens. The sample arm, enclosed in the orange section, is composed by a scanning lens, a dual mirror galvanometric system and a collimator. The detection section, enclosed by a yellow square, is composed by a Dual Balanced photo detector and the fiber coupler 2.	45
3.9	Fiber Coupler 1 is used as a Michelson interferometer with a 50:50 beam splitter. The laser source is connected to port 1 (left white leg) and the light flow is divided towards the reference arm, via port 4 (right red leg) and to the sample arm, via port 3 (right white leg). The backscattered light, from the sample, comes from port 3 and is directed to left ports 1 and 2. The reference reflection comes in port 4, and is also directed to the same left ports. The interference signal, from sample and reference, is created by the reference and sample mixture and divided by the fiber coupler; the resulted beams are sent to ports 1 and 2 (white and blue) - Image adapted from Thorlabs [36].	45
3.10	Reference Arm Length. The light beam from the laser source is divided in two paths; one is sent to the reference arm and the second one to the sample arm. Both light beams have to travel the same length in order to produce a detectable interference signal. As the fiber coupler has the same length for its 4 legs, the reference arm has to match the sample length. For this design, the reference arm can be set from 130 mm to 390 mm in length. The dispersion compensator refraction index (n) was not considered in the calculation due to its short length.	46

3.11	Reference arm composed by a collimator, a focusing lens and a mirror. The key component in the Reference arm is the distance between the collimator and the mirror that will be used to compare the sample back-scattered light; this length can be set from 130 mm up to 390 mm. The collimator receives the light beam from the Fiber Coupler 1, red port, and send it to the mirror; in theory only those two components are required, but the collimator does not have a perfect alignment with the mirror center. That is why a focusing lens was included, to concentrate the light beam into a single spot in the mirror. The mirror tilt can be adjusted to reflect the beam back to the mirror with the same angle or with a little tilt; this will cause that the reflected beam will not have the maximum intensity.....	47
3.12	A focus lens is used to center the light beam into the mirror. Figure (a) shows the Thorlabs AC254-100C Doublet achromatic lens dimensions. Figure (b): AC254-100C facilitates the focusing of the light beam. Since the collimator has to be slipped to match the sample optical path length and also to characterize the system, a translation stage is used as the collimator support. This arrangement adds additional level of complexity to the collimator-mirror alignment. During the implementation it was not possible to get a proper alignment. Using the focus lens, the light beam reached the center of the mirror due to its centering properties - Images taken from "Thorlabs web site"[36].....	47
3.13	Figure (a): Collimator. Figure (b): Translation stage. Figure (c): Collimator (a) mounted on the translation stage (b). Figure (d) Dispersion compensator block. This block has a glass lens arrangement that creates the same first and second order dispersion as the scan lens LSM05 located at the sample arm - Images (a), (b) and (d) taken from "Thorlabs web site"[36].	48
3.14	Figure (a): Reference Mirror; Thorlabs PF10-03-P01 protected silver mirror was selected to complete the reference arm. This mirror has a 25.4 mm diameter, a 22.9 mm clear aperture and a surface flatness of $\lambda/10$ at 630 nm. Figure (b): The mirror is mounted in a Thorlabs KC1/M kinematic 30 mm cage that allows the mirror to be oriented in a vertical/horizontal direction. This arrangement allows the reflected light beam to be directed to a specific direction, the focus lens. Each of its three adjusters provide up to $\pm 5^\circ$ angular displacement and up to ± 3 mm total translation displacement - Images taken from "Thorlabs web site"[36].....	48
3.15	Sample Arm Length. The light beam from the laser source is divided in two paths; one is sent to the reference arm and the second one to the sample arm. Both light beams have to travel the same length in order to produce a detectable interference signal. As the fiber coupler has the same length for its 4 legs, the sample arm has to match the reference length. For this design, the sample arm length is set to 328.8 mm. This length was in the reference arm length range (130 390 mm). The scanning lens refraction index (n) was not considered in the calculation due to its short length.....	49
3.16	Sample Arm components: scanning lens, galvanometric mirror system and collimator mounted on an X-Y translation cage.	49

3.17	Figure (a): Telecentric properties for the scanning lens allows the light beam to reach different sample areas, keeping their back-scattered signals parallel to the optical axis. In this diagram the entrance pupil is called scanning distance and it is located between the 2 mirrors that are part of the galvanometric system. Figure (b): Telecentric scanning lens Thorlabs LSM05. This lens was selected considering that its wavelength range matches the swept laser source and that its working distance provides the necessary space to accommodate an elastography module; also its lateral field of view covers the design requirement (Table 3.1) - Image (b) taken from "Thorlabs web site" [36].	50
3.18	To scan superficial areas, the light beam has to be moved using specific patterns. These patterns are applied to a galvanometric system that has two mirrors; the bottom mirror controls the X axis movement while the upper mirror controls the Y axis movement. The light beams from the galvo system arrive the scanning lens forming and angle to the optical axis; the lens transport these light beams parallel to the optical axis reaching the sample in parallel to the optical axis - Images modified from "Scannermax web site" [38] and "Thorlabs web site" [36].	51
3.19	Collimator, figure (b), mounted on a translation mount Thorlabs CXY1A, figure (a). This mounting block allows to place and direct the collimator within two axis, horizontal and vertical (with ± 1 mm), to align the light beam to the dual mirror galvo system. The collimator used in this section is the same as the one used on the reference arm, figure 3.13 (a) - Images modified from "Thorlabs web site" [36].	51
3.20	Optical Path Length Calculation. As the fiber coupler legs have the same length, we can remove them from the calculations. The Reference arm OPL can be set from 130 to 390 mm in open air. The Sample arm OPL has a fixed length of 328.8 mm in open air. As previously mentioned, the scanning lens and its dispersion compensating block have a different diffraction index (n), but this calculation was not considered due to its dimensions.	52
3.21	The interference signal, generated at the fiber coupler1, is sent to fiber coupler 2 to be divided in two identical signals but with half the amplitude each. These two identical signals are sent to a balanced photodetector that will subtract both signals to cancel the common mode noise. The resulting signal is converted into a electric signal that is captured by an oscilloscope. The photodetector must also use FC/APC connectors to be able to receive the fiber connections from the fiber couplers.	52
3.22	Figure (a) shows an infrared (IR) detector card, placed at the sample arm; the light beam can be spotted in the green circle. Figure (b) shows the interference signal (yellow) captured by the oscilloscope and its Fourier Transform (blue); In the red section two main frequencies can be identified. Figure (c) expands the red section; there are two main peaks that correspond to the IR card and its plastic cover	53

3.23	Figure (a); To start controlling the galvo system, two external power supplies were linked configured as ± 24 VDC. A 2-channel wave generator was also used to control the galvo mirrors (Rigol DG4162, arbitrary waveform generator). Figure (b) shows a linear scan pattern, known as B-scan pattern. This pattern is accomplish by controlling the bottom mirror; with a $2 V_{pp}$ signal with a 200 Hz frequency and a 10% symmetry sawtooth waveform. Offset and phase were set to $0 V_{DC}$ and 0°	53
3.24	The acquisition and processing is now performed by an Analog to Digital Converter embedded card. This card is controlled by a computer application, LabVIEW, that will also control the galvo system trough a second embedded card, a Digital to Analog Card.	54
3.25	Figure (a) shows an Alazartech ATS9364, an ADC with 2 channels (12 bits resolution each). Figure (b) shows a National Instrument NI6738, a DAC to control the galvo system - Images taken from "Alazartech web site" [39] and "National Instruments web site"[40].	54
3.26	Synchronization scheme. The light source provides the reference clock through the DAQ trigger; at the same time it provides a k-clock signal that will be used as reference to process the signal. The NI6738 start to control the galvo mirrors and sends an indication to ATS9364.....	55
3.27	OCT Synchronization Signals. DAQ trigger signal is the system reference (first pattern, pink signal). NI6738 generates a galvo start signal, also known as B-trigger, taking DAQ as reference (second pattern, purple signal). NI6738 starts controlling X-Y galvo mirrors (third pattern, red an blue). K-clok signal start begins at the same time as DAQ trigger (fourth pattern, yellow signal). ATS9364 marks the sample gathering from k-clock (fifth pattern, green signal). The interference spectrum is acquired at the ATS9364 (sixth pattern, vermilion signal).	55
3.28	Synchronization signals distribution. By using the k-clock signal from the laser source, the k-linearization process is not required. DAQ trigger is used by ATS9364 and NI6738 cards to elaborate control and acquisition signals.	56
3.29	LabView App Interface. Green section, shows the captured interference spectrum. On the same figure, red section, the the data is processed to show the sample image (a mirror).....	56
3.30	OCT design updated with the acquisition and control cards in a computer with a LabView application.....	57
3.31	Figure (a): A sample (mirror/glass/plastic) placed at the scanning (focal) point. Figure (b): the LabVIEW application generates a single line (the mirror surface) that represents every scanned point in the sample because every one of them has the same intensity. 300 sample points were scanned in a 10 mm length. Figure (c) shows the scanned image obtained from a coverslide, a glass surface. Figure (d) shows the scanned image obtained from a plastic ruler sample. The image from the plastic sample shows imperfections in its surfaces. All the generated images present curvatures even tough the scanned objects have flat surfaces; this deformation was caused by the processing application.	57

3.32	Figure (a) shows an infrared detector card at the scanning point. Figure (b) shows the image obtained from the IR card scan. This scan does not generate a usable image.	58
3.33	Figure (a) shows a generated image from a scanned glass. Figure (b) shows figure (a) interference signal analyzed by the LabVIEW application. Figure (c) shows a generated image from a scanned plastic eye using a crosshair pattern (horizontal and vertical). Figure (d) shows figure (c) interference signal. In both A-scan spectral datapoints analysis, the interference signal is not synchronized with the processing task.	58
3.34	OCT Design adjustment. The interferometer configuration changed from a Michelson configuration for a Mac-Zehnder one using an additional fiber coupler and an optic circulator.....	59
3.35	Figure (a) shows the Michelson interferometer configuration used in the original design; fiber coupler 1 port 2 is receiving signals reflected from reference and sample arms. Figure (b) shows the Mac-Zehnder interferometer configuration implemented in the system modification; there is no signal from sample arm on fiber coupler 1 port2, all the reflected intensity is sent to fiber coupler 3.....	60
3.36	OCT system with a Mac-Zehnder interferometer configuration. The additional fiber coupler has two purposes; to reduce the intensity reflected from the reference arm and to match the optical path length (OPL). OPL is the length the light travels on the reference arm and at the sample arm. Both have to be almost the same length in order to be able to generate images.....	60
3.37	IR Card image generated with the modified OCT system. This image has better intensity and can be analyzed.	61
3.38	Figure (a) shows a glass object scanned with a crosshair pattern; the horizontal and vertical images are perfectly aligned. Figure (b) shows an image from a plastic model eye, scanned with a linear (horizontal) pattern.	61
4.1	Reference arm components. The cubic stage (figure 3.11) was removed due to the OPL reduction on the second design. The dispersion compensating block was mounted in the translation stage, figure 3.13(b) forward face, back to back with the collimator. The focus lens, figure 3.12, is closed to the dispersion compensating block. As the laser beam has a 1300 nm wavelength, invisible for the human eye, infrared detector cards (IRC) were used to trace the beam.	62
4.2	Sample arm scanning Array	63
4.3	Sample arm alignment procedure. Figures (a) and (b) shows the route used by the laser beam through the mounting supports; the galvo system is mounted on top of two blocks, Thorlabs UBP2/M and BA2S7. Figure (c) shows the IR card, mounted on a metric rail, tracing the light beam elevation and lateral deviation. As the IR card "turns off" if the light beam remains on the same spot, two moving patterns were used to trace the center. An horizontal line pattern was used to verify the altitude remained the same. A vertical line pattern was used to verify the optical axis was maintain.....	63

4.4	The mirror mounted as a sample has the same characteristics as the one located at the reference arm. The mirror mounting bracket is, also, the same type as the one used at the reference arm; it has three adjusters (yellow circles in figure 4.4) that allows the mirror to displace the reflected light beam $\pm 5^\circ$	64
4.5	Figure (a): A metric hex key set used for the characterization procedure. Figure (b): The 2 mm hex key place vertically for the horizontal characterization procedure. A dichroic mirror was placed between the hex key and the scanning lens; this mirror is transparent for the light beam wavelength used ($\lambda = 1300\text{nm}$). ..	65
4.6	Hex Dimensions. In this case a 5 mm hex key was used to calculate the largest to the shortest diagonal relation (1.154). All the keys were used except the smallest one, because it was not possible to place it properly.....	65
4.7	5 mm hex key scanned image. Start and end sections are enclosed in red sections. ..	66
4.8	Zoomed in star and end pixels. Figure (a): the image starts on pixel 98 and ends on pixel 204, figure (b); its length, in pixels, is 106. Then 106 pixels are equivalent to 5.77mm or 1 pix = 54.43 μm (on a 15 mm section scan). The procedure was repeated with 15 mm, 12.5 mm, 10 mm, 7.5 mm, 5 mm and 2.5 mm scan ranges. The number of A-scans (pixels) per section scan was 300.....	66
4.9	Horizontal resolution chart. From table 4.2, the best resolution belongs to sampled lengths of 2.5 mm; a 5.53 $\mu\text{m}/\text{px}$. The scattered plot shows the correlation between resolution ($\mu\text{m}/\text{px}$) and scanning range.	68
4.10	Depth Characterization procedure. Figure (a) shows the mirror in this procedure; the scattering overloads the signal, causing a blurred and thick image. Using the adjusters (yellow circles) located on the mirror mounting bracket, the mirror is slowly tilted until a clear and well defined signal is visible in the image. Figure (b) shows the reference micrometer used to slide away the reference collimator. A full 360° turn slides the collimator 500 μm	69
4.11	As mirror is used as sample, the resultant image is a line that represents a single frequency. Figure (a): the start point selected was the closest to the OPL, without distorting the signal. Figure (b): the line was zoomed in to measure its thickness.	69
4.12	Image from the micrometer full rotation (500 μm).....	69
4.13	Figure (a): System depth limit. Figure (b): The micrometer used to slide the reference collimator.....	70
4.14	Figure (a) shows a slide measured with a caliper, providing a measurement of 1.14 mm deep. Figure (b) shows the scanned image from the same object; the surfaces are separates by 260 pixel that, using the value obtained in the procedure Depth Characterization 4.2.2, can be translated to 1.068 mm for glass with a refraction index (n) of 1.5. Figure (c) shows two adjacent slides measured with the caliper, with a 2.29 mm deep measurement. Figure (d) shows the scanned image that provides a 2.177 mm measurement.	71

4.15	Figure (a): 1951USAF Resolution Target by Thorlabs. The resolution is determined by the smallest group of recognizable parallel lines. Figure (b) shows the resolution target image scanned by the system; the smallest group of recognizable lines belongs to group 3, element 6. Figure (c) provides a 14.30 line pairs per millimeter (lp/mm). This means that the minimum line width resolution is 35 μm . - Figure (b) was generated with a MatLab script created by L.Barreto from PUCP GiBio [41]	71
4.16	The interference signal was captured three times with a separation of 500 μm . The second signal, the one with the higher amplitude, was used for the calculation; the other two were used to calculate the oscilloscope depth resolution.	72
4.17	A measurement was taken every 500 μm but instead of measuring pixels in the image, the spectrum signal was captured in .csv format using the oscilloscope application provided with the ATS9364 acquisition card and then processed with a MatLab script. All acquired files were named P01 to P16. P00 is a measured taken at the first point, just as P01, but with sample and reference arm covered; this file will be used in a following subsection.	73
4.18	Roll-off Chart. 13 measurements are displayed in the chart. The signals with the highest and lower amplitudes were used for the calculation.	74
4.19	An optical power meter, Thorlabs PM100D, was placed at the Sample arm. The value obtained was 5.33 mW, one third of the allowed power, according to the International Electrotechnical Commission (IEC) recommendation.....	75
4.20	Figure (a) shows a glass slide used as sample. A linear scanning pattern was used with 500 A-lines per B-scan. Figure (b) shows the image generated by the system; two lines corresponding to the anterior and posterior surfaces. An amplified view showed the anterior surface located at pixel 400 and the posterior surface located at pixel 660 (depth = 260 px).	75
4.21	Two slides scanned.....	76
4.22	Figure (a) shows a synthetic model eye. This model has the same dimensions as a real human eye and can be set to use in normal or diffraction error configuration. Figure (b) shows the eye set in normal configuration facing the scan lens. Figure (c) shows the OCT system scanning the synthetic eye.	76
4.23	Figure (a) shows a linear scan performed on the synthetic eye model. Corneas' outer and inner layers are well defined. The sclera, iris and lens are also displayed. Figure (b) shows a crosshair scan performed to the same sample. Crosshair scan pattern takes two linear scans shifted 90°. These two scan patterns were taken using 300 samples per line. At the center of each eye image, the scattered light becomes stronger, causing the brighter effect.	77
4.24	OCT image downloaded from the manufacturer's web site. The shape of the cornea matches the shape from Figure 4.23(a) - Image taken from Modell-Augen Manufaktur [42].....	77
5.1	Figure (a): One glass slide was measured; using the summary table, its thickness was 1.1 mm. Figure (b): Two glass slides were measured; using the same summary table as on figure (a), the total thickness was 2.2 mm.	80

- 5.2 Figure (a): OCT system generated image from a scanned synthetic eye model.
Figure (b): OCT's image, downloaded from the manufacturer web's site - Image
(b) Image taken from Modell-Augen Manufaktur [42]. 81



List of Tables

1.1	UV Classification [10]	6
3.1	System design requirements	40
3.2	Thorlabs SL132120 specifications [36]	42
3.3	Scanning lens technical specifications	50
4.1	Lateral Characterization Measures	66
4.2	Length resolution	68
4.3	Depth Characterization	70
4.4	Depth Resolution in air	70
5.1	OCT system parameters	80
0.2	Source Light	87
0.3	Reference Arm	87
0.4	Sample Arm	88
0.5	Interferometer	88
0.6	Mechanical	88
0.7	Tools	89

Chapter I

Introduction

The eyes and skin are responsible for the sight and touch senses, respectively; they provide the central nervous system with sensory information about the environment that is processed by the brain.

The cornea is the outer layer of the eye, a transparent tissue responsible for refracting the electromagnetic spectrum, especially the visible one (between 380 nm and 750 nm) towards the retina, passing through the lens. From an optical point of view, the cornea can be considered as a positive lens with a thickness of 500 to 600 microns thickness; that is why it is very important to maintain its structure and morphology.

Like any biological tissue, the cornea can be affected by external and internal elements that can reduce the quality of vision or, in the worst case, suppress it. One of these progressive conditions is keratoconus, a bulging and thinning of the cornea, which results in the degradation of the patient's visual capacity. This morphological change, the bulging, modifies the cornea's optical properties, affecting the eye's focal point; images are not formed at the retina. This deformation is also associated with changes in the structure and biomechanical properties.

Treatment for keratoconus depends on the stage of the disease progression. In the early stages, corrective lenses are used, as in the case of myopia. In intermediate stages, corneal crosslinking can be used. For later stages, surgical solutions are required, such as the introduction of intra-corneal rings or corneal transplants [1]. Considering that in our country 120 corneal transplants are performed per year, but 300 are not due to a lack of donors, it is clear that keratoconus patients will have a 70% probability of not receiving the transplant [2].

Keratoconus treatment, in the early stages, avoids traumatic and costly procedures. Considering that this condition appears between puberty and 35 years old[1], it becomes very important to detect it at early stages to apply treatments that can stop or slow down disease progression. Keratoconus detection is carried out by exams like:

- Corneal topography; a non-invasive, non-contact technique that produces a map of the superficial curvature of the cornea.
- Slit lamp test; a procedure that can detect morphological abnormalities in the outer and middle layers of the cornea.

-
- Pachymetry; an exam that measures the cornea's thickness.

All of these exams measure corneal morphology and thickness; detection requires that the cornea already presents a change in its surface, but some studies [3] indicate that the biomechanical properties had already changed before the morphology does. Identifying these biomechanical changes would allow the early detection of keratoconus before the structure or morphology of the cornea begins to change.

To detect the early stages of keratoconus, a technique capable of measuring the biomechanical properties of the cornea is required. [4]. Due to the sensitivity and fragility of the cornea, techniques that do not come into contact with the tissues and can be performed in a fairly short amount of time (no more than 2 seconds) are desired. To measure tissue biomechanics, a mechanical stimulus, such as ultrasonic waves, is applied. The response of the cornea to these waves requires a high-resolution fast acquisition device, such as an Optical Coherence Tomography (OCT) system.

However, skin is the largest human organ; It has a surface area of 1.7 - 2.0 square meters and is composed of the epidermis, dermis, and hypodermis. Skin acts as a physical barrier that keeps humidity and temperature under control; it also protects the body from external organisms such as viruses and bacteria. Furthermore, skin metabolizes vitamin D interacting with ultraviolet radiation from the sun. This process requires the skin to be exposed to solar radiation that can penetrate from the epidermis up to the end of the dermis (the middle layer); the hypodermis, the last layer of the skin, does not receive this type of radiation.

However, an excess of type A ultraviolet (UV) radiation can cause burns to the epidermis and, in some cases, cancer, the formation of malignant cells in the skin. There are different types of cancer associated with the types of cells affected (basal, squamous, or melanocytes) [5]. The first stages of cancer appear in cells located in the epidermis layer; as they progress, the deeper layers of the skin are compromised. In stage 0 (carcinoma in situ), abnormal cells can already be seen but are not yet considered cancer; in stage I, these cells have turned into cancer and form tumors up to 2 cm in area. In stage II, tumors can have an area of up to 4 cm and have already spread to the dermis layer. Stage III tumors have a surface area greater than 4 cm and can extend to subcutaneous tissue and, in some cases, reach bones [5].

Skin cancer detection is performed with the ABCDE screening method (**A**symmetry, **B**order, **C**olor, **D**iameter and **E**volution), a visual inspection of the suspicious area, from which the health personnel will decide whether the case should be confirmed with a final test called Punch biopsy. Since the initial inspection is a purely visual and subjective method, it is likely that some cases diagnosed as negative are actually stage 0 cases; on these occasions, patients will lose the opportunity to be diagnosed at this very early stage and should wait for another screening. These cases are called false negatives.

Treatment for skin cancer involves the removal of affected areas; If it is performed in the initial stages, only small sections will have to be removed; but if it is performed in the later stages, the section to be removed will cause injuries that require longer recovery periods and leaves scars. Techniques such as Mohs microsurgery, electrodesiccation, cryosurgery, laser surgery, among

others, are also used [5].

The reduction of false negative cases of skin cancer would increase the number of patients who can start their treatment in the early stages.

1.1 Problem Statement

1.1.1 Keratoconus

The eyesight system is composed of two eyes, each of them has the following sections:

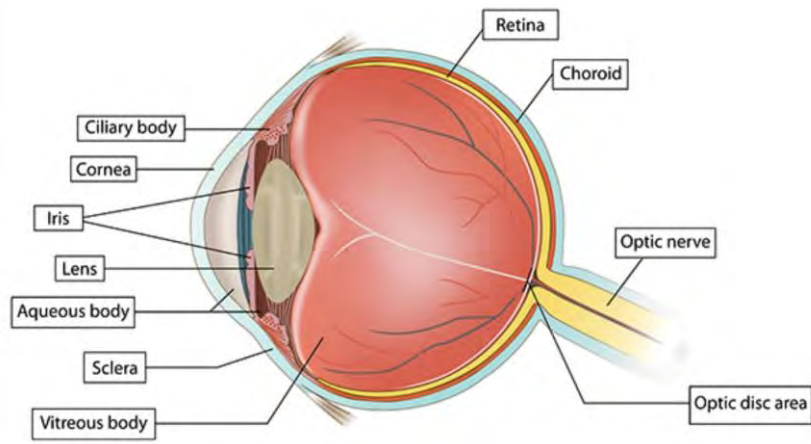


Figure 1.1: Parts of a human eye. Image taken from "Natural Eye Care" [6]

Eyes are optic systems that focus object reflected/scattered light rays to the retina, a tissue sensible to light, that transmit the received stimulus to the brain using the nervous system. Then, the main purpose of the eyes is to ensure that light rays are focused correctly.

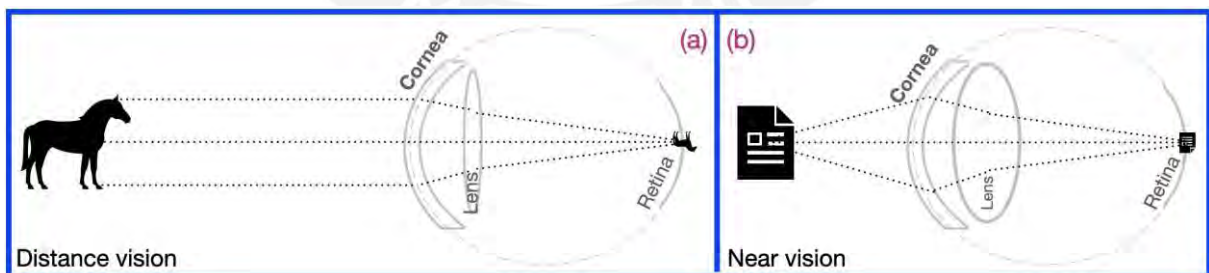


Figure 1.2: Figure (a) shows the optic configuration for distant objects; the lens has a "thin" configuration. Figure (b) shows a near object configuration, like the one used for reading; in this scenario the lens has increase its thickness.

As shown in Figure 1.2, the eye adapts its length thickness to focus the image from objects located at long and short distances. The ciliary body contracts the lens to adopt a thick shape in order to focus objects located at very short distances. For distant objects, the ciliary body relaxes.

When the light rays, reflected by the objects, are not focused in the retina, the generated images are blurred, and the patient must squint to have a clear image. This is a case of refractive error. The most common cases of refractive errors are myopia, hyperopia, and astigmatism.

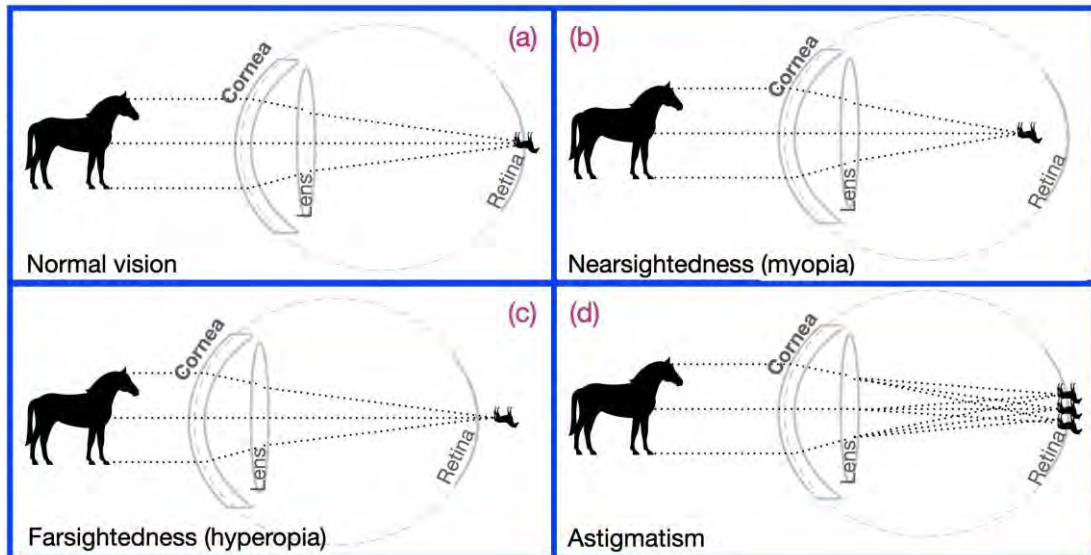


Figure 1.3: Normal and most common refractive errors eyes. Figure (a) shows a normal vision case. Figure (b) shows a myopia case; images are formed before reaching the retina. Figure (c) shows a hyperopia case; images are formed after the retina. Figure (d) shows an astigmatism case; images reach the retina, but there are not correctly formed - Myopia and hyperopia can be caused by an abnormal eye length or by abnormal cornea or lens shape. Astigmatism can be caused by abnormal cornea or lens shape.

These visual disorders are easily treated with correction lenses, contact lenses, and, in some cases, surgery. Correction lenses are composed of convex and/or concave interfaces. In some cases, Refractive Surgery is used to reshape the cornea, so the correction effect produced by the lenses will be provided by the reshaped cornea.

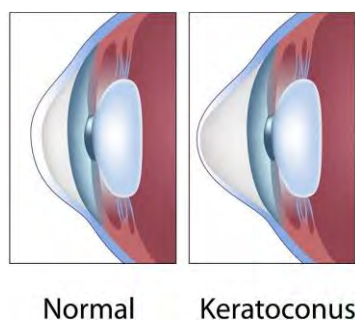


Figure 1.4: Left picture shows a normal eye. The right picture shows an eye affected by keratoconus. The cornea thickness is thinner than the normal ones; also, the shape of the keratoconus affected cornea becomes steepened - Image taken from "Dupage Optical" [7]

There are also other disorders related to eye shape, astigmatism and keratoconus. Astigmatism is caused by an abnormal corneal shape, which causes the light rays not to reach the retina; in this case, the symptoms and treatments are quite similar to Myopia. However, keratoconus is a progressive deformation of the cornea.

The cornea not only changes its shape, but also loses rigidity. As long as the strength of the corneal tissue decreases, the shapes become bulgier, pulled by gravity.

In earlier stages, Keratoconus can be treated with the cross-linking technique, a combination of UV radiation and riboflavin, to increase tissue stiffness and stop disease regression. In later stages, a cornea transplant remains the only solution.

According to the Cornea Research Foundation of America, between 50 and 200 of every 100,000 people are affected by keratoconus in the United States. In any case, keratoconus is one of the main causes of corneal transplants. In Peru, 120 corneal transplants are performed every year, but 300 more cannot be performed due to the lack of donors [2]. Early detection of keratoconus could reduce the need for corneal transplants.

1.1.2 Skin cancer

As the largest organ of the human body, the skin plays an important role in our lives. Not only does it act as a shield against mechanical impacts, chemicals, bacteria and viruses, but it also controls the body temperature.

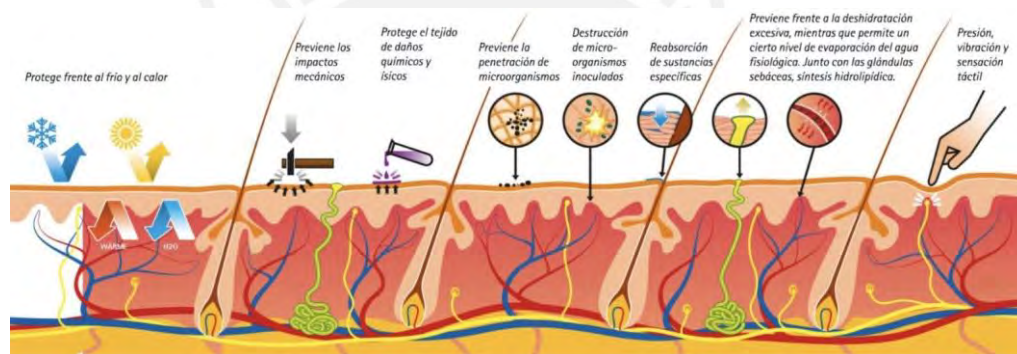


Figure 1.5: Chemical, mechanical and biological protection provided by the skin - Image taken from "Trucos de Belleza" [8].

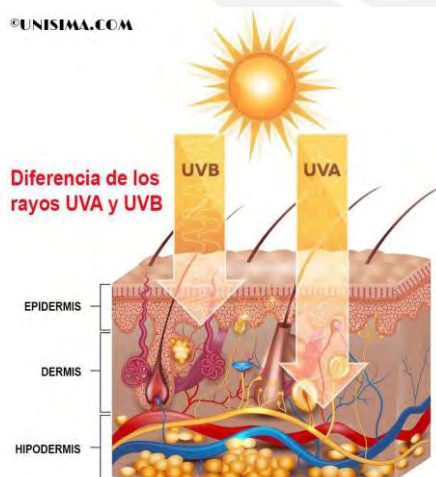


Figure 1.6: Depth penetration by UV type. Type A penetrates up to the deepest layers of the dermis, while type B only reaches the epidermis - Image taken from "Radiación UVA y UVB: La Importancia de la Protección Solar" [9].

Skin also contains biological sensors that provide the sense of touch as it is located in the body's external layer. In addition to the effects of the sun, skin can be damaged by mechanical or chemical agents. In addition, some microorganisms can cause skin irritation. The skin is also responsible for the synthesis of vitamin D through the interaction of UV. However, exposure to UV radiation is harmful to skin health. Skin burns are the most common type of damage due to overexposure, but the most severe is skin cancer.

Skin cancer can be divided into different types, according to the type of affected cells (basal, squamous, melanocytes, etc.).

The early stages of cancer start in the most superficial layer, the epidermis, but as it progresses the disease goes deeper into the inner layers, due to exposure to ultraviolet (UV) radiation. UV radiation is a form of non-ionizing radiation that is emitted by the Sun and some artificial sources. It is usually classified in three types:

Table 1.1: UV Classification [10]

UV-A	UV-B	UV-C
315 - 399 nm	280 - 314 nm	100 - 279 nm
Not absorbed by the ozone layer	Mostly absorbed by the ozone layer, but some does reach the Earth's surface	Completely absorbed by the ozone layer and atmosphere
	Synthesizes Vitamin D	

UV radiation can penetrate the epidermis and dermis layers of the skin. The epidermis is the most affected by sun overexposure. According to the World Health Organization, every year between 2 and 3 million people will suffer from skin cancer (melanoma and non-melanoma types) in the world [11]. An investigation by Melina Arnold et al. (2022) concludes that melanomas cases will increase by 50% between 2020 and 2040 [12].

According to the "Centro Nacional de Epidemiología, Prevención y Control de Enfermedades" (CDC), skin cancer was the second most frequent in Perú (2022 first quarter, distribution of cancer types).

DISTRIBUCIÓN DE LA INCIDENCIA DE CÁNCER EN EL PERÚ, ENERO-ABRIL 2022

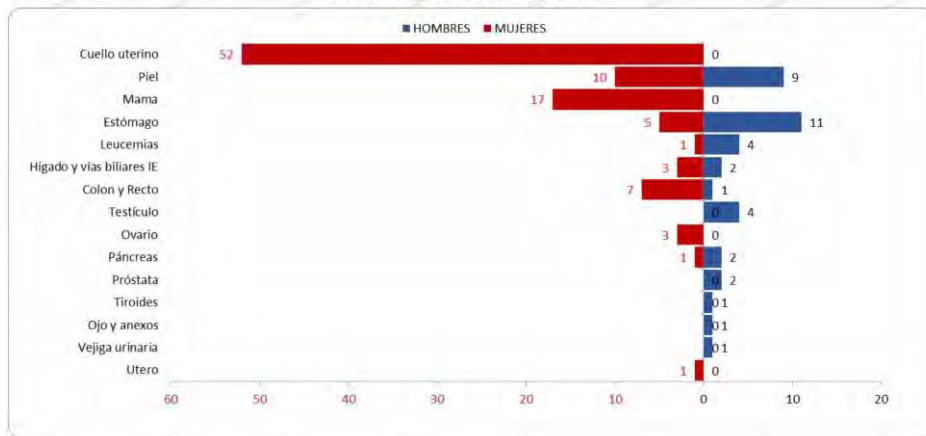


Figure 1.7: Peruvian Cancer Distribution in the first quarter 2022 - Image taken from "Sala Situacional del Cáncer en el Perú, January-April 2022" [13].

Physicians diagnose skin cancer by examining the color and shape of unusual formations (ABCDE rule mentioned at the beginning of this chapter), followed by a skin biopsy, a procedure that involves the extraction of a section of the suspected affected tissue.

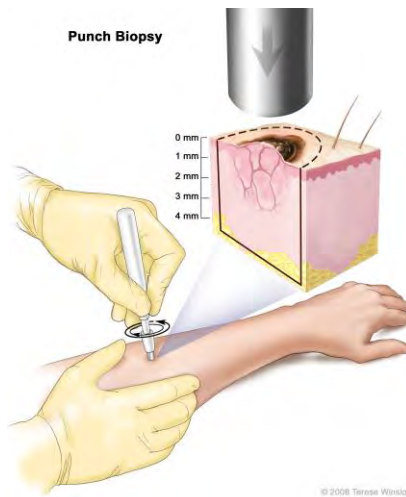


Figure 1.8: Punch biopsy consist in extracting a section of the skin tissue with a special probe. Figure shows the punch biopsy procedure which requires a special probe to extract a small section of the skin. The surface area is not significant, but it can go up to 4mm deep. The affected area can take up to 2 months for full recover. This procedure is required after a health professional executes the ABCDE screening procedure and is the final diagnostic exam. A non-invasive diagnostic tool that can display and analyze the affected area without the need of removing it from the patient may help physicians as well as allow patients to continue their normal lives - Image taken from "Melanoma Treatment (PDQ®)–Patient Version" [14]

The early stages of cancer start in the upper layers of the skin. Having the ability to generate images of these upper layers will allow physicians to identify positive cases.

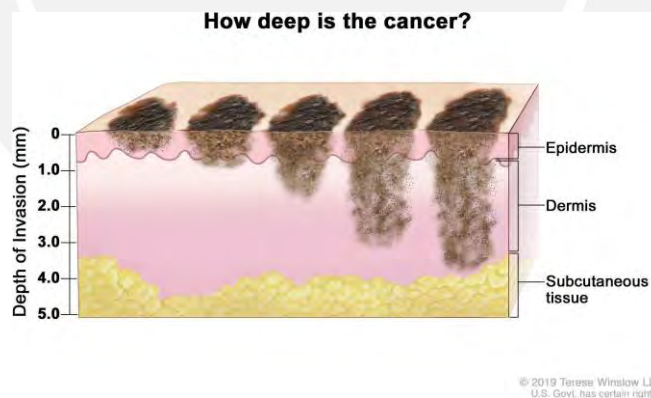


Figure 1.9: Cancer stages depth. The higher the stage is, the deeper the affected tissues spread. Earlier stages affect only epidermis, but later ones can go up to the dermis layer with almost 4 mm depth. Melanoma presents itself in melanocytes, cells that provide color to the skin. Other skin cancer types can also present in squamous and basal cells; these two are called Non-Melanoma Skin Cancer. In order to identify earlier stages of skin cancer, the most superficial epidermis layers need to be analyze. - Image taken from "Melanoma Treatment (PDQ®)–Patient Version" [14]

As mentioned above, some elastography techniques have found that cancer tissue is more rigid than normal tissue [15]. This technique can be used to identify early cancer stages and also reduce false negative cases.

1.2 State of the Art

1.2.1 Clinical standard for diagnosing keratoconus

As mentioned in the Introduction, keratoconus detection can be performed by corneal topography that produces a map of the superficial curvature of the cornea, by a slit lamp test, a procedure that can detect morphological abnormalities and by pachymetry, an exam that measures cornea thickness. All of these methods provide a topology and thickness analysis in which keratoconus can be identified if they are different from the normal topology and thickness of the eye.

Corneal Topography

Corneal topography is the most reliable method of diagnosing and checking the progression of keratoconus, astigmatism, injuries and infections, among others [16].

Topography techniques can be classified as [17]:

- Reflection-based
 - Keratometry
 - Keratoscopy
 - * Placido disc
 - * Photokeratoscopy
 - * Videokeratoscopy
- Projection-based
 - Rasterstereography
 - Interferometry

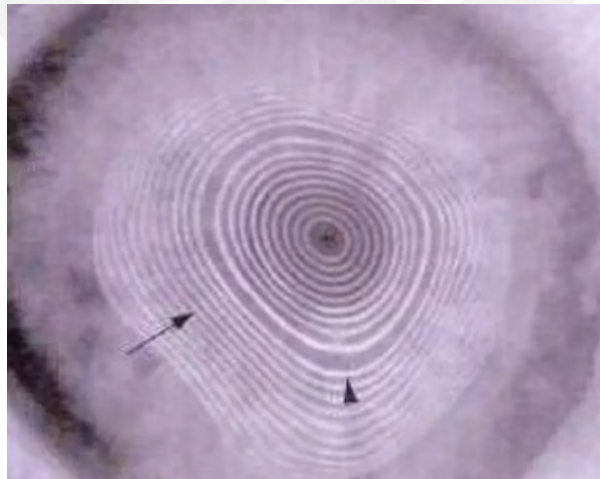


Figure 1.10: Placido disc projection in an eye. The projection of concentric circles over the corneal are analyzed to evaluate its optical properties. Abnormal formations in the cornea surface will produce different patterns; the closer the rings the more pronounced the inclination. The flatter the cornea, the wider the rings will be. - Image taken from "Corneal Topography" [17]

A normal cornea presents a regular distribution between its rings and thickness, figure 1.11 (a). By analyzing the ring patterns, the physician can diagnose its topography anomalies, figure 1.11 (b).

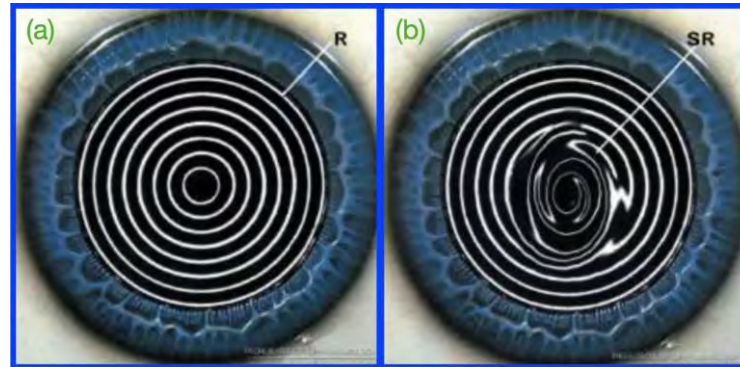


Figure 1.11: Figure (a): Placido disc eye ring pattern reflection from a normal eye. Figure (b): Placido disc eye ring pattern reflection from a keratoconus eye. This method cannot detect small deformations and can be deceived by other disorders like stromal ulcers and epithelial defects as they will produce abnormal reflection - Image taken from "Corneal Topography" [17].

Slit Scanning

Slit scanning technique replaces circles with slits, while scanning their reflection (figure 1.12).



Figure 1.12: Parallel Slit scanning technique performed by an Orbscan system - Image taken from "Corneal Topography" [17].

The slits can also be taken in a multimeridian pattern. Figure 1.13 shows a scanning sequence performed by an Oculus Pentacam AXL system.

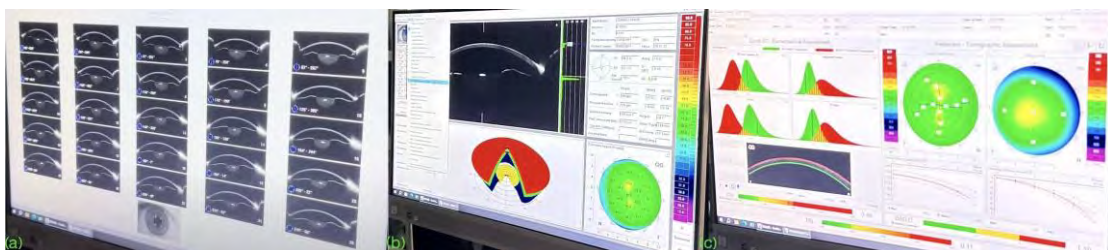


Figure 1.13: Figure (a) shows how an Oculus Pentacam system takes 20 meridian scans (each rotated 9° degrees) to cover the cornea. Figure (b) shows the system processing the 20 scans information gathered, analyzing their reflection, in order to create a surface and thickness map. Figure (c) shows the system extrapolating a topology map by combining all the scans.

Optical Coherence Tomography

Due to its resolution and scan speed, Optical Coherence Tomography (OCT) systems are used for pachymetry and epithelial mapping to diagnose keratoconus [18]. These systems provide medical professionals with images and measures that allow them to assess the condition of the cornea without further processing.

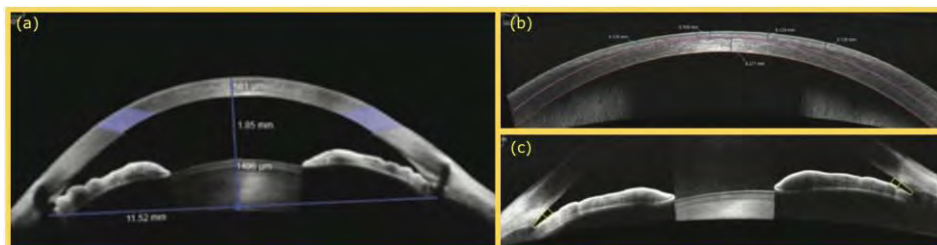


Figure 1.14: A Zeiss Cirrus HD-OCT was used to scan the eye anterior side. Figure (a) shows the Chamber view. Figure (b) shows a high definition corneal image. Figure (c) shows a detail view of the lens and iris. Image taken from "Cirrus HD-OCT 5000/50 booklet"[19].

Experimental Research

Some research studies used OCT with a mechanical stimulus to identify the early stages of keratoconus. Using an air puff and a Swept Source OCT system, normal and keratoconic corneas were compared.

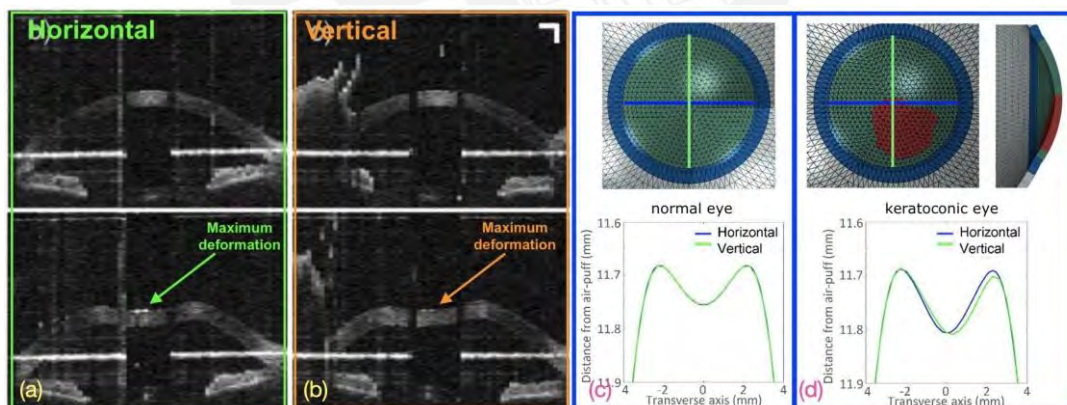


Figure 1.15: Figures (a) and (b) show air puff stimulus applied to an *in vivo* human cornea with a crosshair pattern. Figure (a), the green section, corresponds to the horizontal scan at two moments; at rest state and the bottom one when the air puff caused its maximum deformation. Figure (b), the orange section, shows the same two conditions but on the vertical scan. OCT can also display the transition from rest to maximum deformation and vice-versa. Figures (c) and (d) were taken using an *ex vivo* porcine eyes; one of them was artificially modified to mimic a keratoconic eye. Figure (c) shows the analysis performed on the normal eye. Figure (d) shows the same analysis performed in the keratoconic eye. - Images adapted from "Multi-meridian corneal imaging of air-puff induced deformation for improved detection of biomechanical abnormalities" [20].

Keratoconus summary

The actual techniques and equipment used to detect and monitor keratoconus and other corneal abnormalities provide reliable information to develop diagnoses. However, these equipments and techniques require the presence, at least at a minimum level, of corneal deformation.

If keratoconus can be diagnosed before it causes corneal deformations, proper treatment could be applied with better chances to stop the disease. According to some researches, such as "Human cornea biomechanics and subclinical keratoconus detection using ultrasonic wave-based optical coherence elastography", some corneal biomechanical properties can change prior to topographic deformation[21]. Identifying these properties would allow physicians to identify keratoconus in very early stages without having to wait until the cornea starts to deform its surface. According to multimeridian corneal imaging of air-puff-induced deformation for improved detection of biomechanical abnormalities [18] and the confocal air-coupled ultrasonic optical coherence elastography probe for quantitative biomechanics [20], Optical Coherence Elastography can be used as a reliable way to identify keratoconus in the early stages from the biomechanical perspective, rather than topography.

1.2.2 Clinical standard for diagnosing skin cancer

Skin Cancer diagnostic is based on visual assessments. The first level screening test, performed by the general population and physicians, is called ABCDE based on the criteria actions, Asimetry, Border, Color, Diameter and Evolution.

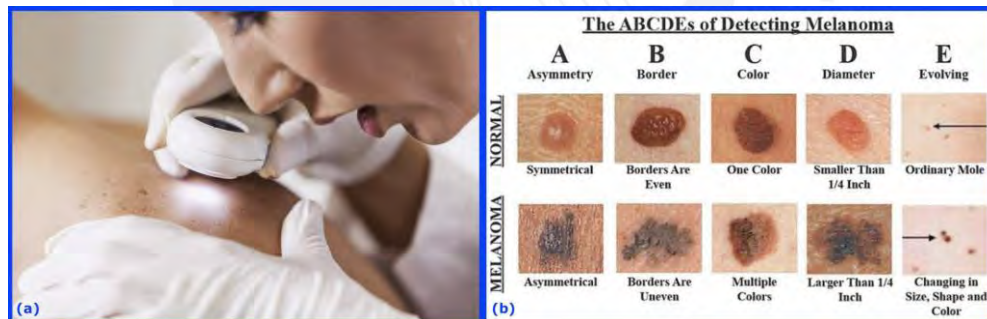


Figure 1.16: Figure (a) shows the ABCDE screening performed by a health professional, using an amplifier tool. Figure (b) shows the table used to identify melanoma from normal moles. - Images taken from "Skin Cancer Foundation" [22].

Each person can perform the ABCDE screening by looking directly at the suspected area or using a camera. Skin cancer usually presents in exposed areas such as arms, legs, and torso. Minimal assistance is required to use the ABCDE method. Health professionals will screen the suspected area by direct visual examination or using magnifying glasses as shown in Figure 1.16 (a). Some magnifying devices can be adapted to smartphones or the same phone's camera can provide the required magnification. After using the ABCDE (first level) screening method in suspected areas, physicians will rule out a possible cancer case or they will request a final examination, a histological examination. To perform the histological exam, a portion of the suspected area must be removed from the patient. Punch biopsy is one of the methods used to extract the sample as shown in figure 1.8.

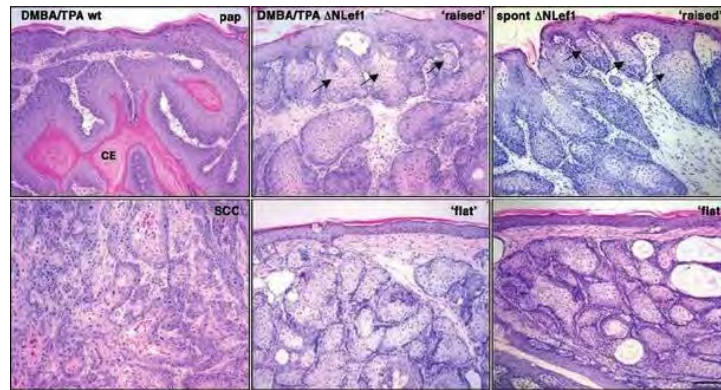


Figure 1.17: For Histology exams the extracted tissue is laminated, placed in a slide and colored to identify cancer cell morphology. Sampled tissues are colored and examined under microscope. Cell morphology will reveal abnormal cell formations and its quantity. Figure shows different types of anomalous cells like squamous cell carcinoma and sebaceous tumors - Image taken from "Dual Role of Inactivating Lef1 Mutations in Epidermis: Tumor Promotion and Specification of Tumor Type" [23].

At the date this document is elaborated, some blood tests are used to diagnose Melanoma. This specific test looks for lactate dehydrogenase (LDH), but its presence indicates that the melanoma has spread to other parts of the body and, if the indicators of LDH are high, the disease will be difficult to treat [24].

Experimental Research

Taking advantage of the penetration capacity of OCT, it is possible to obtain images from the epidermis to identify the tissue topography and structure. Figure 1.18 shows a comparison between normal and cancer skin tissue.

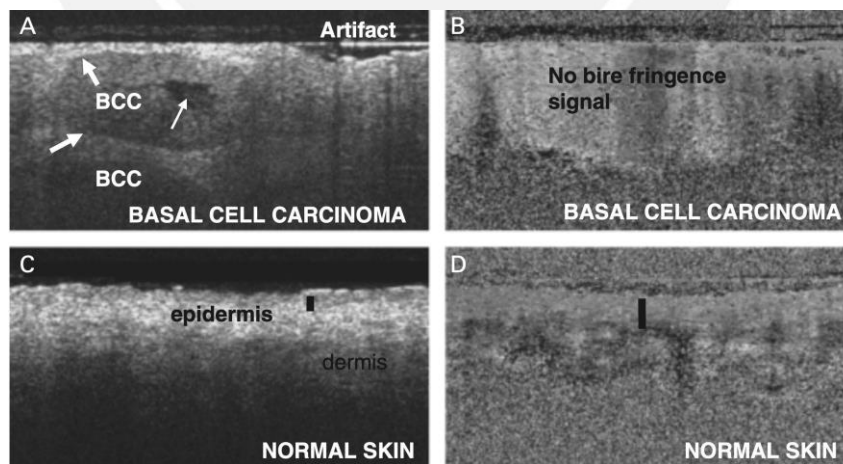


Figure 1.18: Sub-figure A shows a Basal Center Carcinoma section; fat white arrows mark the BCC border while the thin white arrow points to a necrotic center. Sub-figure B shows a Polarity-Sensitive OCT (PS-OCT) from a portion of the same area. Sub-figure C shows a normal skin image and sub-figure D shows a PS-OCT capture; the black bar is the same area in C and D - Images taken from "Assessment of Optical Coherence Tomography Imaging in the Diagnosis of Non-Melanoma Skin Cancer and Benign Lesions Versus Normal Skin" [25].

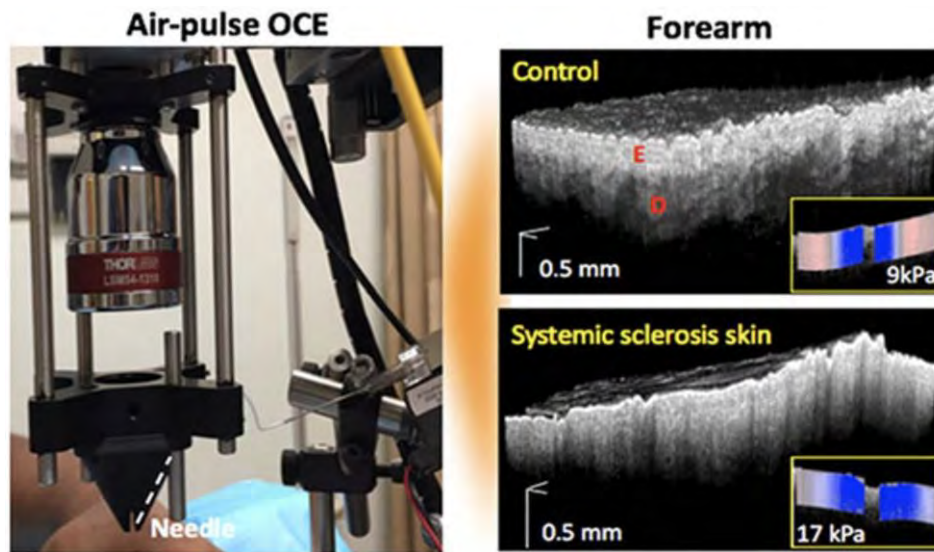


Figure 1.19: Air puff OCE system. A Thorlabs LSM54-1310 scan lens is used for the optical components. Below the lens a conical structure allows air puff to hit the skin without obstructing the optical axis. Two samples were scanned, a healthy sample at the top (Control) and an illd one (a case of Systemic sclerosis skin) at the bottom. Scanned images show the skin structure obtained with OCT and small sections located at the bottom right corner show the wave propagation. Image taken from "Translational optical coherence elastography for assessment of systemic sclerosis" [26].

Skin cancer summary

Biopsies are prescribed by health professionals after performing a visual screening (ABCDE). There are four possible outcomes for this examination.

		Actual	
		Positive	Negative
Diagnosed	Positive	True Positive	False Positive
	Negative	False Negative	True Negative

Figure 1.20: Diagnose Confusion Matrix shows the possible outcomes for ABCDE screening.

A true negative diagnosis will not have an impact on patients. However, a true positive will require a biopsy to characterize the cancer and evaluate its stage. False-positive diagnosed patients will have to undergo a biopsy, which requires the extraction of a small skin section, but histological analysis will rule out the cancer.

False negatives diagnostics can affect patients health. As they do not receive treatment, skin cancer will continue to spread to later stages of severity.

In order to reduce false negative cases, visual screening has to be improved or complemented for a more reliable procedure. Alfageme Roldán indicates, in his 2016 publication [15], that cancer tissue becomes more rigid than normal skin tissue. Identifying these changes will help reduce false negative cases.

1.3 Proposal

From the summary of keratoconus (section 1.2.1) it can be seen that actual techniques and equipment diagnose keratoconus when the disease has already modified the cornea topography. According to some studies, the biomechanical properties of the cornea change, leading to topological deformation [27]. To identify these biomechanical properties, elastography procedures and techniques must be used for the clinical evaluation of keratoconus.

From the skin cancer summary 1.2.2, a technique or procedure that can identify the biomechanical properties of the skin will help reduce the number of false negative cases [15]. In addition to the previous cases, elastography procedures and techniques can help identify modifications in rigidity.

This thesis proposes to design and implement an imaging system that can integrate elastography techniques to acquire tissue responses. Resolution and penetration are two parameters that must be considered in order to select the proper imaging technique. Considering that the cornea has between 400 and 600 μm thickness, ultrasound, computed tomography, and magnetic resonance cannot be used for the diagnosis of keratoconus. Confocal microscopy has a finer resolution, but it penetrates only 200 - 300 μm .

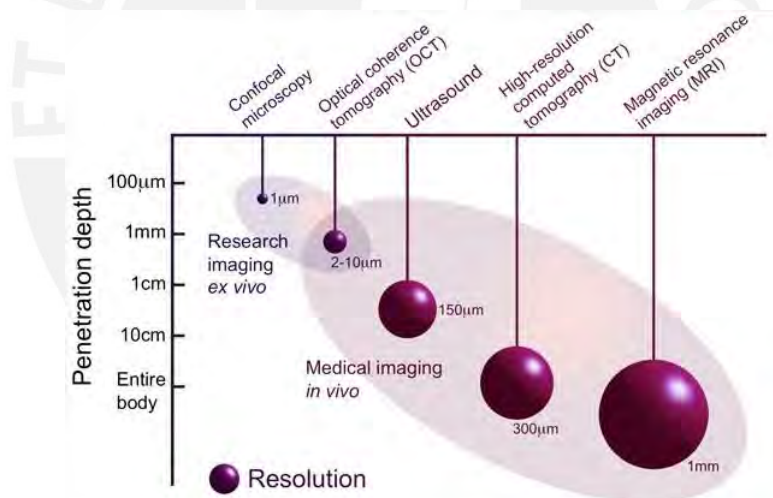


Figure 1.21: OCT has between 2 to 10 μm resolution with a penetration of up to 1 or 2 mm; this resolution provides enough details of corneal tissues and skin. 1 mm penetration covers the whole cornea thickness; it provides the depth required to locate stages 0 and I skin cancer cases. Ultrasound, high resolution CT and MRI does not have the resolution to generate corneal images. Confocal microscopy has better resolution than OCT, but it can only penetrate tissues a couple of hundreds micrometers. [28].

This thesis proposal consists of the design and implementation of an swept source optical coherence tomography (SS-OCT) system that can capture the tissue response to elastography techniques in order to diagnose early stages of keratoconus and reduce false negative diagnoses of early stages of skin cancer. The system must be prepared for scanning human eyes and skin under safety regulations. The scan information must be delivered to a computer where the control, capture and process will be performed using applications like LabVIEW and MatLab.

1.4 Objectives

1.4.1 General Objective

To design, implement and characterize an optical coherent tomography (OCT) system to generate structural images of ocular and skin tissues. The system should be able to detect displacements caused by non-contact ultrasonic mechanical excitation in wave-based biomedical elastography applications.

1.4.2 Specific Objectives

1. Conduct an analysis of the requirements for an OCT system that is capable of measuring the structure of ocular and skin tissues, as well as the propagation of mechanical waves in those tissues.
2. Design the optical system and define the list of optical, optomechanical and electronic components based on the requirements explored for that OCT system.
3. Implement, assemble and align the OCT system using the chosen components according to the proposed optical design. Optimize optical design based on alignment and calibration tests.
4. Characterize the OCT system in terms of axial and lateral resolution, image depth, acquisition speed, sensitivity and stability using calibration standards and acquisition protocols.
5. Acquire OCT images of synthetic models that have the dimensions of human eye and skin tissues.

1.5 Scope and limitations

1.5.1 Scope

1. Collect design requirements and implement an OCT system that can generate images of cornea and skin tissues with micrometric resolution to evaluate their morphological structure. In addition, to gather scan speed requirements that allow the procedure to be performed without patient discomfort.
2. To design an OCT system and optimize its components (optical, mechanical and computational) to obtain the best possible result (resolution and speed) with the most simple implementation.
3. The resultant system must be ready to integrate with an ultrasound elastography module that can stimulate the tissues of the sample without affecting optical scanning. For this purpose the synchronization between the swept laser source, the ultrasound stimulus, the galvanometric mirror array and the data processing application.
4. Align all the optical and electric elements to obtain the maximum acquired optical power with the lowest noise ratio at the acquiring devices.

-
5. To characterize the system to obtain its system parameters like axial and lateral resolution, deepness, sensitivity and roll-off.
 6. To acquire images from test objects in order to verify the system functionality and parameters. Synthetic objects will be used for these procedures.

1.5.2 Limitations

1. The system will not include the elastography module, but it will provide space and synchronization signals.
2. The application for image processing and mirror control is not included as part of this project. An existing application will be used for the purposes of this thesis.
3. This thesis will not include the measurement of biological tissues; synthetic samples and phantom will be used.

1.6 Expected Results

At the end of the project, an optimized and functional OCT system will be achieved. This system will be designed and implemented with the following results:

1. The system must be modular, so a modification in one module produces the minimum impact on the other modules.
2. The system must allow the integration of an ultrasound elastography module and additional ones such as badal systems.
3. The system will be optically aligned to produce the resolution and scan speed required by the ultrasound elastography module.

Chapter II

Theoretical Background

2.1 Optical Coherence Tomography (OCT)

OCT is a medical imaging technique that generates cross-sectional and volumetric images with micrometer resolution, using back-scattered light from a coherent light source.

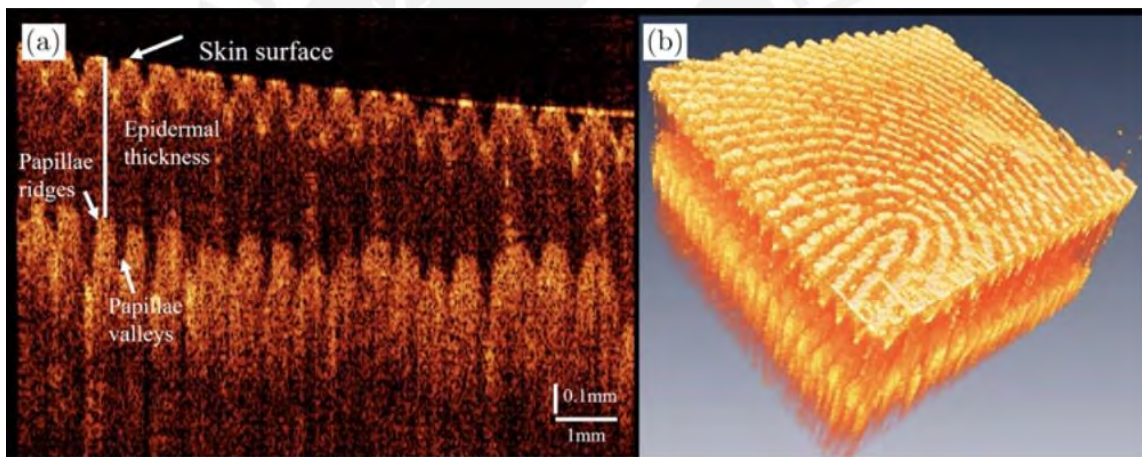


Figure 2.1: Figure (a) shows a cross section image from a skin sample (2D image). Figure (b) shows a volumetric image, created by multiple cross sectional images from the same skin sample (3D image) - Images taken from "A measurement of epidermal thickness of fingertip skin from OCT images using convolutional neural network" [29].

As the source light penetrates the sample, it will be reflected in different directions as it reaches different layers. As the refractive index changes, the backscattered light will be reflected differently with every change (Figure 2.2). Depending on the wavelength and power of the light source, penetration will reach 2 or 3 mm (figure 2.2).

As light travels at a speed of 299,792 km/s in vacuum, direct measurement of its reflection on small distances is not an option. OCT uses interferometry to measure these small distances, a technique that uses a light beam that is split into two paths, one to measure the sample and the second used as a reference. In addition, low-coherent light sources are used in this technique.

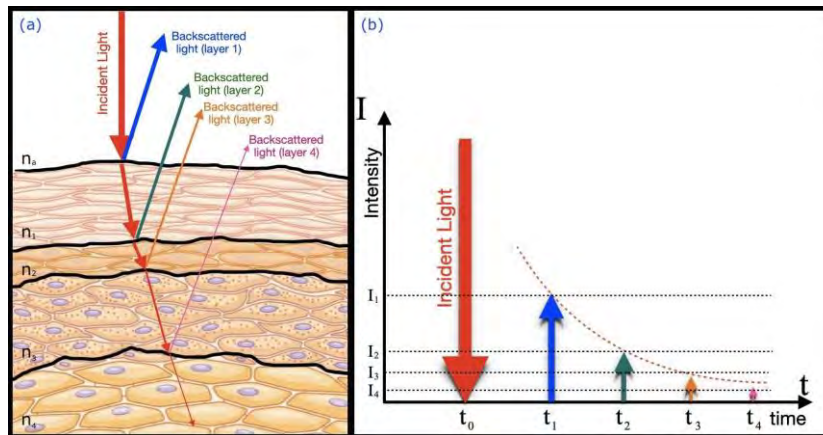


Figure 2.2: OCT principle is that light will be refracted in a different speed due to its refractive index (n_x). Figure (a) shows a skin diagram receiving an incident light beam. This beam will be, partially, reflected and dispersed (backscattered); the rest will be transmitted (refracted) through this layer until it reaches the following one. This behavior repeats until the intensity is completely absorbed by the tissues - Image modified from "Skin and its histology applied" [30]. Figure (b). As the incident light beam travels through each layer of the tissue, backscattered beams will be generated, each one of them attenuated compared to the previous one. Each backscattered beam will be delayed to the ones generated in upper tissue layers.

2.1.1 Optical Coherence

Coherence is defined as a correlation between two or more elements. Optical coherence presents when two or more light rays present temporal and/or spatial coherence. A laser beam is considered a **high coherence** beam while the sun light is the opposite, total incoherence light.

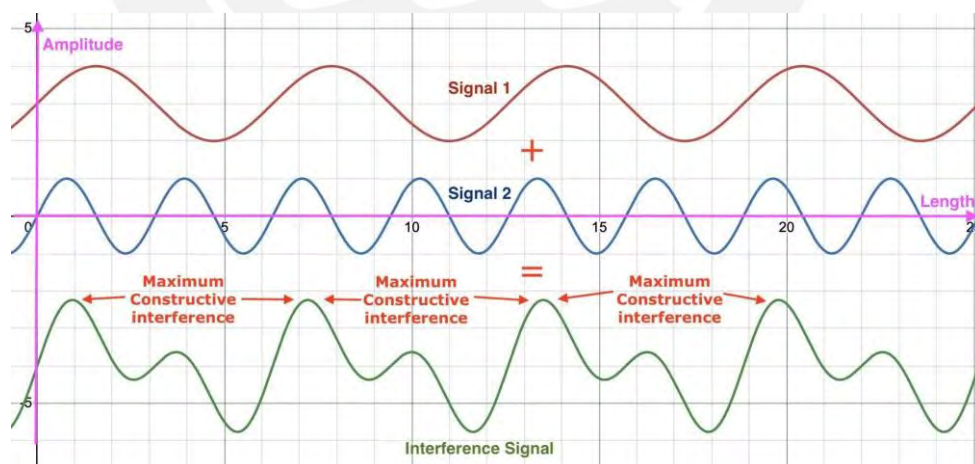


Figure 2.3: Spatially dependent interference pattern caused by a single wavelength (high coherence).

Lasers are high coherence light sources, because they have one wavelength; non-coherence light sources have a long range of wavelengths (such as the sunlight). For OCT interferometry, neither high-coherent nor non-coherent light sources can be used. Instead, low-coherence light sources provide an interferometry pattern that can be used to scan tissues and generate images.

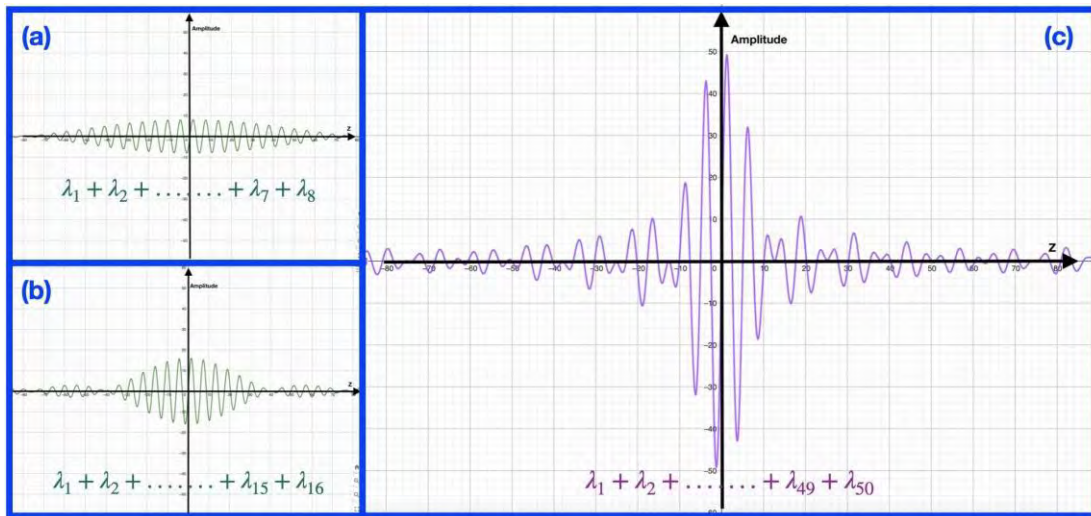


Figure 2.4: Figure (a): An interference pattern created by eight slightly different wavelength (λ_1) signals (1% difference). Figure (b) shows interference patterns created by 16 different wavelength signals. Figure (c) expands the number of signals to 50. The resultant temporal coherence interference signal has a pronounced amplitude and a Gaussian shape.

Temporal Coherence:

As figure 2.4 shows, the temporal coherence function pattern has a Gaussian shape. It is represented by:

$$G(\tau) = \langle E^*(t) E(t+\tau) \rangle_{\tau} \quad (2.1)$$

This is a signal interfered with itself but delayed by τ time and measured in a period average.

Normalizing $G(\tau)$ with $G(\tau=0)$:

$$g(\tau) = \frac{G(\tau)}{G(\tau=0)} = \frac{\langle E^*(t) E(t+\tau) \rangle_{\tau}}{\langle E^*(t) E(t) \rangle_{\tau}}; \quad 0 < g(\tau) < 1 \quad (2.2)$$

$g(\tau) = 0$ is presented on totally incoherent light sources, such as the sun, while $g(\tau) = 1$ can be found in highly coherent light sources such as precise lasers.

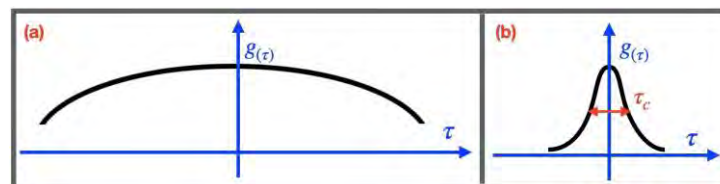


Figure 2.5: Figure (a) shows a pattern with $g(\tau) \approx 1$. Figure (b) shows a low coherence pattern. Their coherence periods have the following relation $\tau_{c(a)} > \tau_{c(b)}$.

Then the temporal coherence period (τ_c) and the length of coherence l_c are defined by:

$$\tau_c = \int_{-\infty}^{\infty} |g(\tau)|^2 d\tau; \quad l_c = c\tau_c \quad (2.3)$$

Where c = speed of light. The Wiener–Khinchin theorem states that the power spectral density can be expressed as the Fourier transform of the autocorrelation function.

$$S(\nu) = \int_{-\infty}^{\infty} G(\tau) e^{-i2\pi\nu\tau} d\tau \quad (2.4)$$

Then the temporal coherence function can be expressed as the inverse Fourier transform of the power spectral density.

$$G(\tau) = \int_{-\infty}^{\infty} S(f) e^{i2\pi\nu\tau} d\nu \quad (2.5)$$

2.1.2 Time Domain OCT

A basic OCT system is made up of two paths, one used as a reference and the other to scan a sample. These two paths are called reference arms and sample arms, respectively. Comparison of the reflected light beams from both arms, using an interferometer, will provide the information required to generate an image from the sample.

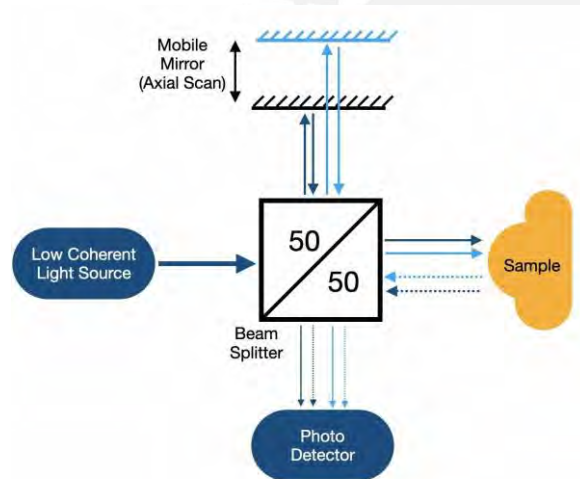


Figure 2.6: Time Domain OCT basic diagram. The mobile mirror identifies these types of system. Other techniques use a fixed mirror on the reference arm.

Figure 2.6 shows a basic OCT system, Time Domain OCT (TD-OCT). TD-OCT was the first OCT technique introduced in 1991 by D. Huang, E.A. Swanson, C.P. Lin, J.S. Schuman, W.G. Stinson, W. Chang, M.R. Hee, T. Flotte, K. Gregory, C.A. Puliafito and J.G. Fujimoto [31].

A superluminescent diode (SLD) is used as a low coherent light source. The core of the system is composed of a Michelson fiber-optic interferometer that receives sample and reference signals, producing an interference pattern that is converted to an electrical signal by a photo detector. This electric signal is then processed by a software application running on a computer.

As the mobile mirror displaces, increasing/decreasing the reference optical length, a matching backscattered light path will be produced from the sample. This means that both the reference and sample arms have the same optical length and a constructive interference signal is generated. The axial scan speed will be determined by the speed of the mobile mirror. The mirror controller must have accuracy and precision, as well as a fast transition. The interference signals from the reference and sample arms are received by the photodetector and converted into an electric signal that can be acquired and processed by the computer application.

TD-OCT Interferometry

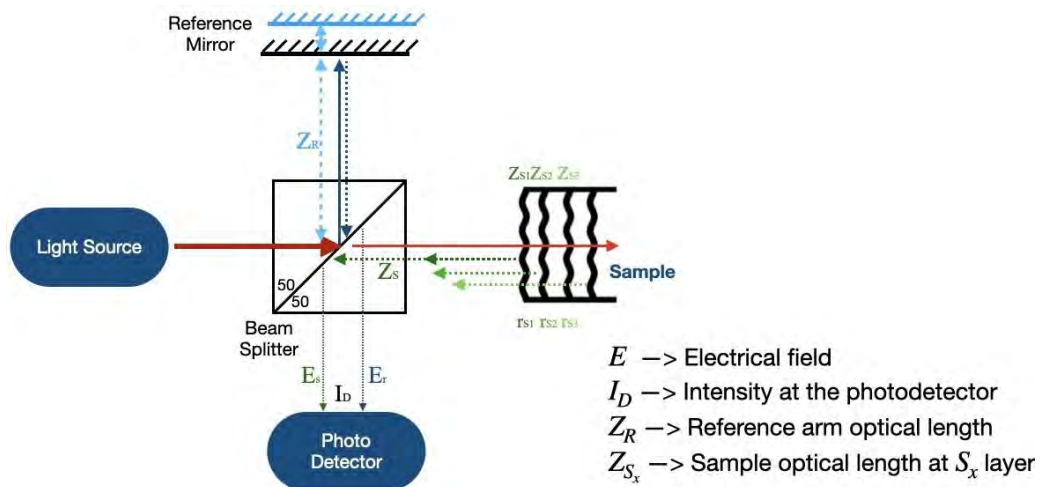


Figure 2.7: TD-OCT diagram and variable definition for interference calculation.

High coherence light sources, like lasers, produce multiple spatially dependent interference points because they only have one wavelength. For imaging, this behavior will not allow us to choose a specific point to identify the distance. A high coherent laser source cannot be used in this scenario. Instead, low-coherence light sources, such as superluminescent diodes (SLD), are used.

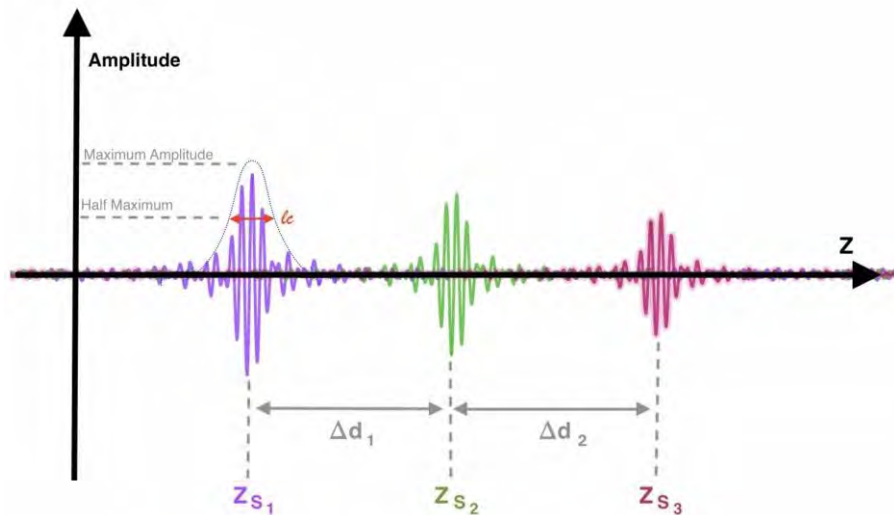


Figure 2.8: When a low coherence light source is used, one interference signal results when the Optical Path Lengths (OPL), reference and sample, are the same. These three interference signals correspond to sample layer 1, Figure 2.7 Z_{S_1} , layer 2 to Z_{S_2} and layer 3 to Z_{S_3} ; these signals were captured when the reference mirror was displaced along its axis. l_c stands for **length of coherence** and corresponds to the distance over which the wave maintains its coherence. It is measured at half the maximum (Full Width Half Maximum).

OCT uses low-coherence light sources, which produce a light beam with several wavelengths with minimal difference between them. With this source, an interference signal is generated for the first surface (see Z_{S_1} in Figure 2.8). The second layer generates the second constructive interference signal (Figure 2.8 Z_{S_2}). The distances between these interference patterns (Δd_1 and Δd_2) are also the distance between the tissue layers sampled and correspond to the distance from which the reference mirror was displaced until the interference signal formed.

The length of coherence (l_c) determines the resolution of the system. The wider l_c is, the larger the resolution. The narrower the l_c , the finer the details the system can obtain.

Interference From figure 2.7, light intensity (I) can be calculated from the electrical field, for a single wavelength(λ_1):

$$I = |\vec{S}| = \frac{|\vec{E}|^2}{Z_0} = \frac{\epsilon_0}{\mu_0} |\vec{E}|^2 \quad I \approx |\vec{E}|^2 \quad (2.6)$$

As a 50 / 50 beam splitter is used:

$$\frac{I_R}{I_o} = \frac{|\vec{E}_R|^2}{|\vec{E}_o|^2} \approx \frac{1}{2}; \quad \frac{E_R}{E_o} \approx \frac{1}{\sqrt{2}} \quad (2.7)$$

From equations 2.6 and 2.7, the electrical field at detector (E_D) can be expressed by:

$$E_D = E_r + E_s = \frac{1}{\sqrt{2}} E_R e^{ikZ_R} + \frac{1}{\sqrt{2}} E_S e^{ikZ_S} = \frac{1}{\sqrt{2}} \frac{1}{\sqrt{2}} E_o e^{ikZ_R} + \frac{1}{\sqrt{2}} \frac{1}{\sqrt{2}} E_o e^{ikZ_S}$$

$$E_D = \frac{1}{2} E_o e^{ikZ_R} + \frac{1}{2} E_o e^{ikZ_S} \quad (2.8)$$

Intensity (I_D) measurement is proportional to a temporal average of E_D :

$$I_D \approx \langle E_D E_D^* \rangle_T \quad (2.9)$$

From equations 2.8 and 2.9, the Intensity at the detector, for a single λ :

$$I_D \approx \langle (\frac{1}{2} E_o e^{ikZ_R} + \frac{1}{2} E_o e^{ikZ_S})(\frac{1}{2} E_o e^{-ikZ_R} + \frac{1}{2} E_o e^{-ikZ_S}) \rangle_T \quad (2.10)$$

$$I_D \approx \frac{1}{4} E_o^2 (e^{ikZ_R} + e^{ikZ_S})(e^{-ikZ_R} + e^{-ikZ_S})$$

$$I_D \approx \frac{1}{4} E_o^2 (e^{ikZ_R} e^{-ikZ_R} + e^{ikZ_S} e^{-ikZ_R} + e^{ikZ_R} e^{-ikZ_S} + e^{ikZ_S} e^{-ikZ_S})$$

$$I_D \approx \frac{1}{4} E_o^2 ((e^{ikZ_R} e^{-ikZ_R}) + (e^{ikZ_S} e^{-ikZ_R}) + (e^{ikZ_R} e^{-ikZ_S}) + (e^{ikZ_S} e^{-ikZ_S})) \quad (2.11)$$

The red section of the equation 2.11 correspond to the stand alone electric field components from reference and sample arms. The blue section corresponds to the interference term generated by the interference from the sample and reference arms.

$$I_D \approx \frac{1}{4} E_o^2 + \frac{1}{4} E_o^2 + \frac{1}{4} ((e^{ikZ_R} e^{-ikZ_S}) + (e^{ikZ_S} e^{-ikZ_R}))$$

$$I_D \approx \frac{1}{2} E_0^2 + \frac{1}{4} \text{real}((e^{ik(Z_R - Z_S)}) + (e^{-ik(Z_R - Z_S)})) \quad (2.12)$$

We had assumed that $I_R \approx I_S \approx \frac{1}{2} I_0$ and knowing that $2 \cos \theta = e^{i\theta} + e^{-i\theta}$:

$$I_D \approx \frac{1}{2} I_0 + \frac{1}{2} I_0 \cos \theta \approx \frac{1}{2} I_0 (1 + \cos \theta) \quad (2.13)$$

Where $\theta = k(Z_R - Z_S)$. From figure 2.4, Intensity at detector is composed by the intensity of each wavelength:

$$I_D \approx I_{\lambda_1} + I_{\lambda_2} + I_{\lambda_3} + \dots + I_{\lambda_n} \quad (2.14)$$

Then the Intensity from all wavelengths at detector can be expressed as:

$$I_D \approx \frac{1}{2} \int_0^{\infty} I(k) (1 + \cos \theta) \partial k \approx \frac{1}{2} \int_0^{\infty} I(k) \partial k + \frac{1}{4} \int_0^{\infty} I(k) (e^{ikz} + e^{-ikz}) \partial k$$

$$I_D \approx \frac{1}{2} I_0(k) + \frac{1}{4} \int_{-\infty}^{\infty} I_0(k) e^{ikz} \partial k \quad (2.15)$$

Where $z = Z_R - Z_S$. Replacing Temporal Coherence Function, equation 2.5 on the second term of equation 2.15:

$$I_D \approx \frac{1}{2} I_0(k) + G(\tau) \approx \frac{1}{2} I_0(k) + g(z) G_{(0)} \quad (2.16)$$

Then $G_{(0)}$ can be expressed by:

$$G_{(0)} = \sqrt{I_r I_s} \quad (2.17)$$

Replacing equation 2.17 in 2.16, the Intensity at the detector (I_D) will be expressed as:

$$I_D \approx \frac{1}{2} I_0(k) + \sqrt{I_r I_s} \text{real}(g(z)) \quad (2.18)$$

As the normalized Coherence Function ($g(z)$) and the intensity at the source ($I_0(k)$) are known parameters for the light source (provided by the manufacturer), the interference pattern will depend on the real component of the reference and sample intensities reaching the detector.

OCT System Resolution

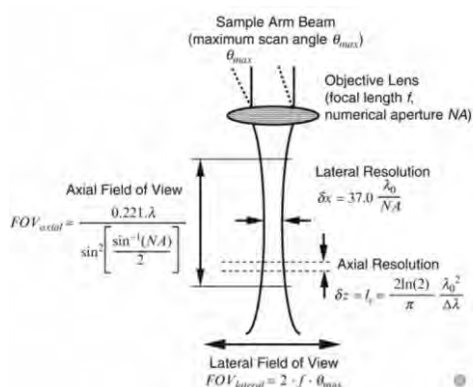


Figure 2.9: OCT systems are characterized by the lateral and axial field of view and the lateral and axial system resolution. These parameters depend on the light source and the sample scan lens parameters like, wavelength and Numeric Aperture (NA) - Image taken from "Optical Coherence Tomography Technology and applications"[32].

The axial and lateral field of view (FOV) are the areas that can be imaged by the system. The axial FOV corresponds to the depth in which the system can obtain images. The lateral FOV corresponds to the lateral area that can be covered by the system. The axial FOV depends on the wavelength of the light source and the NA of the scanning lens. The axial and lateral resolutions indicate the smallest detail that the system can identify. Axial resolution is related to the light source wavelength, central, minimum and maximum. Lateral resolution is related to the central wavelength of the light source and the NA of the lens.

2.1.3 Spectral Domain OCT

TD-OCT is limited by the reliability and speed of the reference mobile mirror. An improvement to this technique involves the use of a fixed mirror in the reference arm.

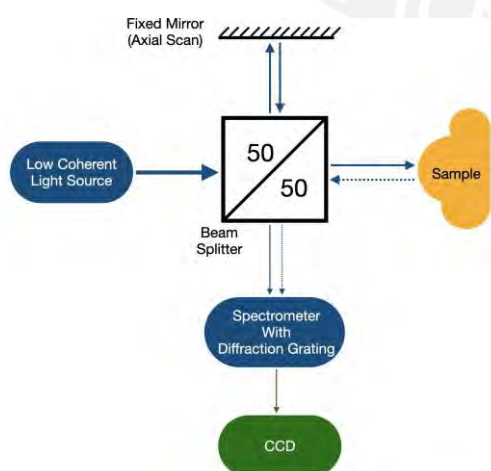


Figure 2.10: Spectral Domain OCT diagram. The reference mirror is now not mobile.

Spectral Domain OCT (SD-OCT) implementation was recorded in 1995. SD-OCT provides ultra-high axial scan (A-scan) speed, compared to TD-OCT with a more complex architecture, but without the mobile reference mirror. SD-OCT includes a spectrometer with a diffraction grating and a Charged-Coupled Device (CCD) camera instead of the photodetector used in TD-OCT. The CCD camera bins match the number of wavelengths split by the spectrometer.

Now, with a fixed reference mirror, the stability of the system was improved. The scanning speed increases from 400 A-scans/second in TD-OCT to 52,000 A-scans/second.

In SD-OCT, the interference spectrum is projected on a diffraction grating which will reflect each wavelength in a slightly different direction (Figure 2.11). This reflection will be captured by a detector array (CCD camera) with a defined number of bins; this arrangement will determine the system resolution.

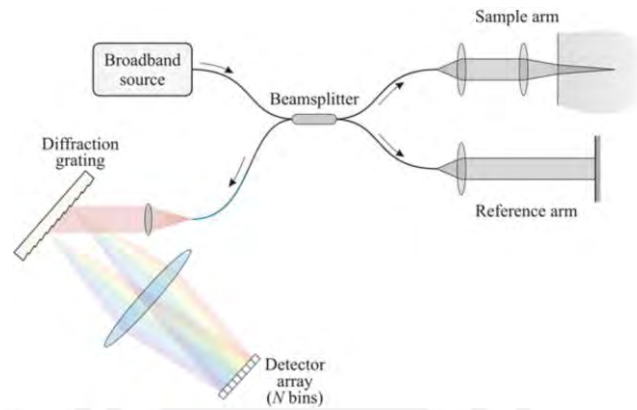


Figure 2.11: Basic SD-OCT schematic with a Michelson Morley interferometer. The detector array (a CCD camera) with an N number of bins to receive an N number of wavelengths - Image taken from "Introduction to OCT"[28]

SD-OCT Interferometry

In SD-OCT, the scattered light from the sample arm is combined with the beam from the reference arm. The interference spectrum is divided by wavelength, using a diffraction grid, so a CCD camera will receive these beams.

The CCD camera will determine the amount of wavelengths captured by the number of pixel bins. The diffraction grid must also have the capability of splitting the same number of wavelengths from the interference spectrum.

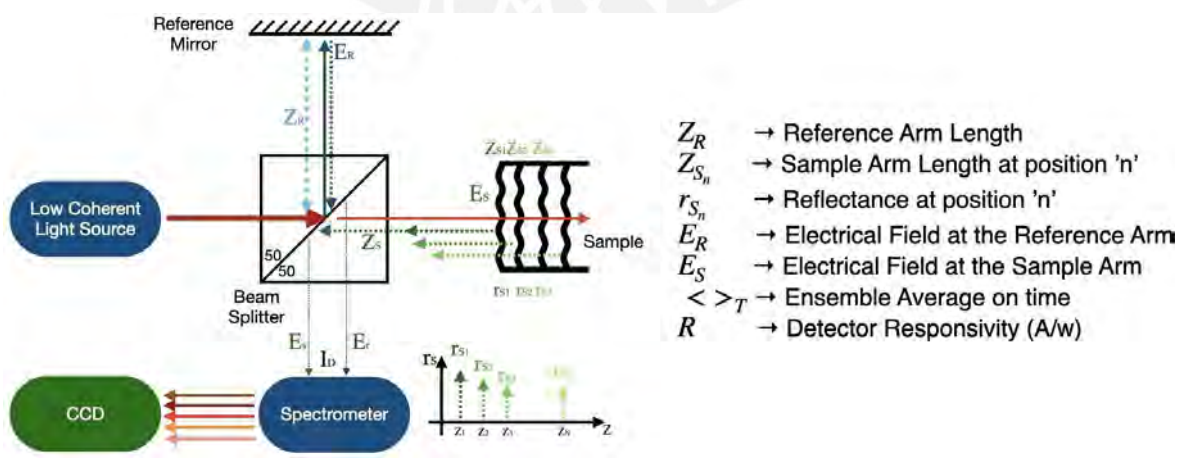


Figure 2.12: SD-OCT Interference. Each sample layer reflects the light beam from a different depth as shown in figure 2.2.

Interferometry The electric field (E_R) from the Reference Arm can be expressed as:

$$E_R = \frac{E_0}{\sqrt{2}} r_R e^{i2kz_R} \quad (2.19)$$

The reflectivity from the sample arm $r_s(z_s)$ can be expressed as the sum of the reflectivities from all sample layers:

$$r_s(z_s) = r_{s_1} + r_{s_2} + r_{s_3} + \dots + r_{s_n} \quad (2.20)$$

The electric field from the sample arm can be expressed as:

$$E_S = \frac{E_0}{\sqrt{2}} [r_s(z_s) \otimes e^{i2kz_s}] \quad (2.21)$$

Where:

$$r_s(z_s) = \sum_{n=1}^N \delta(z_s - z_{s_n}) \quad (2.22)$$

Then Intensity at the detector (CCD camera) can be expressed as:

$$I_D(\omega, k) = \frac{R}{2} \langle |E_R + E_S|^2 \rangle_T = \frac{R}{2} \langle |(E_R + E_S)(E_R + E_S)^*| \rangle_T \quad (2.23)$$

The intensity, in terms of spectral density(ρ), can be expressed as:

$$I_D(\omega, k) = \frac{R}{2} \langle \left| \frac{\rho(k, \omega)}{2} r_R e^{i2kz_R} + \frac{\rho(k, \omega)}{2} \sum_{n=1}^N r_{s_n} e^{i2k(z_{s_n} - \omega t)} \right|^2 \rangle_T \quad (2.24)$$

If the Signal Spectrum is expressed as the ensemble average of the power spectrum and assuming the light source has a Gaussian shape, across the wave number domain, then frequencies do not modify the result. It will be only related to the wave number k .

$$S(k) = \langle |\rho(\omega, k)|^2 \rangle_T \Rightarrow S(k) = \frac{1}{\Delta k} \frac{1}{\pi} e^{-\left(\frac{k-k_0}{\Delta k}\right)^2} \quad (2.25)$$

From the Temporal Coherence Function $g(z)$ equation 2.5 and the Signal Spectrum $S(k)$.

$$g(z) = e^{-z^2 \Delta k^2} \Rightarrow \text{F.T.} \Rightarrow S(k) = \frac{1}{\Delta k} \frac{1}{\pi} e^{-\left(\frac{k-k_0}{\Delta k}\right)^2} \quad (2.26)$$

Applying $S(k)$ to Intensity:

$$I_{D_k} = \frac{R}{2} [(r_R + r_{s_1} + r_{s_2} + r_{s_3} + \dots + r_{s_n}) + \sum_{n=1}^N \sqrt{\frac{1}{r_R r_{s_n}}} (e^{i2k(z_R - z_{s_n})} + e^{-i2k(z_R - z_{s_n})}) + \sum_{m=n=1}^N \sqrt{\frac{1}{r_{s_n} r_{s_m}}} (e^{i2k(z_{s_n} - z_{s_m})} + e^{-i2k(z_{s_n} - z_{s_m})})] \quad (2.27)$$

The information required to build the sample image is located at the second term (blue section), the interference between the sample layers and the reference arm. The DC term (red section) has to be removed in order to generate a clear image. The last section is generated by the interference generated between the sample layers; it is very small and usually does not cause too much noise.

2.1.4 Swept Source OCT

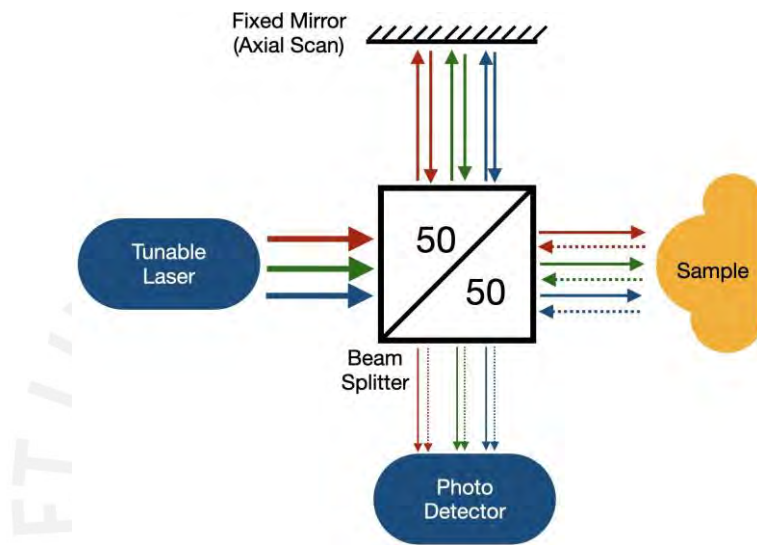


Figure 2.13: Swept Source OCT diagram. Spectrometer and CCD camera are replaced by a photo-detector and a swept source laser.

Swept-source OCT (SS-OCT) is a variation of the SD-OCT technique in which a tunable (swept-source) laser is used as a light source instead of a superluminescent diode. With this light source, the spectrometer and the CCD are no longer required. The usual interferometer array is used, but a photo detector replaces the CCD camera (figure 2.13).

The SS-OCT architecture is simpler than SD-OCT but it keeps the high resolution and fast acquisition characteristics; the laser-swept frequency determines the axial scan speed. The system design uses this architecture.

SD-OCT and SS-OCT are also known as Fourier-domain OCT because they work in the frequency domain. They converted the optical path difference between reference and sample layers into a phase-shifting value.

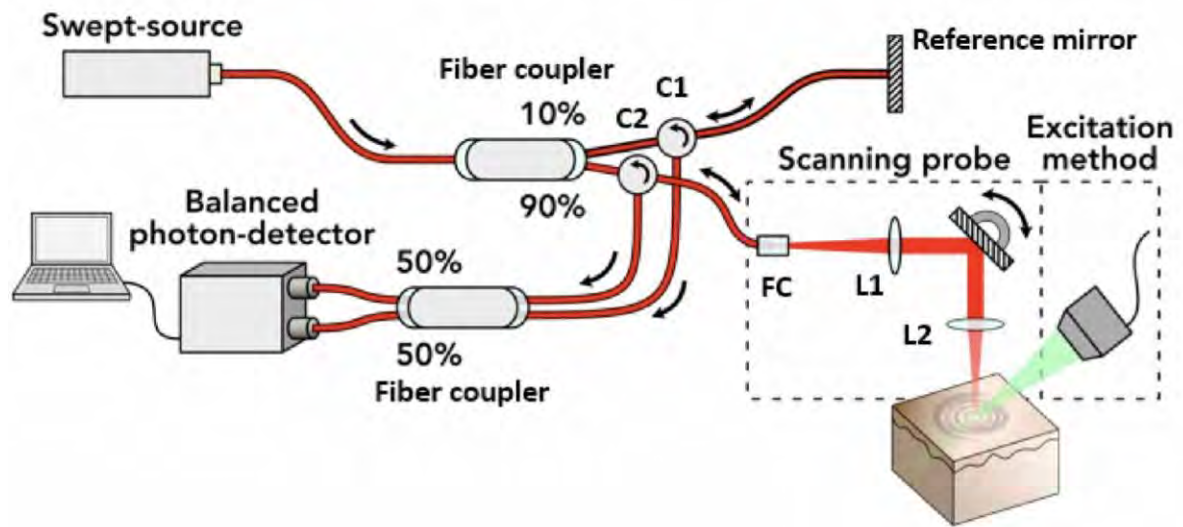


Figure 2.14: Swept Source OCT system basic schematic diagram. Two fiber couplers (bidirectional beam splitters) and two circulators are used to configure a Mac-Zehnder interferometer schema. With this arrangement the first fiber coupler is used to split the swept source beam, one for reference and the other for the sample, and the second one is used to combine (interfere) signals from reference and sample. SS - OCT requires a synchronization with the computer to acquire the scanned information at the swept start - Image taken from "Wave-based optical coherence elastography: the 10-year perspective" [33].

The main difference between SS-CT and SD-OCT is that SS-OCT uses a tunable laser as light source which eliminates the need of the spectrometer and the CCD camera. A photo detector is used to capture the interference spectrum. The architecture is simpler than SD-OCT without sacrificing scan speed.

Nevertheless, the light source is more complex than the one used on SD-OCT systems. In this architecture a Swept-Source laser is used. The swept laser source varies its wavelength in a certain range, simulating low-coherence SLD sources. The axial scan speed is directly related to the sweep speed; actual systems provide between 50,000 and 400,000 sweeps per second.

SS-OCT Interferometry

For SS-OCT the same principles as for SD-OCT apply. The reference and backscattered sample light beams are combined to analyze their interference. In SD-OCT a CCD received the interference spectrum divided by wavelength on the spectrometer, but for SS-OCT the spectrum will also be divided by spectrum but not in the space, but in the time domain. The swept laser source will sweep its wavelength between a range.

Even though this configuration belongs to the Fourier Domain OCT systems, the diagram looks similar to an TD-OCT system with a fixed reference mirror. The low coherence will be provided by the sweep sequence from the laser source.

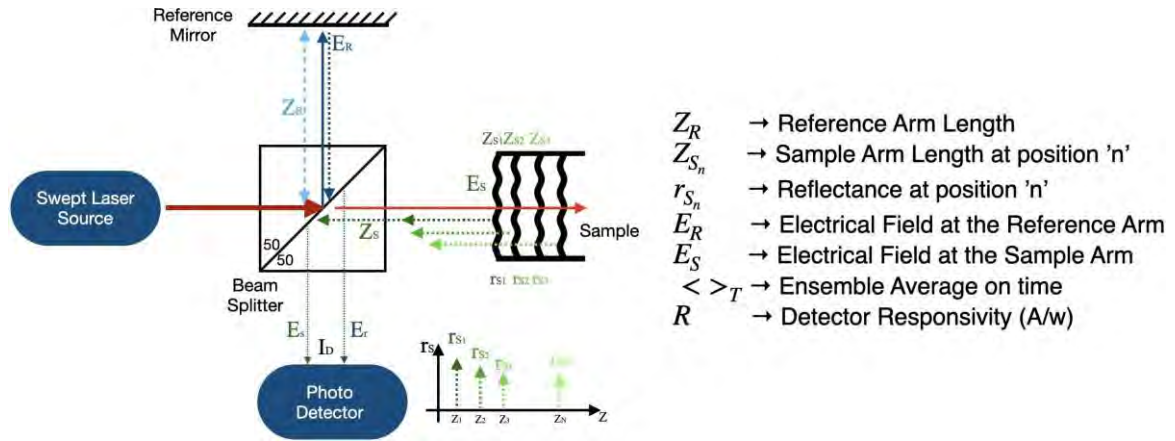


Figure 2.15: SS-OCT Interference. Each sample layer reflects the light beam from a different depth as shown in figure 2.2

Interferometry The electric field at the detector will be expressed by the electric fields from the sample and reference arms.

$$\mathbf{E}_D = \mathbf{E}_S + \mathbf{E}_R \quad (2.28)$$

The reflectivity from the sample will be the sum of the reflectivities from all tissue layers as shown in figure 2.15.

$$\begin{aligned} r(Z_s) &= r_{s_1} + r_{s_2} + r_{s_3} + \dots + r_{s_n} \\ r(Z_s) &= \sum_{n=1}^N \partial(Z_s - Z_{s_n}) \end{aligned} \quad (2.29)$$

Then the electric fields at reference and sample arms will be expressed as:

$$\mathbf{E}_R = \frac{\mathbf{E}_0}{\sqrt{2}} r_R e^{i2kZ_R} \quad \text{and} \quad \mathbf{E}_S = \frac{\mathbf{E}_0}{\sqrt{2}} [r_{z_s} \otimes e^{i2kZ_s}] \quad (2.30)$$

The Intensity at the detector (from equation 2.28):

$$I_D \approx |\mathbf{E}_D|^2 = R |\mathbf{E}_S + \mathbf{E}_R|^2 \quad (2.31)$$

The intensity, in terms of spectral density(ρ), can be expressed as:

$$I_D = \frac{R}{2} \left\langle \left| \frac{\rho(k, \omega)}{2} r_R e^{i2kZ_R} + \frac{\rho(k, \omega)}{2} \sum_{n=1}^N r_{s_n} e^{i2k(Z_{s_n} - \omega t)} \right|^2 \right\rangle_T \quad (2.32)$$

The swept laser source emits one wavelength at a specific time (λ_0 at t_0) and another one at the next time (λ_1 at t_1), sweeping the entire range in a specific period. The assembled average covers the entire period, which also covers all wavelength ranges from the swept source. The result will be the same as the SD-OCT equation 2.27

$$I_{D_k} = \frac{R}{2} [(r_R + r_{S_1} + r_{S_2} + r_{S_3} + \dots + r_{S_n}) + \sum_{n=1}^N \sqrt{r_R r_{S_n}} (e^{i2k(Z_R - Z_{S_n})} + e^{-i2k(Z_R - Z_{S_n})}) + \sum_{m=n=1}^* \sqrt{r_{S_n} r_{S_m}} (e^{i2k(Z_{S_n} - Z_{S_m})} + e^{-i2k(Z_{S_n} - Z_{S_m})})] \quad (2.33)$$

$$I_{D_k} = \frac{R}{2} [r_R + \sum_{n=1}^* r_{S_n}] + \frac{R}{2} \left[\sum_{n=1}^* \sqrt{r_R r_{S_n}} (e^{i2k(Z_R - Z_{S_n})} + e^{-i2k(Z_R - Z_{S_n})}) + \sum_{m=n=1}^* \sqrt{r_{S_n} r_{S_m}} (e^{i2k(Z_{S_n} - Z_{S_m})} + e^{-i2k(Z_{S_n} - Z_{S_m})}) \right] \quad (2.34)$$

$$I_{D_k} = \frac{R}{2} [r_R + \sum_{n=1}^* r_{S_n}] + R \left[\sum_{n=1}^* \sqrt{r_R r_{S_n}} \cos(2k[Z_R - Z_{S_n}]) + \sum_{m=n=1}^* \sqrt{r_{S_n} r_{S_m}} \cos(2k[Z_{S_n} - Z_{S_m}]) \right] \quad (2.35)$$

The interference term used to generate the images is the second one, on blue. The first, in red, and the last one, in black, are unwanted components of the spectrum and will be removed at the data processing step.

The interference term consists of all the signals reflected by all layers of tissue. Each signal frequency is built on the optical path difference between the reference path and each sample layer ($Z = Z_R - Z_{S_n}$) and $k(\frac{2\pi}{\lambda})$. As the wavelength and Z_R are known, then Z_{S_n} can be calculated.

2.2 Optical Coherence Elastography (OCE)

OCE used an OCT system integrated with an elastography module. This module is used to stimulate the tissue sample with mechanical stimulus. OCE prefers non-contact stimulus in order to avoid intrusion from the mechanical source/tool. Two of these non-contact techniques are air pulses and ultrasound waves, depending on the biomechanical parameters that are intended to measure. The OCT part of the system is responsible for capturing the tissue response to mechanical stimulation.

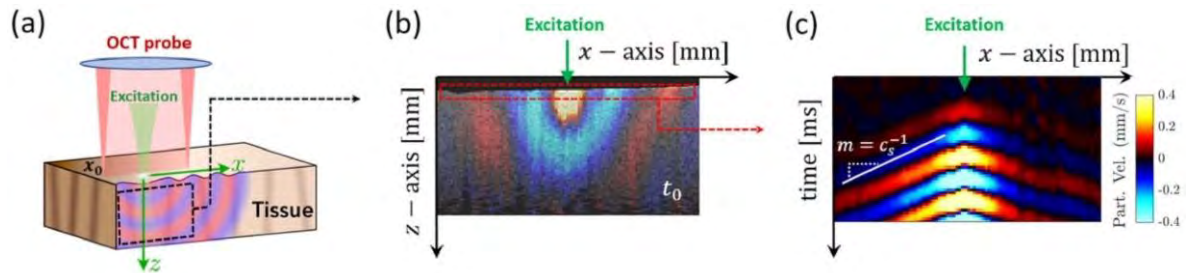


Figure 2.16: Figure (a) shows an OCE system analyzing a tissue. The OCT probe (red rays) is responsible for capturing the tissue structure and its response to the mechanical stimulus (green rays). The tissue receives the mechanical waves and propagate it through the axial (Z) and lateral (X) axes. Figure (b): From the cross section scan obtain in figure (a), an horizontal (X) section is analyzed at a specific moment (t_0). Figure (c) analyzes the same (X) section from figure (b), but in a time period. With this information a speed map can be generated - Image taken from "Wave based OCE the 10 year perspective" [33].

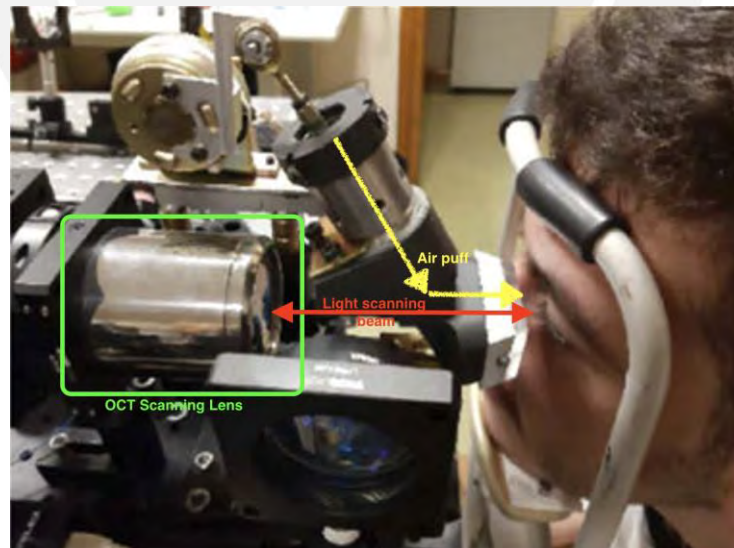


Figure 2.17: On this OCE Prototype air puff module (yellow arrow) has an aperture that let the optical axis (red arrow) from the OCT scanning lens (green section) reach the eye; besides the optical-air puff confocal alignment, the air stimulus has to be synchronized with the OCT data capture process so the system can generate images for the complete tissue movement. This arrangement is used, also in other elastography-OCT systems - Image taken from "Multi-meridian corneal imaging of air-puff induced deformation for improved detection of biomechanical abnormalities" [20].

In an OCE system using ultrasound waves, the wave generator unit (transducer) must be aligned with the optical axis of the OCT system, following the same criteria as the one shown in figure 2.17. In this case, the transducer has a hollow center to allow the light beam to reach the tissue.

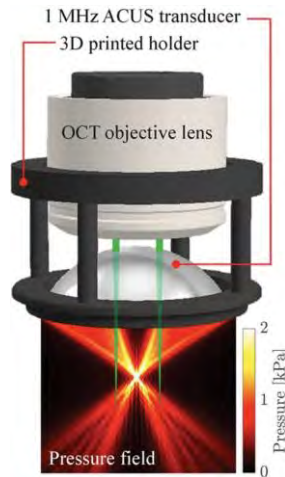


Figure 2.18: Ultrasound OCE Lens Array - Image taken from "Confocal air-coupled ultrasonic optical coherence elastography probe for quantitative biomechanics" [34].

A custom-made holder interfaces the optical system with the ultrasound transducer. The sample tissue must be located at the focal point of the lens system and at the focal point of the transducer.

The ultrasound wave will produce a mechanical stimulus, in form of waves, at the sampled focus point. The OCT strategy must capture the wave propagation without losing any section. In order to perform this action, a specific Acquisition Mode must be selected.

The ultrasound transducer has a holed center and it is, also, concentric with the OCT scan lens. The OCT must not be blocked by any element in order to correctly scan the sampled tissue.

2.3 Acquisition Modes and Protocols

OCT scans axial lines each time. In order to generate sections, the probe has to be moved across the tissue repeating axial scans. There are different techniques than can be used to acquire these B-lines; as ultrasound waves will be used to stimulate tissues, the wave speed propagation has to be measured as well as the motion.

2.3.1 B-mode Acquisition

A collection of A-scans across a surface line is called B-scan or cross section. In this mode, a two-dimensional (2D) area is scanned.

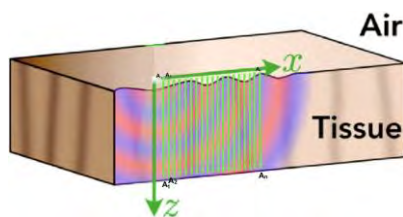


Figure 2.19: B-Scan on a tissue - Image adapted from " Wave-based optical coherence elastography: the 10-year perspective" [33].

In this acquisition mode, a series of A scans will be performed. This line (X axis) combined with the A scan (Z axis) constructs a cross-sectional image.

In this acquisition mode, there is no A-scan repetition; one point is scanned just once, and then the scanning process takes place at the next scanning point.

The number of samples, A-scans, will be determined prior to the start of the acquisition process. This will construct a line on the X -axis, a line of "n" points, where each point is a sample.

2.3.2 M-mode Acquisition

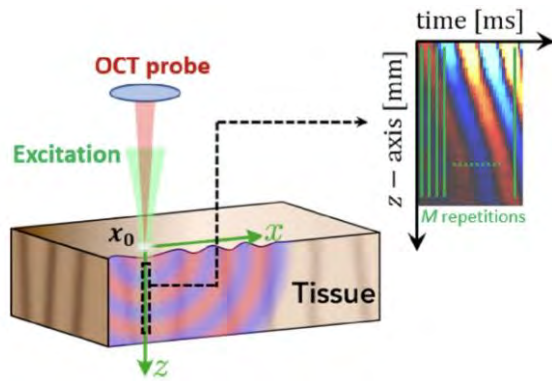


Figure 2.20: M-Mode Acquisition - Image taken from "Wave-based optical coherence elastography: the 10-year perspective" [33].

M-mode acquires the same axial line for a specific time period. In an OCT environment acquisition will provide the same measurement unless that section experiences motion (The M stands for MOTION).[33]

In OCE the section will present motion, due to the mechanical excitation source (an ultra sound wave). The M mode acquires the same vertical line (A line) for a specific time period. In an OCT environment, acquisition will provide the same measurement unless that section experiences motion.

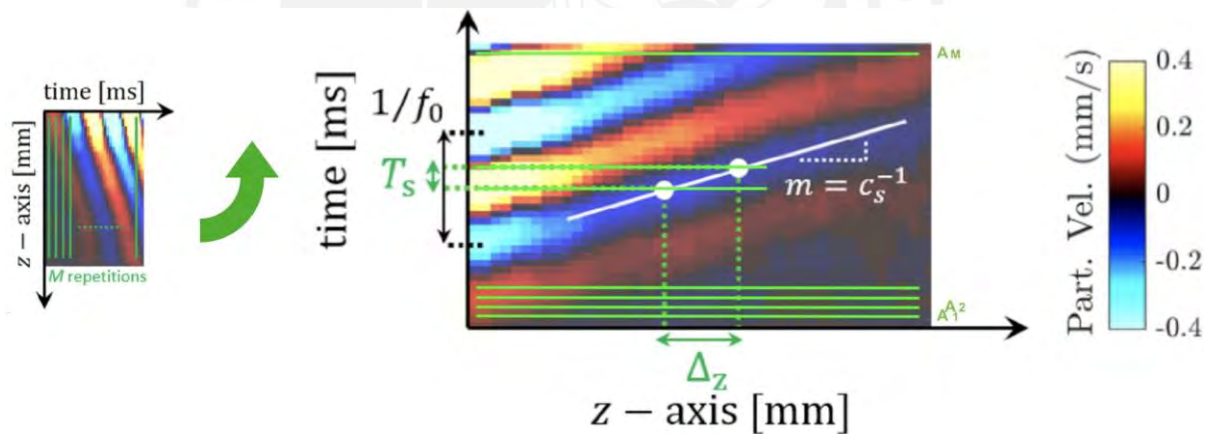


Figure 2.21: M-Mode Analysis. From the multiple A-scans obtained, we can calculate the inverse of the wave velocity by calculating the pendent between the time period and the distance difference Δz in the same period. The image is generated with colors based on the color bar assumed - Image modified from "Wave-based optical coherence elastography: the 10-year perspective" [33].

2.3.3 MB-mode Acquisition

Combining B-Mode and M-Mode acquisition modes provides a way to scan a sample point for a complete period to examine its behavior. Once this point has been completely scanned, the next point will be examined. This operation will continue for the number of times that equals the number of samples that need to be examined on the X-axis line.

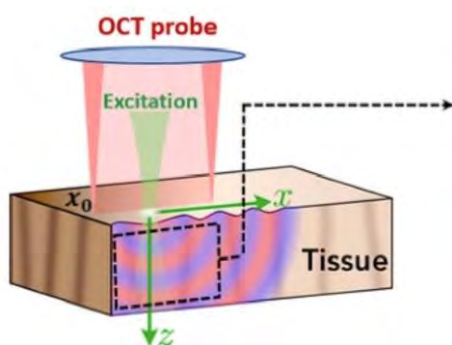


Figure 2.22: MB-Scan - Image taken from "Wave-based optical coherence elastography: the 10-year perspective" [33].

As portions of the sampled tissue need to be analyzed, cross sections (B-scan) have to be measured. Several A-scans (Z-axis) will be taken across the X-axis. This is an expansion of the M-mode into B scans to get the MB-mode acquisition.

The excitation wave is applied to the sampled tissue in order to analyze the mechanical characteristics.

When the M-mode is expanded to B-scans, the MB mode acquisition is obtained.

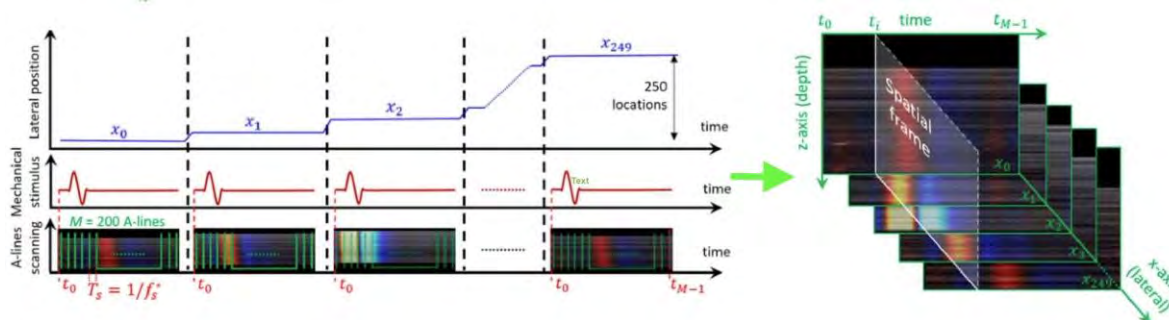


Figure 2.23: MB-mode acquisition scan process - Image taken from "Wave-based optical coherence elastography: the 10-year perspective" [33].

In this example, an excitation wave is applied to the sampled tissue and M-mode acquisition is applied, but it will be repeated in adjacent locations. In figure 2.23 example, 250 locations have been defined on the X axis (X_0 to X_{249}) creating 250 A-scans (spatial frames) that cover the selected area in the sample tissue.

2.4 Data processing

As mentioned in the SD-OCT interferometry (Section 2.1.3), acquired signals have unwanted components that need to be removed before clear images can be generated.

The interference signals generated by OCT systems have to be acquired and processed in order to generate images. These signals have DC, also known as background components, that have to be removed as a first step. The second step is only required if the interference signal was not acquired with a k-clock (provided by the light source); in those cases, a k-linearization process has to be applied to the new signal obtained from the DC removal process. The last step for the data processing step is to apply a Gaussian-type window.

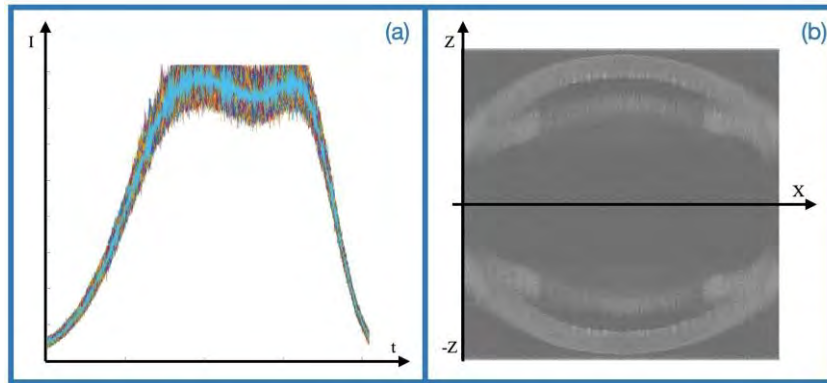


Figure 2.24: Figure (a) shows an interference signal, from a cornea, captured by an OCT system. Figure (b) shows the image generated from the interference signal, using the Fourier Transform (generating a mirror image).

2.4.1 DC Removal

As previously mentioned, the DC component (equation 2.10) has to be removed from the acquired signal. Two methods can be used for this purpose, a background measurement or an average calculation. The first method requires the recording of interference signals without a sample; a scan process with the reference arm blocked, a second one with the sample arm blocked and a third one with both arms blocked.

R = Signal with the Reference Arm blocked: $B_{Sample} + B_{noise}$

S = Signal with the Sample Arm blocked: $B_{Reference} + B_{noise}$

N = Signal with both arms blocked: B_{noise}

Background signal $B_K = R + S - N$

The background component B_K will be subtracted from every scan.

The second method to subtract the DC component is to calculate an average signal from all the scanned signals and subtract this average from the measurements. This method does not require one to pre-set the system every time it will be used.

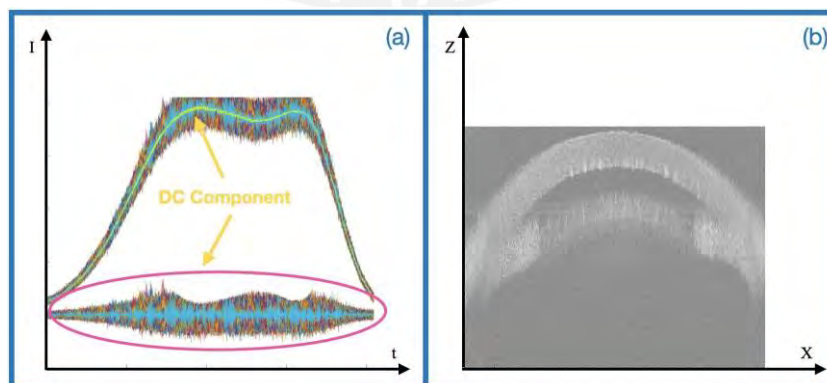


Figure 2.25: Figure (a) shows the calculated DC component (in yellow). After subtracting DC from the raw signal, the interference is showed at the bottom of that figure. Figure (b) shows the new image from the data without the DC component and without the mirror image.

2.4.2 Remapping on k-domain (k-linearization)

As previously mentioned, there are some light sources that do not provide a k-clock signal for data processing. In those cases, after removal of the DC component, the acquired signal has to be relinearized in the wave number (k) domain instead of the wavelength domain.

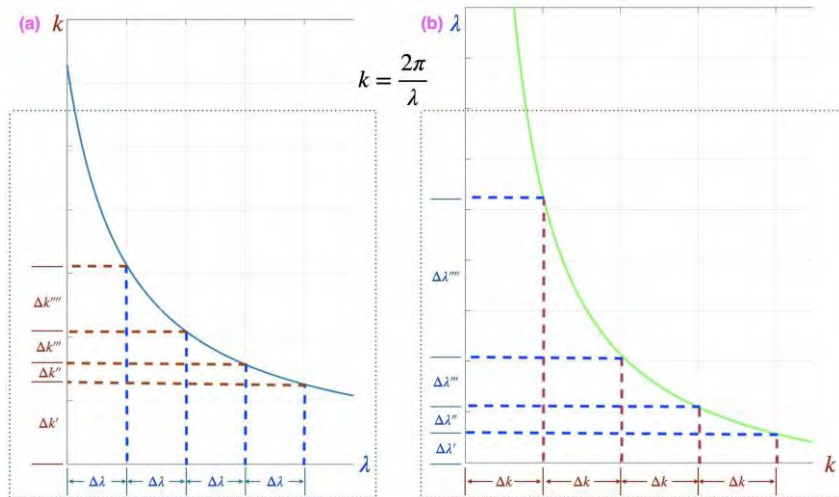


Figure 2.26: k-linearization process: from λ domain to k domain. Figure (a) shows the interference spectrum captured by an oscilloscope. The signal runs in time domain. Wavelengths are also equally distributed in time; the correspondence between wavelength and wave number is provided by equation $k = \frac{2\pi}{\lambda}$. The k value for each sample is not equally distributed. Figure (b): From Intensity equation 2.18, the Intensity at the detector depends on wave number (k), not in wavelength domain. A regular k distribution is required, an interpolation can be applied.

For the k-linearization process, a vector has to be applied to the signal. This vector has to be calculated from the signals obtained from the sample.

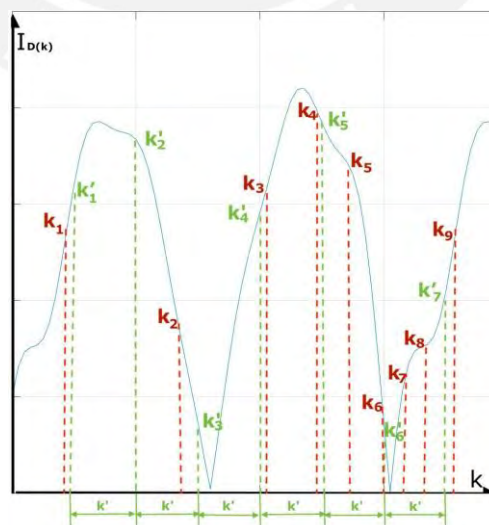


Figure 2.27: K-linearization example. $k_1, k_2, k_3, \dots, k_n$ have an irregular distribution. After the signal is interpolated, a new set of k values are generated $(k'_1, k'_2, k'_3, \dots, k'_n)$

2.4.3 Windowing

Ideally, coherent and low-coherent light sources have Gaussian shapes. Nevertheless, not all sources meet this case, or deviations can be found in others. These variations will produce spurious frequencies, displayed as sidelobes when the Fourier Transform is applied. To reduce this unwanted effect, a Gaussian-type window can be applied to the already processed signal as a final step before generating the images.

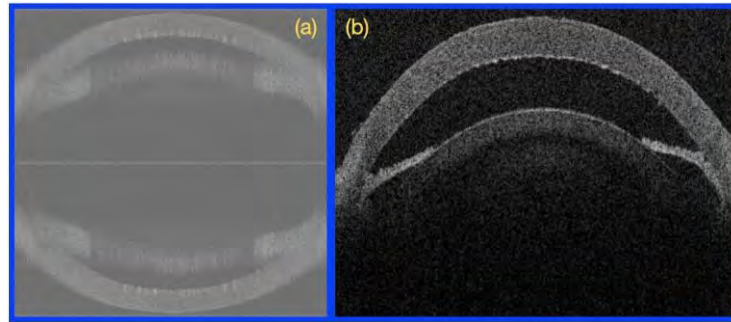


Figure 2.28: Figure (a) shows the image generated from the raw data. Figure (b) shows the image generated from the processed data (DC subtraction, k remapping and windowing).

2.5 Scanning patterns

To generate cross-sectional images, the light beam must cover a line over the sample tissue. This action is accomplished by a galvanometric mirror system that varies its position to cover the desired section. One mirror will generate a line movement. If a different pattern is desired, two mirrors will be needed, one for the X axis and the other for the Y axis.

Crosshair pattern For a crosshair scanning pattern, the two mirror galvanometer system has to be controlled with the following voltage pattern:

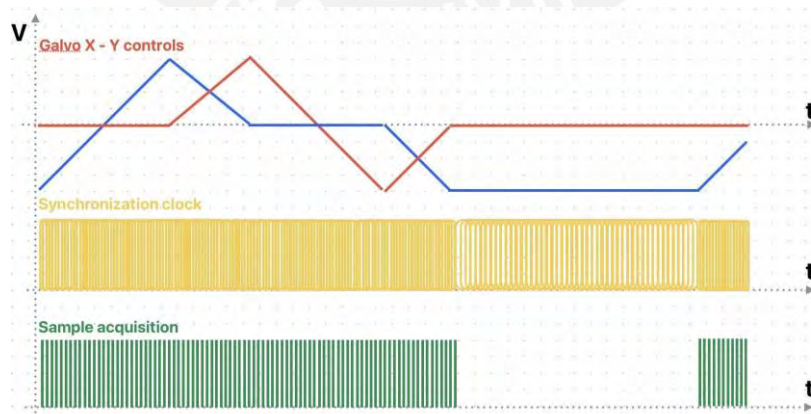


Figure 2.29: Voltages applied to X and Y mirrors to create a Crosshair scan pattern. Blue line shows the voltage pattern applied to the X-axis mirror. Red line corresponds to the Y-axis mirror. The synchronization clock (yellow pattern), indicates the mirror movement duration as well as the sample data acquisition (green pattern).

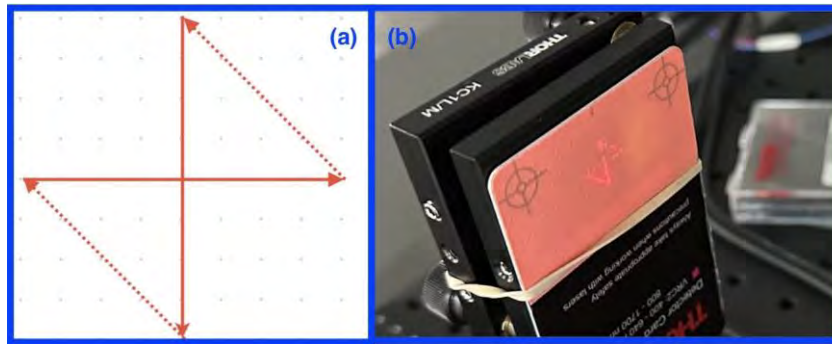


Figure 2.30: Figure (a) show the result for the applied voltage pattern on figure 2.29. Figure (b) shows the same pattern applied from the system on an IR detector Card. The transition lines, showed as dotted in figure (a), are not taking in consideration for image processing.

By modifying the voltages applied to the galvanometer mirrors (X and Y), different scan patterns can be set. A 3D pattern required a series of B scans, one at the following line from the previous line.

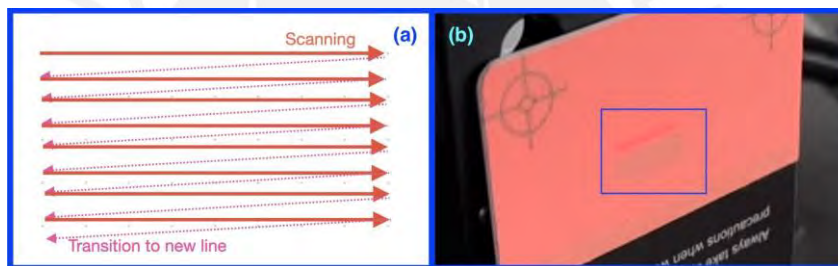


Figure 2.31: Figure (a) shows the scan pattern for a 3D image. Figure (b) shows a bright red line at the top of a dark rectangular section on the IR detector card . This IR card becomes a dark after an IR beam is received; the dark rectangular section was hit by the IR line beam one line at a time.

Chapter III

System Design and Implementation

A basic OCT system is composed by a light source, a beam splitter, a Reference arm, a Sample Arm, an interferometer array and a acquiring/processing section (usually a Photo Detector or a Spectrometer with a computer interface). An ultrasound module (elastography) added to the Sample Arm provides the ability to detect the mechanical properties of the sample.

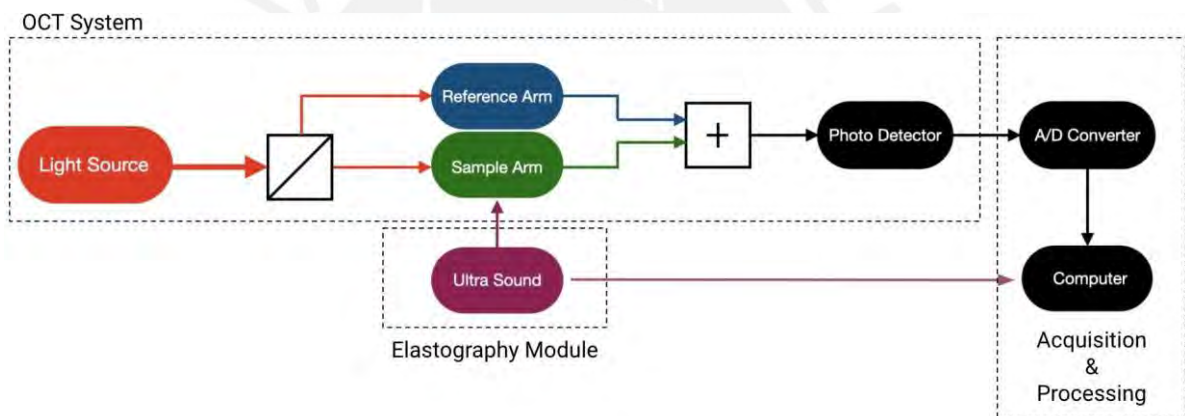


Figure 3.1: OCT/E System Block Diagram showing its main components, sample and reference arm, beam splitter, mixer, photo-detector, acquisition and processing and the elastography module.

3.1 Design Considerations

Skin scanning procedures can last for a few minutes, but eye scanning procedures cannot take more than 2 seconds to complete. The procedure scan time will maintain the same limit. This time is due to the fact that patients cannot keep their eyes open, without blinking, for longer periods. From all OCT techniques reviewed in the previous chapter, Swept Source OCT was selected because of its simple architecture and its high axial scan rate (from 50 kHz up to Megahertz).

3.1.1 Parameters Selection

Considering that the OCT system will be integrated with an elastography module to perform tissue scans in human patients, the following considerations have been taken:

Table 3.1: System design requirements

Parameter	Limits	Description
Scan duration	< 2 s	Faster than human blinking
Optical power	< 15.6 mW	Table A.3 of IEC 60821-1:2014
Resolution	< 20 μm	In order to display the corneal structure
Penetration	1 ~ 2 mm	To cover the whole corneal thickness
Lateral Field of View	>13 mm	To cover the whole cornea diameter
Phase stability		Required for ultrasound waves tracing
Wavelength	> 700 nm	Must not be visible
Working distance	> 50 mm	Space needed for elastography module

3.1.2 Light Source Selection

The first key element that has to be selected is the light source. As the system will be used for corneal scanning, the wavelength must be outside the visual spectrum to avoid blinking of the eyes. The system must have the maximum resolution.

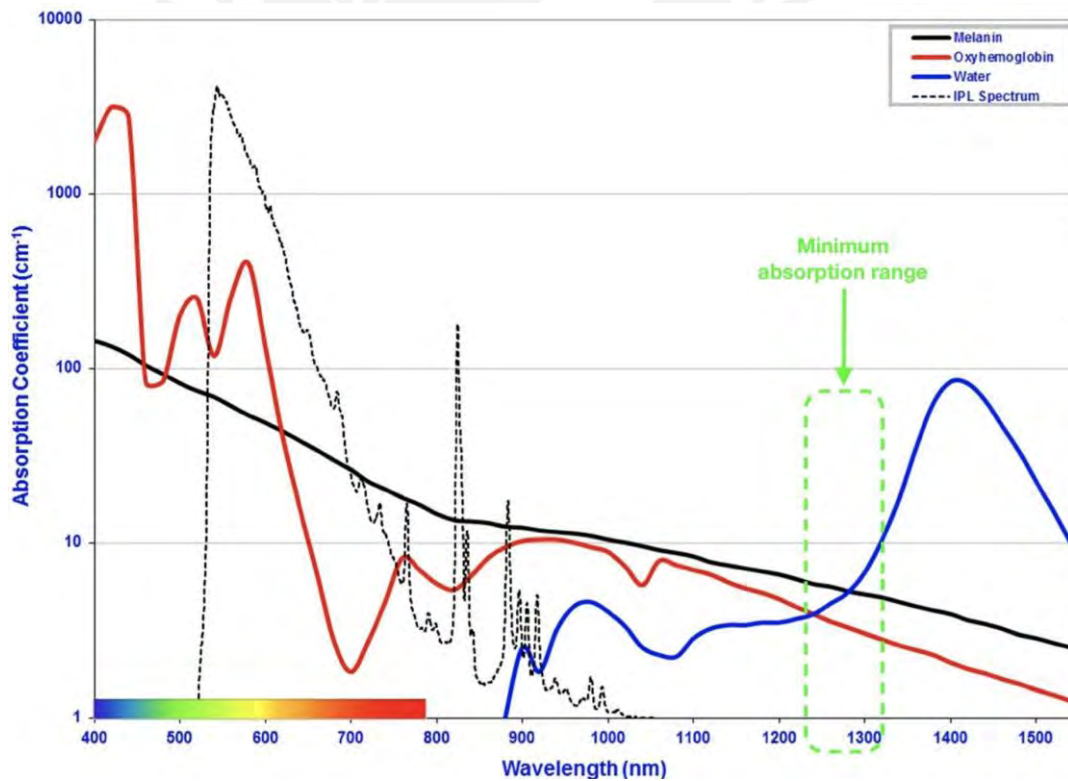


Figure 3.2: The optical window figure shows the light absorption caused by the principal components of biological tissues - Melanin and oxyhemoglobin(HbO_2). Around 1300 nm the absorption from the biological tissue components is minimum. At the same time, the water has a relative absorbance between 1 and 2. Longer wavelengths have higher absorbance - Image modified from "Effect of wavelength and beam width on penetration in light-tissue interaction using computational methods"[35].

With the central wavelength selected and the resolution requirements from Table 3.1, the resolution can be calculated from Figure 2.9.

$$\Delta Z = 2\ln(2)\frac{\lambda_0^2}{\pi\Delta\lambda} \quad (3.1)$$

Using a system with 100 nm of bandwidth, the resolution will be:

$$\Delta Z = 2\ln(2)\frac{(1300\text{nm})^2}{\pi 100\text{nm}} = 7.4574\mu\text{m} \quad (3.2)$$

From figure 2.9, the lateral resolution will be determined by:

$$\delta X = 37\frac{\lambda_0}{\text{NA}} \quad (3.3)$$

As the requirement table 3.1, the resolution must be finer than 20 μm . From equation 3.3

$$20\mu\text{m} > 37\frac{1.3\mu\text{m}}{\text{NA}} \quad \text{then,} \quad \text{NA} > 2.405 \quad (3.4)$$

This means that the scanning lens must have a Numeric Aperture (NA) bigger than 2.405. For the Lateral Resolution, the equation (from figure 2.9):

$$\text{FOV}_{\text{Lateral}} = 2f\theta_{\text{max}} \quad (3.5)$$

From requirement table 3.1:

$$13\text{mm} < 2f\theta_{\text{max}} \quad \text{then,} \quad 6.5\text{mm} < f\theta_{\text{max}} \quad (3.6)$$

The scanning lens must have a product of its focal point and the maximum angle of inclination bigger than 6.5 mm. For the Axial FOV, the following equation (from figure 2.9) is used:

$$\text{FOV}_{\text{Axial}} = \frac{0.221\lambda_0}{\sin^2\left[\frac{\sin^{-1}(\text{NA})}{2}\right]} \quad (3.7)$$

In order to have phase stability, a Fourier Domain OCT (FD-OCT) system will be used. The most common FD-OCT variations are the Spectral Domain and swept Source OCT. SS-OCT has an axial scan rate from 50 KHz up to MHz. From the requirement table, the scan procedure must have a duration shorter than 2 seconds. A 200KHz rate-swept laser source produces a full cycle in just 5 μs . This rate allows the system to perform a maximum of 200,000 A-scan points in one second.

SS-OCT systems also use photodetectors instead of CCD or CMOS cameras. A spectrometer is also not required. With those conditions, the system light source selected is the Thorlabs 1300 nm MEMS-VCSEL (Micro Electro Mechanical System - Vertical Cavity Surface Emitting Laser) system with the following specifications:

Table 3.2: Thorlabs SL132120 specifications [36]

	Min	Typical	Max
Center Wavelength	1280 nm	1300 nm	1320 nm
Wavelength Sweep Range (-10 dB)	95 nm	100 nm	N.A.
Average Output Power	20 mW	25 mW	30 mW
Trigger Wavelength	1295 nm	1300 nm	1305 nm
Sweep Rate	-	200 KHz	-
OCT Imaging Depth Range	-	8 mm	-

3.1.3 Interferometry Array

As previously mentioned, OCT is based on optical wave interferometry, a technique that mixes two copies of a light beam with different paths. One of them has fixed length and reflectivity (called Reference) and the other will be used to irradiate a sample. There are different types of interferometer that are used for different purposes. For OCT two of them are the most common, Michelson and Mach-Zehnder.

Michelson Interferometer

The Michelson interferometer is an array of mirrors and beam splitters. Its base concept is to divide the source beam in two. Each of the new beams will follow a different path and, at the end of them, the two beams will be combined in a receptor.

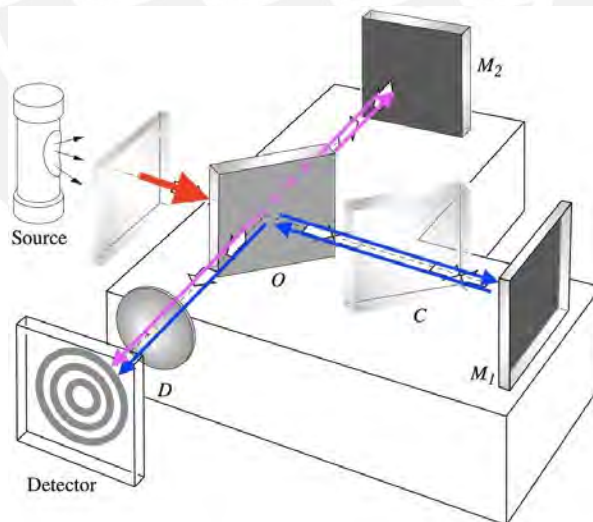


Figure 3.3: A source emits a light beam (red) that is splitted in two by a beam splitter (O). One of the new beams (blue) goes to mirror 1 (M_1) where it is reflected back; this beam and its reflection travels through a compensator block (C) in order to compensate the beam splitter thickness traveled by the second created beam (pink). This second beam travels to mirror 2 (M_2) and then it is reflected back to the interferometer through which it will reach the detector (D). If the distances to mirrors M_1 and M_2 , positive interference patterns will be created at the detector (in this case concentric circles) - Image modified from "Optics - Fifth edition"[37]

Mach-Zehnder Interferometer

A Mach-Zehnder interferometer is also an array of mirrors and beam splitters, but in this technique, each new beam will travel in just one direction until it reaches the combination element before the detector.

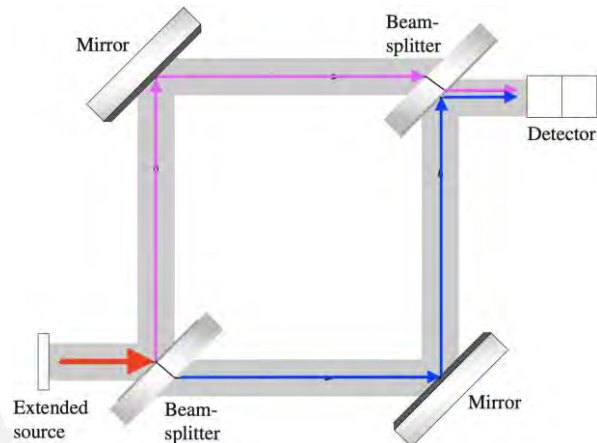


Figure 3.4: The source (red) is splitted in two light beams. One of the new beams (pink) goes to one mirror and then it reaches a second beam splitter that serves as a combination arrangement. The other light beam (blue) goes to the second mirror and then to the last beam splitter to be combined with the other light beam - Image modified from "Optics - Fifth edition"[37]

Interferometers can be implemented on free space (air) or on fiber optic components. Free space interferometers are more susceptible to vibrations and they have bigger volumes than fiber optic interferometers. For our system, fiber optic devices will be preferred over free-spaced ones. Thorlabs fiber coupler with a 50% / 50% division will be used. The fiber coupler routes are shown in figure 3.5.

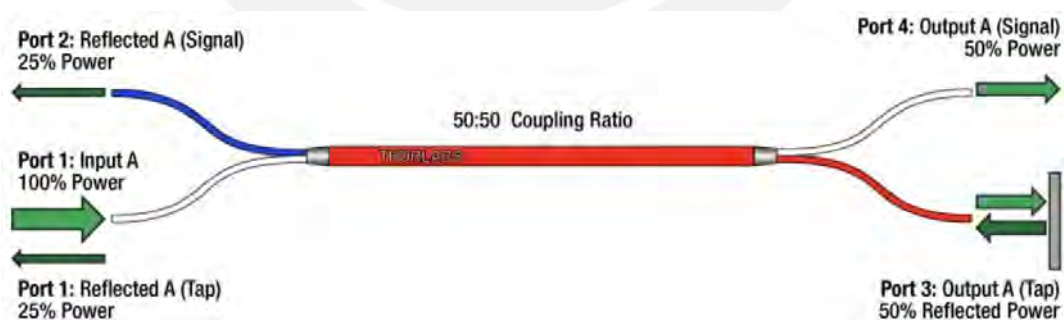
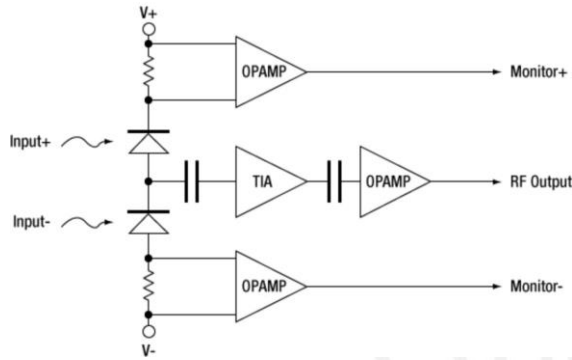


Figure 3.5: Thorlabs Fiber Optic Coupler Flow. This coupler has a bidirectional configuration with two ends at each side; they can be used in both directions. The center wavelength must match the source laser (1300 nm) as well as its connectors type - Image adapted from "Thorlabs web site" [36].

A Michelson interferometer, based on fiber optic components, was selected for the design of the OCT system.

3.1.4 Photodetector

The photodetector receives the optical interference signals and converts them to an electrical one.



The swept laser source SL132120 recommends options for a Dual Balanced Detector. The first one is an embedded one available at the SL132121 laser source and the other one is the external PDB480C-AC Fiber Coupled Balanced Amp. Photodetector, 1.6 GHz, In-GaAs, 1300 nm. The balanced photodetector embedded in the SL132121 has the same characteristics as the external PDB480-AC unit.

Figure 3.6: Thorlabs PDB480-AC External Dual Balanced Photo-detector - Image taken from "Thorlabs web site" [36].

The selection was based on flexibility and reliability. If the photodetector on SL132121 fails, the whole equipment must be replaced.

3.2 OCT Design

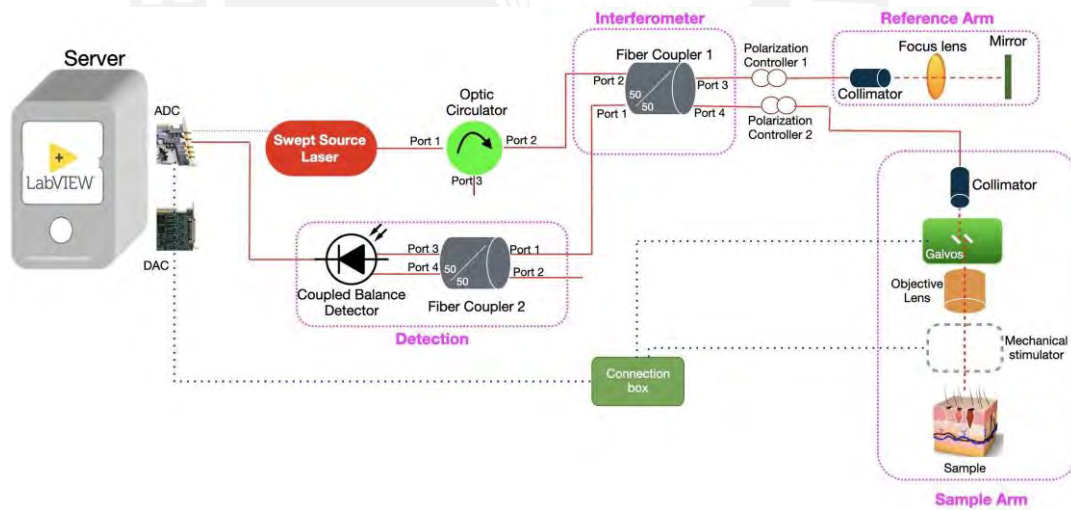


Figure 3.7: OCT design using a swept laser source and a Michelson interferometer array. An Optic circulator is being used as an isolator to protect the laser source from back-reflection coming from the reference arm. Fiber coupler described in figure 3.5 are used as fiber couplers 1 and 2.

The Swept Laser Source is connected to an optical circulator for protection; during the initial tests, the laser source became disabled due to the back-reflection coming from the reference arm. With the optical circulator, the laser emission goes from port 1 to port 2 and the reflection, from port 2 to port 3. This arrangement was temporary until a fiber optic isolator was acquired.

This system, beside the light source, has four (4) sections that need to be designed: the interferometer (composed by the fiber-coupler 1), the reference arm, the sample arm, and the detection section (composed by the DB Photo detector and the fiber-coupler 2).

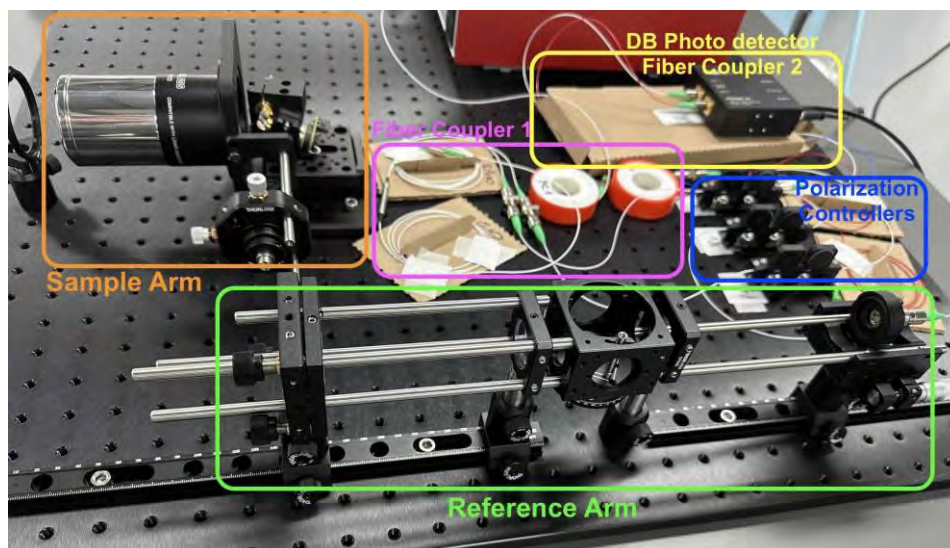


Figure 3.8: OCT system sections. The interferometer section, composed by the Fiber Coupler 1 is enclosed in the pink section. The reference arm is enclosed in the green section; it is composed by a collimator, a mirror and a focus lens. The sample arm, enclosed in the orange section, is composed by a scanning lens, a dual mirror galvanometric system and a collimator. The detection section, enclosed by a yellow square, is composed by a Dual Balanced photo detector and the fiber coupler 2.

3.2.1 Interferometer

The interferometer is the system component responsible for "mixing" the signals from the Reference and the Sample arms. Different configurations can be selected for this element, but for this system a Michelson type was selected. As the light source has a fiber optic output with FC / APC connector, this element is made with single-mode fiber optics (SMF-28).

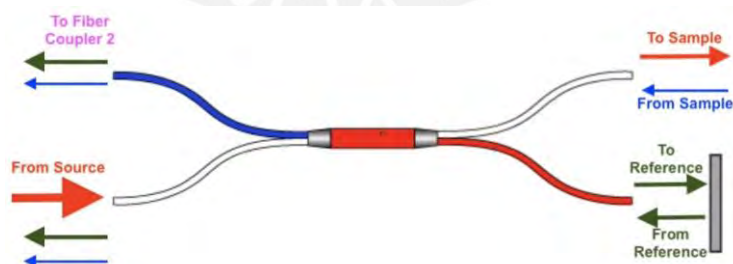


Figure 3.9: Fiber Coupler 1 is used as a Michelson interferometer with a 50:50 beam splitter. The laser source is connected to port 1 (left white leg) and the light flow is divided towards the reference arm, via port 4 (right red leg) and to the sample arm, via port 3 (right white leg). The backscattered light, from the sample, comes from port 3 and is directed to left ports 1 and 2. The reference reflection comes in port 4, and is also directed to the same left ports. The interference signal, from sample and reference, is created by the reference and sample mixture and divided by the fiber coupler; the resulted beams are sent to ports 1 and 2 (white and blue) - Image adapted from Thorlabs [36].

A circulator was placed between the light source and the interferometer to protect the laser source from the light beam reflected in port 1. Port 2 carries the interference signal to fiber coupler 2, which splits the spectrum in two beams that are connected to the dual-balanced photo detector. Two Polarization Controllers were installed on reference and sample arms, to control the delay the reference and sample spectrum's to reduce the DC component at the photo-detector inputs.

3.2.2 Reference Arm

This section is the part of the system used as a "reference" for the signal backscattered from the sample. To generate sample images, the interference signal, between reference and sample arms, requires that the reference and sample optical paths be of the same length.

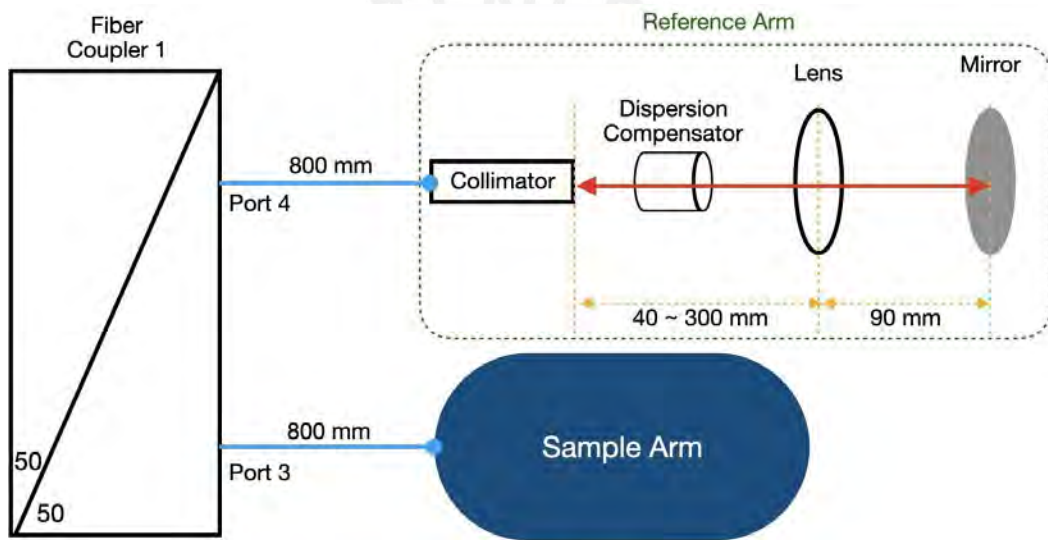


Figure 3.10: Reference Arm Length. The light beam from the laser source is divided in two paths; one is sent to the reference arm and the second one to the sample arm. Both light beams have to travel the same length in order to produce a detectable interference signal. As the fiber coupler has the same length for its 4 legs, the reference arm has to match the sample length. For this design, the reference arm can be set from 130 mm to 390 mm in length. The dispersion compensator refractive index (n) was not considered in the calculation due to its short length.

The reference arm has two main components: a collimator that sends the light beam to the mirror in a collimated condition and a mirror that reflects the beam back. There is an additional component, a focus lens used to concentrate the light beam in a spot located at the focal point; this component also allows the light to reach the lens in its Clear Aperture, instead of its center.

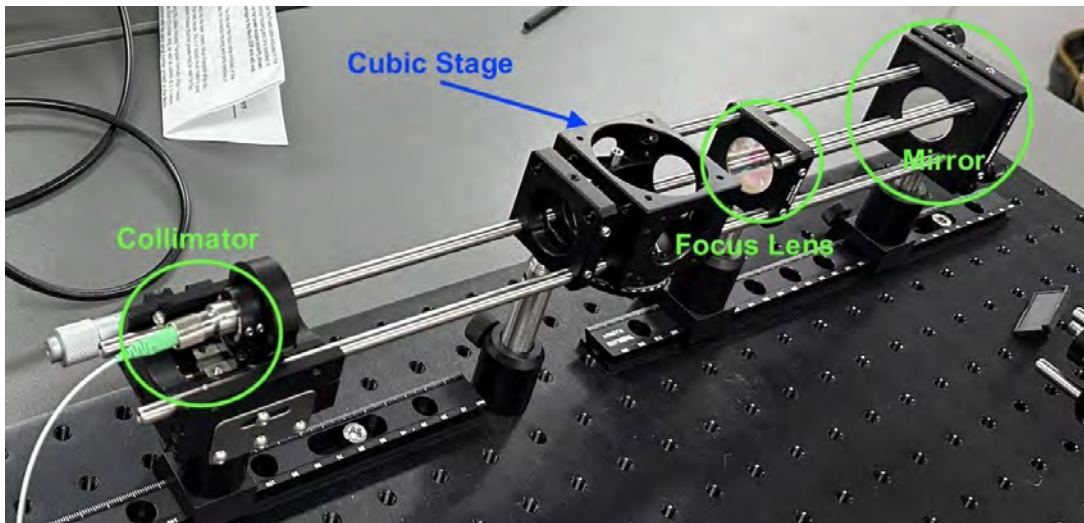


Figure 3.11: Reference arm composed by a collimator, a focusing lens and a mirror. The key component in the Reference arm is the distance between the collimator and the mirror that will be used to compare the sample back-scattered light; this length can be set from 130 mm up to 390 mm. The collimator receives the light beam from the Fiber Coupler 1, red port, and send it to the mirror; in theory only those two components are required, but the collimator does not have a perfect alignment with the mirror center. That is why a focusing lens was included, to concentrate the light beam into a single spot in the mirror. The mirror tilt can be adjusted to reflect the beam back to the mirror with the same angle or with a little tilt; this will cause that the reflected beam will not have the maximum intensity.

The focus lens focuses the light beam, even though the beam is not centered with the mirror, as shown in figure 3.12 (b).

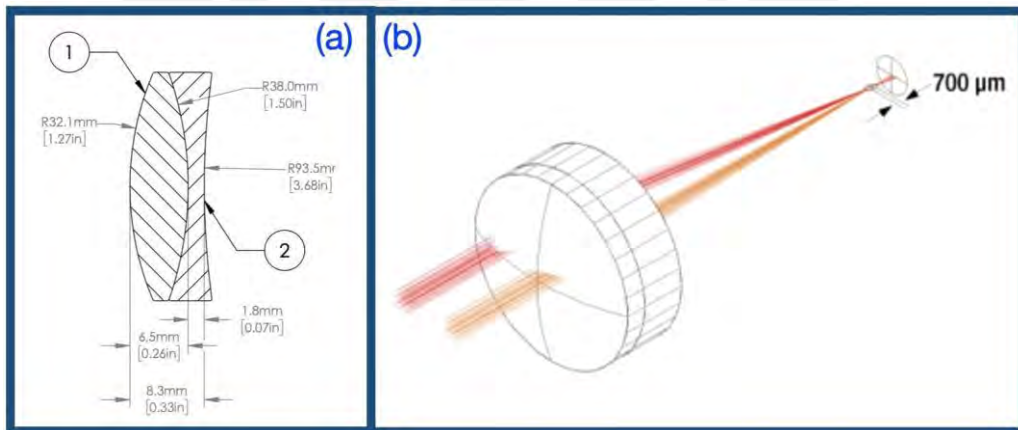


Figure 3.12: A focus lens is used to center the light beam into the mirror. Figure (a) shows the Thorlabs AC254-100C Doublet achromatic lens dimensions. Figure (b): AC254-100C facilitates the focusing of the light beam. Since the collimator has to be slipped to match the sample optical path length and also to characterize the system, a translation stage is used as the collimator support. This arrangement adds additional level of complexity to the collimator-mirror alignment. During the implementation it was not possible to get a proper alignment. Using the focus lens, the light beam reached the center of the mirror due to its centering properties - Images taken from "Thorlabs web site"[36].

- The lens specifications are the following:
- Wavelength: 1016 nm, 1330 nm, 1550 nm.
 - Focal length: 100.1 mm @ 1330 nm.
 - Back focal length: 90.4 mm.
 - Diameter: 25.4 mm.
 - Clear aperture: 22.86 mm.

The light beam reaches the reference arm through the collimator. This component has to be installed on a mobile mounting support. A dispersion compensator is used to provide the same dispersion as the one caused by the scanning lens in the sample arm; both are selected at the same time.

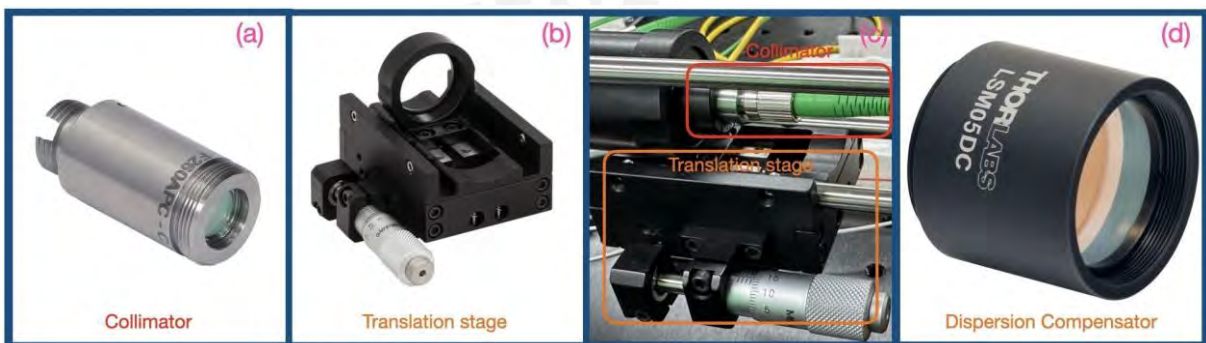


Figure 3.13: Figure (a): Collimator. Figure (b): Translation stage. Figure (c): Collimator (a) mounted on the translation stage (b). Figure (d) Dispersion compensator block. This block has a glass lens arrangement that creates the same first and second order dispersion as the scan lens LSM05 located at the sample arm - Images (a), (b) and (d) taken from "Thorlabs web site"[36].

The last component of this section is a mirror which reflects the light beam back to the collimator. A kinematic cage holds the mirror, providing tilt capability.

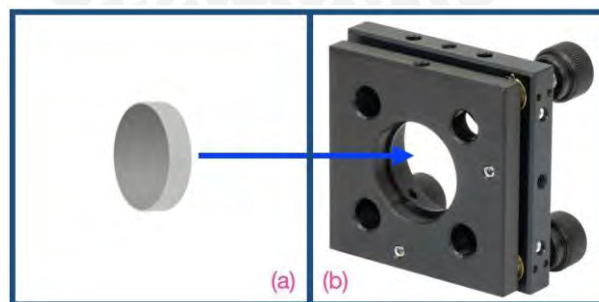


Figure 3.14: Figure (a): Reference Mirror; Thorlabs PF10-03-P01 protected silver mirror was selected to complete the reference arm. This mirror has a 25.4 mm diameter, a 22.9 mm clear aperture and a surface flatness of $\lambda/10$ at 630 nm. Figure (b): The mirror is mounted in a Thorlabs KC1/M kinematic 30 mm cage that allows the mirror to be oriented in a vertical/horizontal direction. This arrangement allows the reflected light beam to be directed to a specific direction, the focus lens. Each of its three adjusters provide up to $\pm 5^\circ$ angular displacement and up to ± 3 mm total translation displacement - Images taken from "Thorlabs web site"[36].

3.2.3 Sample Arm

The sample arm is responsible for capturing the backscattered light reflected by the sampled object. As pointed out in the previous section, to generate sample images, the interference signal, between reference and sample arms, requires the reference and sample optical paths to be the same length.

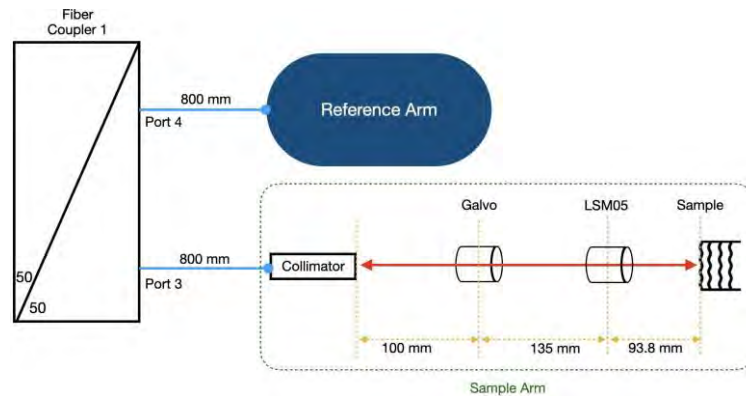


Figure 3.15: Sample Arm Length. The light beam from the laser source is divided in two paths; one is sent to the reference arm and the second one to the sample arm. Both light beams have to travel the same length in order to produce a detectable interference signal. As the fiber coupler has the same length for its 4 legs, the sample arm has to match the reference length. For this design, the sample arm length is set to 328.8 mm. This length was in the reference arm length range (130–390 mm). The scanning lens refraction index (n) was not considered in the calculation due to its short length.

The sample arm has three components, the scanning lens, the galvanometric mirror system and the collimator:

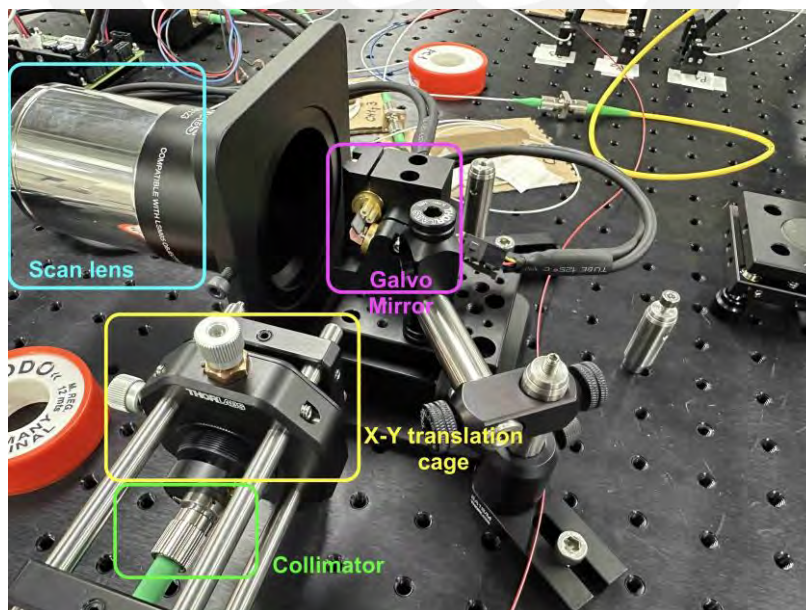


Figure 3.16: Sample Arm components: scanning lens, galvanometric mirror system and collimator mounted on an X-Y translation cage.

The scanning lens directs the light beam to the sample and captures its backscattered light. The light beam must be transported parallel to the optical axis in order to reach different sample areas.

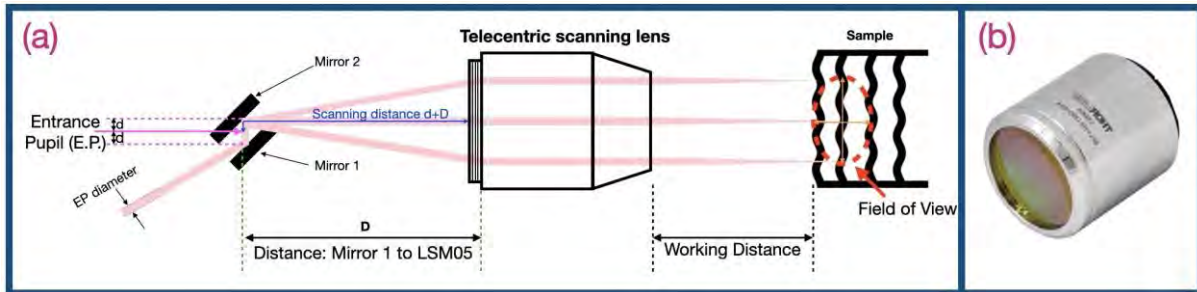


Figure 3.17: Figure (a): Telecentric properties for the scanning lens allows the light beam to reach different sample areas, keeping their back-scattered signals parallel to the optical axis. In this diagram the entrance pupil is called scanning distance and it is located between the 2 mirrors that are part of the galvanometric system. Figure (b): Telecentric scanning lens Thorlabs LSM05. This lens was selected considering that its wavelength range matches the swept laser source and that its working distance provides the necessary space to accommodate an elastography module; also its lateral field of view covers the design requirement (Table 3.1) - Image (b) taken from "Thorlabs web site" [36].

Table 3.3: Scanning lens technical specifications

Wavelength Range	1250 to 1380 nm
Working Distance	93.8 mm
Field of View (max)	28.9 mm x 28.9 mm
Scanning distance	75.5 ± 5 mm
Entrance Pupil diameter	8 mm
Optical Scan Angle	$\pm 7.5^\circ \times \pm 7.5^\circ$
Dispersion Compensator	LSM05DC

The optical scanning angle for this lens in a dual axis system is $\pm 6.2^\circ \times \pm 6.2^\circ$ (limited by diffraction) and a maximum of $\pm 7.5^\circ \times \pm 7.5^\circ$. Between this range the beam will be directed to the sample parallel to the optical axis; the scattered rays that hit the lens will also be directed to the first mirror and from this point to the collimator.

As part of the lens specifications, the manufacturer also provides a dispersion compensator block to provide the reference arm with the same optical dispersion created by the LSM05 lens.

To generate a cross-sectional image, the light beam must be moved in a single axis direction (X). To accomplish this behavior, a galvanometric mirror is controlled by applying electric voltages. To scan a sample surface, the light beam has to be moved through two axes (X and Y), using a dual mirror galvanometric system.

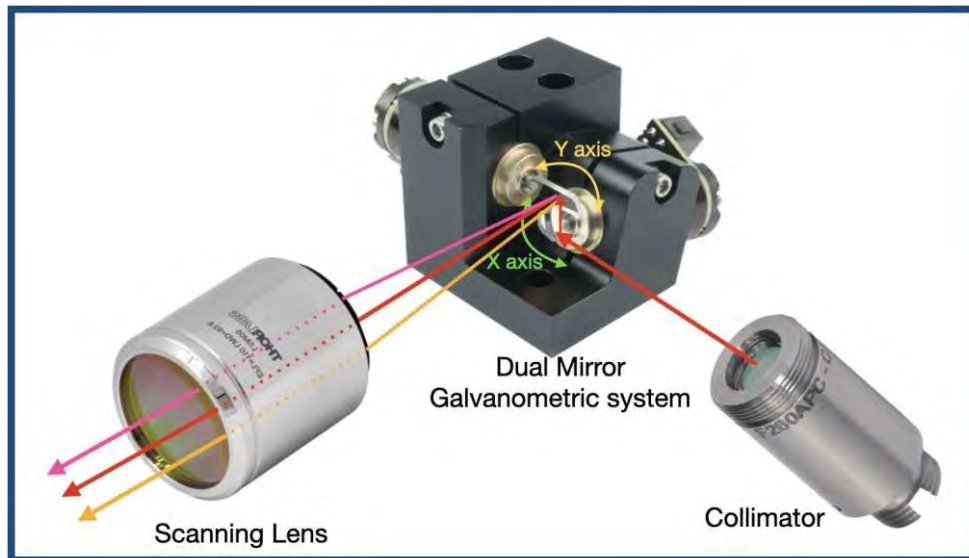


Figure 3.18: To scan superficial areas, the light beam has to be moved using specific patterns. These patterns are applied to a galvanometric system that has two mirrors; the bottom mirror controls the X axis movement while the upper mirror controls the Y axis movement. The light beams from the galvo system arrive the scanning lens forming an angle to the optical axis; the lens transports these light beams parallel to the optical axis reaching the sample in parallel to the optical axis - Images modified from "Scannermax web site" [38] and "Thorlabs web site" [36].

The Saturn1B galvanometric array system, from Scannermax, has been selected for our design. With a rotation angle of ± 27.5 degrees, it covers the lens angle range. Its high scanning speed can reach a signal bandwidth of 5 kHz. This equipment is powered by ± 24 V_{DC} with a peak consumption of 20 A. This parameter can cause high heat generation, so the power supply must be located in a well-ventilated area.

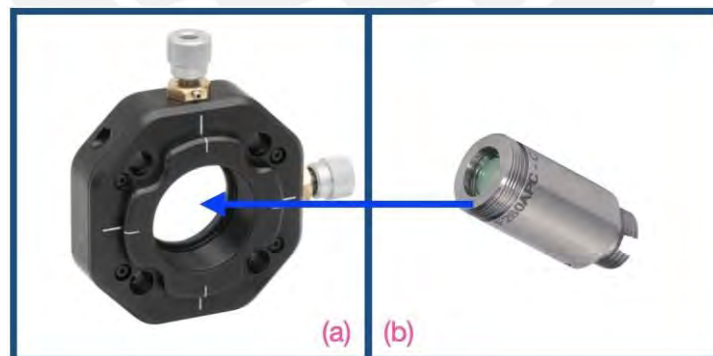


Figure 3.19: Collimator, figure (b), mounted on a translation mount Thorlabs CXY1A, figure (a). This mounting block allows to place and direct the collimator within two axes, horizontal and vertical (with ± 1 mm), to align the light beam to the dual mirror galvo system. The collimator used in this section is the same as the one used on the reference arm, figure 3.13 (a) - Images modified from "Thorlabs web site" [36]

3.2.4 Optical Path Length (OPL)

As the interference generated from the reference and sample arms is used to generate the images, both arms must have the same optical path length. Based on the reference and sample arms components, the OPL was 328.8 mm.

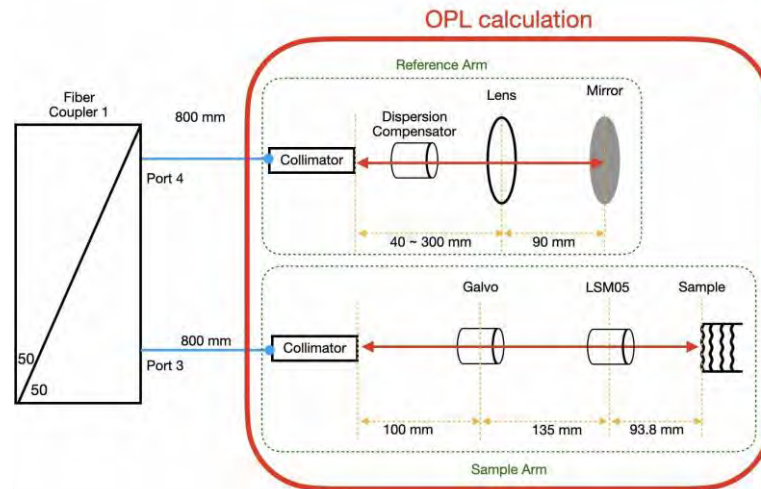


Figure 3.20: Optical Path Length Calculation. As the fiber coupler legs have the same length, we can remove them from the calculations. The Reference arm OPL can be set from 130 to 390 mm in open air. The Sample arm OPL has a fixed length of 328.8 mm in open air. As previously mentioned, the scanning lens and its dispersion compensating block have a different diffraction index (n), but this calculation was not considered due to its dimensions.

3.2.5 Acquisition and processing

During the design and implementation stage, a Rigol MSO5104 oscilloscope was used to capture the interference signals provided by the photo detector.

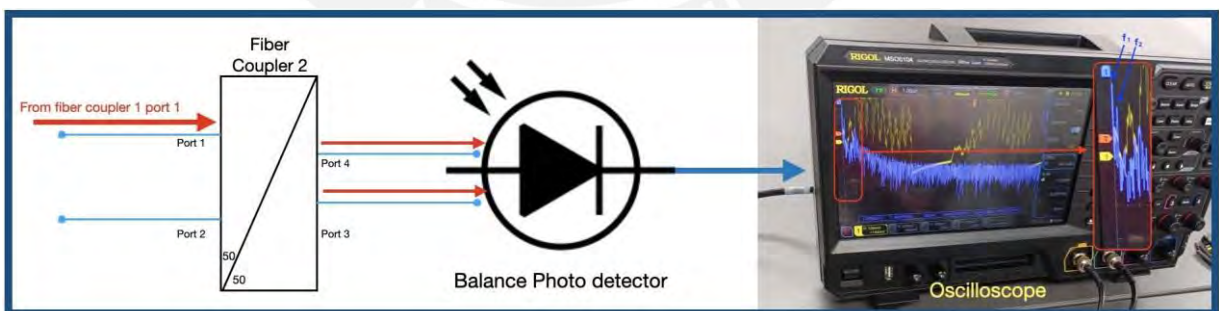


Figure 3.21: The interference signal, generated at the fiber coupler1, is sent to fiber coupler 2 to be divided in two identical signals but with half the amplitude each. These two identical signals are sent to a balanced photodetector that will subtract both signals to cancel the common mode noise. The resulting signal is converted into a electric signal that is captured by an oscilloscope. The photodetector must also use FC/APC connectors to be able to receive the fiber connections from the fiber couplers.

The selected photodetector was the Thorlabs PDB480C-AC Balanced Amplified Photodetector, optimized for 1300 nm with internal coupling fiber based on SMF-28+ and a responsivity

of 0.9 A/W @ 1550 nm. To test the design, an infrared detector card was sampled.

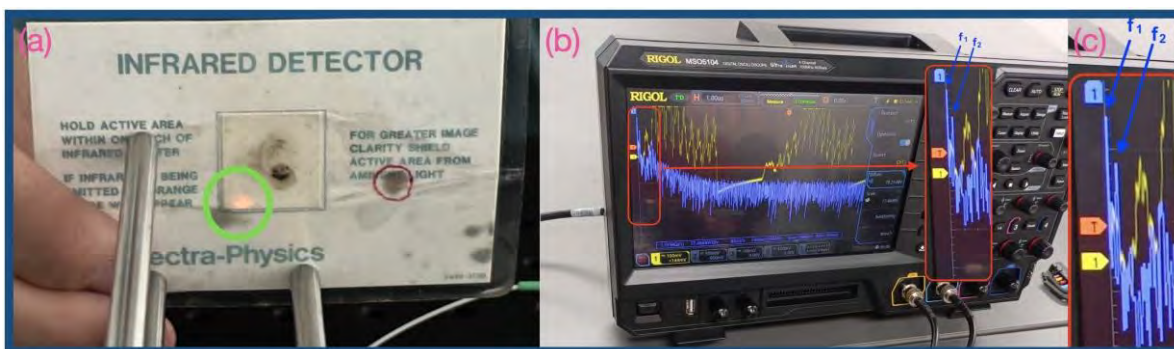


Figure 3.22: Figure (a) shows an infrared (IR) detector card, placed at the sample arm; the light beam can be spotted in the green circle. Figure (b) shows the interference signal (yellow) captured by the oscilloscope and its Fourier Transform (blue); In the red section two main frequencies can be identified. Figure (c) expands the red section; there are two main peaks that correspond to the IR card and its plastic cover.

The galvanometric mirror system was set to a fixed position in order to get axial scans at a specific point. Two peaks identified as f_1 and f_2 represent the outer layer (transparent plastic) and the IR detector section (white square). In order to translate these two frequencies into distance, the system has to be characterized using well-known patterns. At this stage, it was not necessary to generate an accurate measurement, but to identify layers with the OCT setup.

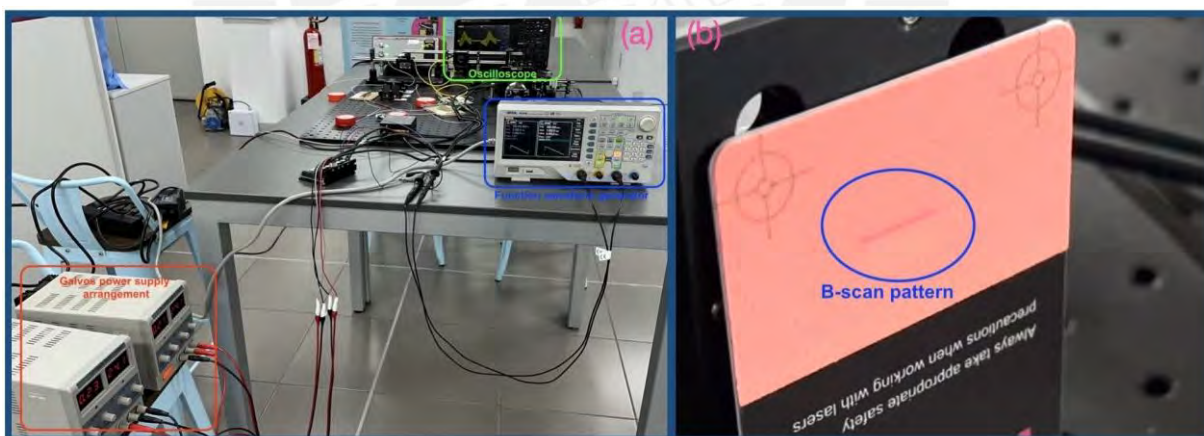


Figure 3.23: Figure (a); To start controlling the galvo system, two external power supplies were linked configured as ± 24 VDC. A 2-channel wave generator was also used to control the galvo mirrors (Rigol DG4162, arbitrary waveform generator). Figure (b) shows a linear scan pattern, known as B-scan pattern. This pattern is accomplished by controlling the bottom mirror; with a 2 V_{pp} signal with a 200 Hz frequency and a 10% symmetry sawtooth waveform. Offset and phase were set to 0 V_{DC} and 0°.

To create a 3D pattern, a second signal was applied to Y-axis; this signal was $1 V_{pp}$ with 0.4 Hz frequency and 0% symmetry waveform. The video is available at: <https://youtu.be/H8oqet198NI>. The offset and phase were also set to $0 V_{DC}$ and 0° .

3.2.6 Embedded Acquisition Devices

Once the photodetector and galvo system were tested, data acquisition and processing devices were implemented on a computer.

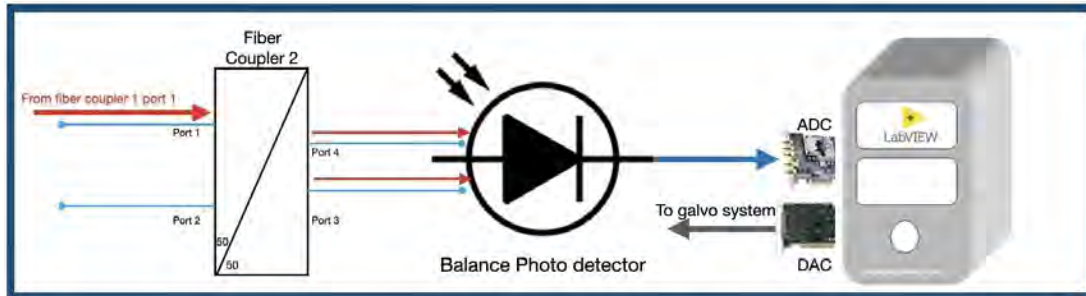


Figure 3.24: The acquisition and processing is now performed by an Analog to Digital Converter embedded card. This card is controlled by a computer application, LabVIEW, that will also control the galvo system through a second embedded card, a Digital to Analog Card.

Alazartech ATS9364 and National Instrument NI6738 cards were selected as the ADC and DAC respectively; these are PCIe (Peripheral Component Interconnect express) bus components.

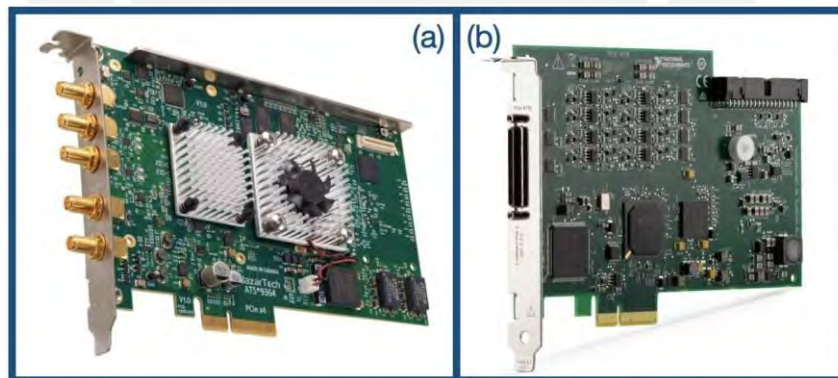


Figure 3.25: Figure (a) shows an Alazartech ATS9364, an ADC with 2 channels (12 bits resolution each). Figure (b) shows a National Instrument NI6738, a DAC to control the galvo system - Images taken from "Alazartech web site" [39] and "National Instruments web site"[40].

The ATS9364 card will acquire the interference signal through one of its two channels (with 12 bit resolution). The card is capable of acquiring up to 1 giga-samples per second. The NI6738 card will be used to control light beam by moving the galvo mirror system with one of its 32 channels (with 16 bits of signal resolution and 10 ns of timing resolution). The acquisition and galvo movements will be synchronized using the light source triggers.

3.2.7 Synchronization

To acquire and process the interference signals, the processing application (LabVIEW in this case) has to know when the light source starts the swept period, through the ATS9364 card, in order to control the start scan pattern at the galvo system, using the NI6738 card. Although the ATS9364 and the NI6738 cards can provide a synchronization signal, the master reference clock will be provided by the light source.

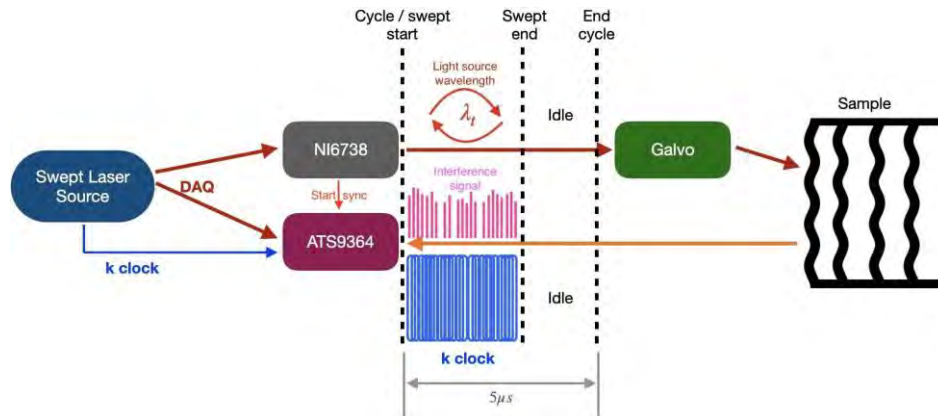


Figure 3.26: Synchronization scheme. The light source provides the reference clock through the DAQ trigger; at the same time it provides a k-clock signal that will be used as reference to process the signal. The NI6738 starts to control the galvo mirrors and sends an indication to ATS9364.

The following diagram shows the synchronization sequence. The galvo X – Y control signals correspond to a crosshair scan pattern.

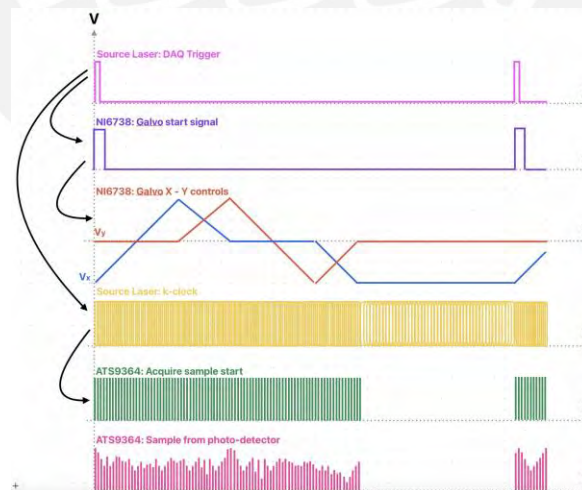


Figure 3.27: OCT Synchronization Signals. DAQ trigger signal is the system reference (first pattern, pink signal). NI6738 generates a galvo start signal, also known as B-trigger, taking DAQ as reference (second pattern, purple signal). NI6738 starts controlling X-Y galvo mirrors (third pattern, red and blue). K-clock signal start begins at the same time as DAQ trigger (fourth pattern, yellow signal). ATS9364 marks the sample gathering from k-clock (fifth pattern, green signal). The interference spectrum is acquired at the ATS9364 (sixth pattern, vermilion signal).

The connection between the system components are shown in the following figure:

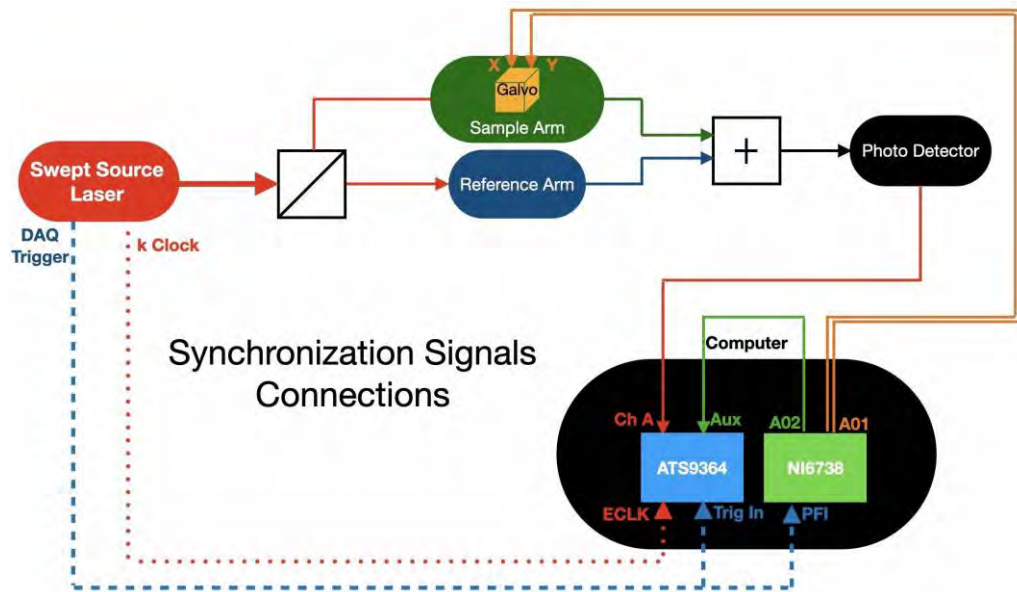


Figure 3.28: Synchronization signals distribution. By using the k-clock signal from the laser source, the k-linearization process is not required. DAQ trigger is used by ATS9364 and NI6738 cards to elaborate control and acquisition signals.

To control and acquire all of these signals, a LabView application provided by Professor F. Zvietkovick was used. This application controlled the data acquisition from the ATS9364 card and controlled the galvo mirror system through the NI6738 card.

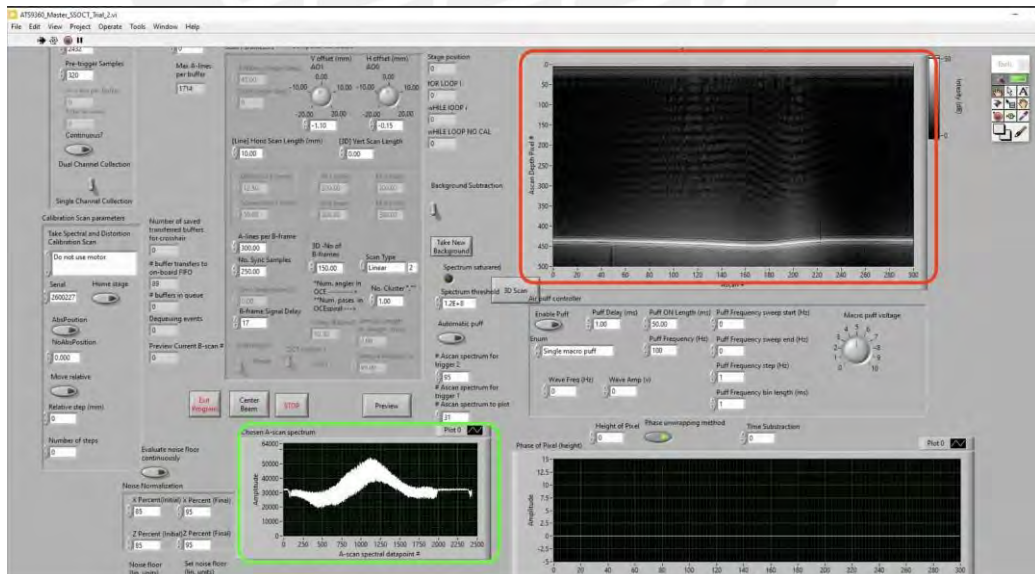


Figure 3.29: LabView App Interface. Green section, shows the captured interference spectrum. On the same figure, red section, the the data is processed to show the sample image (a mirror).

The optic circulator was replaced by the Thorlabs IO-H-1310APC, Fiber Isolator. This element directs the light source from the input port to the output port. The light incoming from the output port will not be directed to the input.

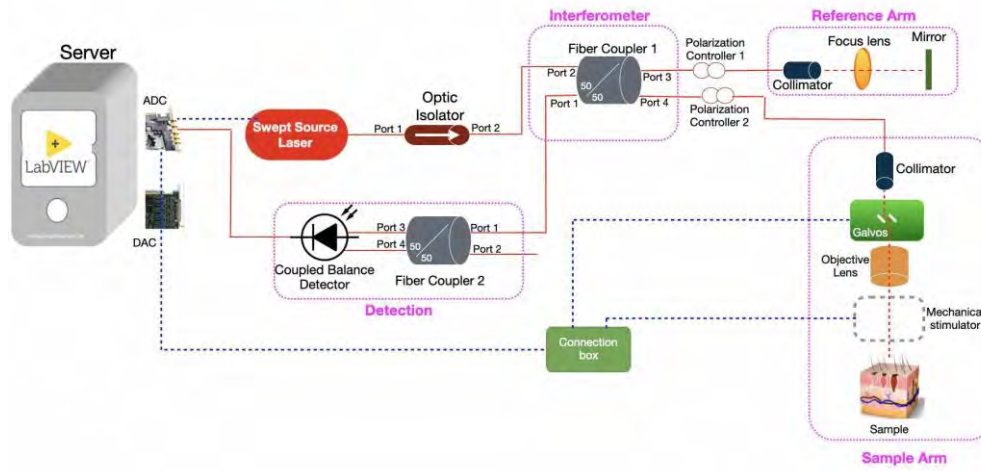


Figure 3.30: OCT design updated with the acquisition and control cards in a computer with a LabVIEW application.

With this setup, the first scans were performed. A mirror, a glass (coverglass) and a multi-layer glass arrangement (slide and coverslide) were used.

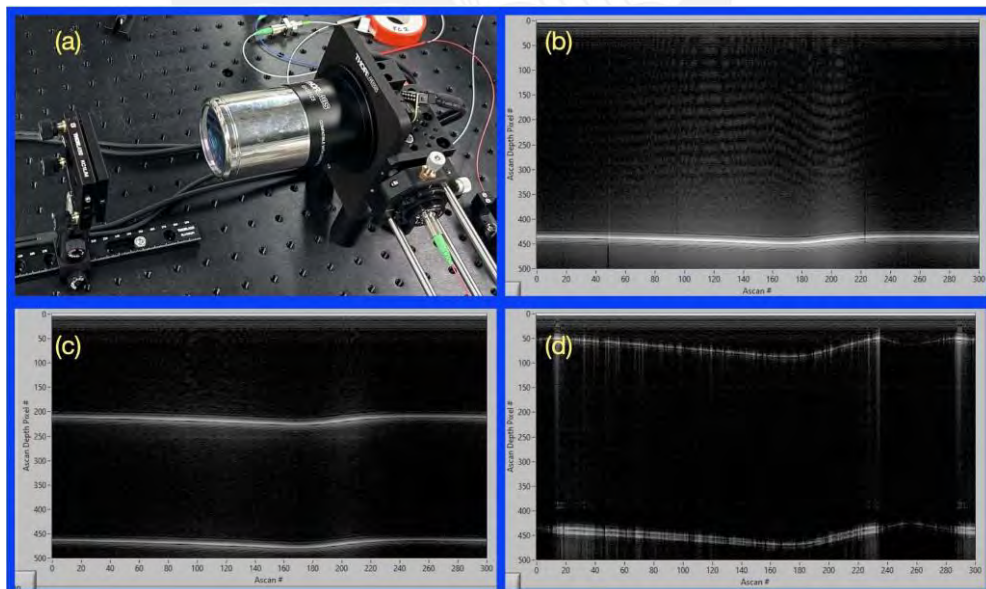


Figure 3.31: Figure (a): A sample (mirror/glass/plastic) placed at the scanning (focal) point. Figure (b): the LabVIEW application generates a single line (the mirror surface) that represents every scanned point in the sample because every one of them has the same intensity. 300 sample points were scanned in a 10 mm length. Figure (c) shows the scanned image obtained from a coverslide, a glass surface. Figure (d) shows the scanned image obtained from a plastic ruler sample. The image from the plastic sample shows imperfections in its surfaces. All the generated images present curvatures even though the scanned objects have flat surfaces; this deformation was caused by the processing application.

The last sampled object was an infrared detector card. The image obtained was blurry and very faint; it did not provide a recognizable structure.

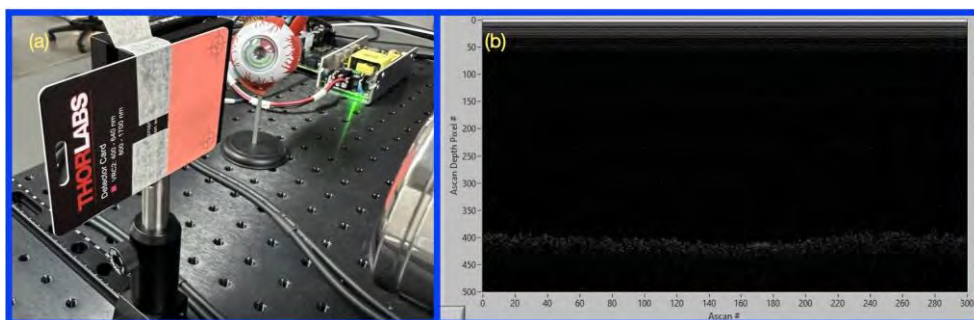


Figure 3.32: Figure (a) shows an infrared detector card at the scanning point. Figure (b) shows the image obtained from the IR card scan. This scan does not generate a usable image.

3.2.8 OCT Design Results

- The system is generating well-defined images for transparent samples such as glasses and plastic.
- For opaque objects, the images can barely show ghostly figures.
- Flat surfaces have some distortion.

The distortion on flat surfaces is related to the LabVIEW application that was designed for different acquisition devices. The synchronization triggers were not being correctly treated, causing aberration of the image. The application was reconfigured with the proper drivers and the images were correctly generated.

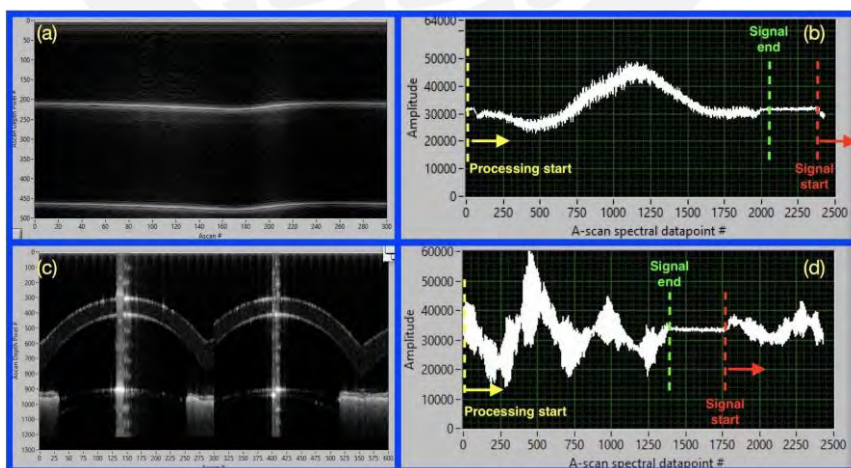


Figure 3.33: Figure (a) shows a generated image from a scanned glass. Figure (b) shows figure (a) interference signal analyzed by the LabVIEW application. Figure (c) shows a generated image from a scanned plastic eye using a crosshair pattern (horizontal and vertical). Figure (d) shows figure (c) interference signal. In both A-scan spectral datapoints analysis, the interference signal is not synchronized with the processing task.

Figures 3.33 (b) and (d) show that the data processing task starts when the interference signal has already started. Figure 3.33 (b) shows a small slide in the interference spectrum; in Figure 3.33 (d) the slide is significantly longer.

With this design, transparent objects generate well-defined images, but the system must be capable of scanning opaque objects, penetrating their external layers, and generating useful images. Ghostly images are caused by the lack of light intensity in the signal coming from the sample object. This issue was caused by an inefficient optic design.

3.3 OCT Design Adjustment

Based on the results obtained with the original design, a new interferometry arrangement was implemented, a Mach-Zehnder configuration, with three fiber couplers and one fiber optic circulator, a Thorlabs CIR-1310-50-APC.

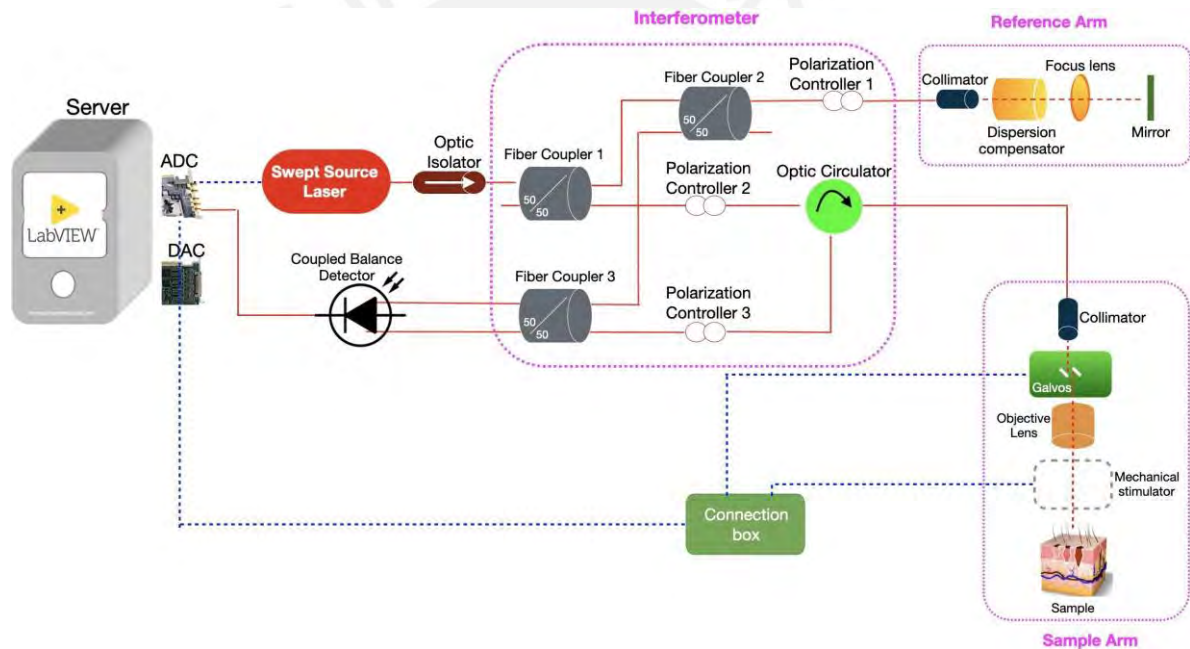


Figure 3.34: OCT Design adjustment. The interferometer configuration changed from a Michelson configuration for a Mac-Zehnder one using an additional fiber coupler and an optic circulator.

In both interferometer configurations, part of the light intensity is reflected to the light source; this is the reason why an optic isolator was included. Without an isolator, the laser device inhibits its operation.

In this modified design, the sample and reference arms were not modified. As mentioned, the interferometer was modified. With the original design, the sample received 50% of the source emitted optical intensity. Then the scattered light from the sample returns to fiber coupler 1 and is sent to the left ports; 25% of the original intensity (if a mirror is used as the sample) reached fiber coupler 2.

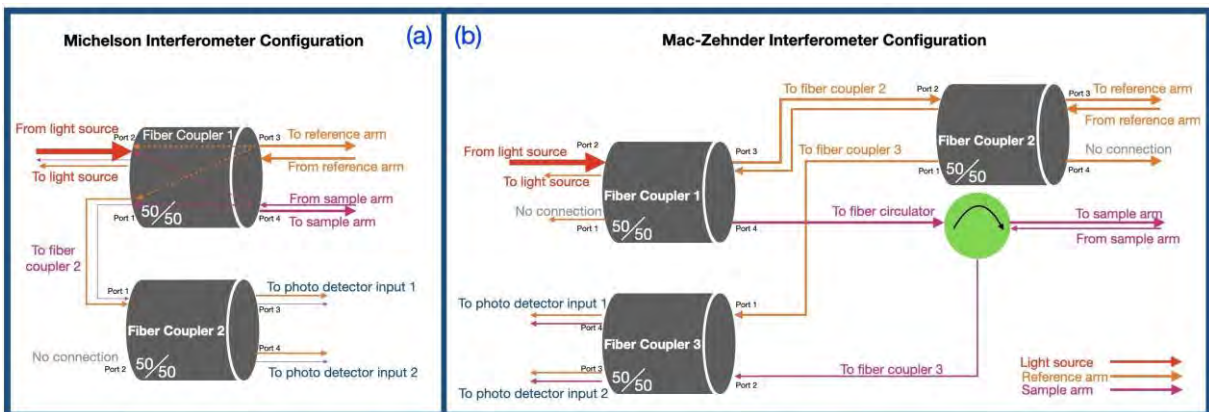


Figure 3.35: Figure (a) shows the Michelson interferometer configuration used in the original design; fiber coupler 1 port 2 is receiving signals reflected from reference and sample arms. Figure (b) shows the Mac-Zehnder interferometer configuration implemented in the system modification; there is no signal from sample arm on fiber coupler 1 port2, all the reflected intensity is sent to fiber coupler 3.

With the Mac-Zehnder interferometer, the sample still receives 50% of the emitted optical intensity, but the scattered light from the samples is carried straight to the final step, fiber coupler 3, with its whole intensity (50% if a mirror is used), twice the intensity as the Michelson interferometer configuration.

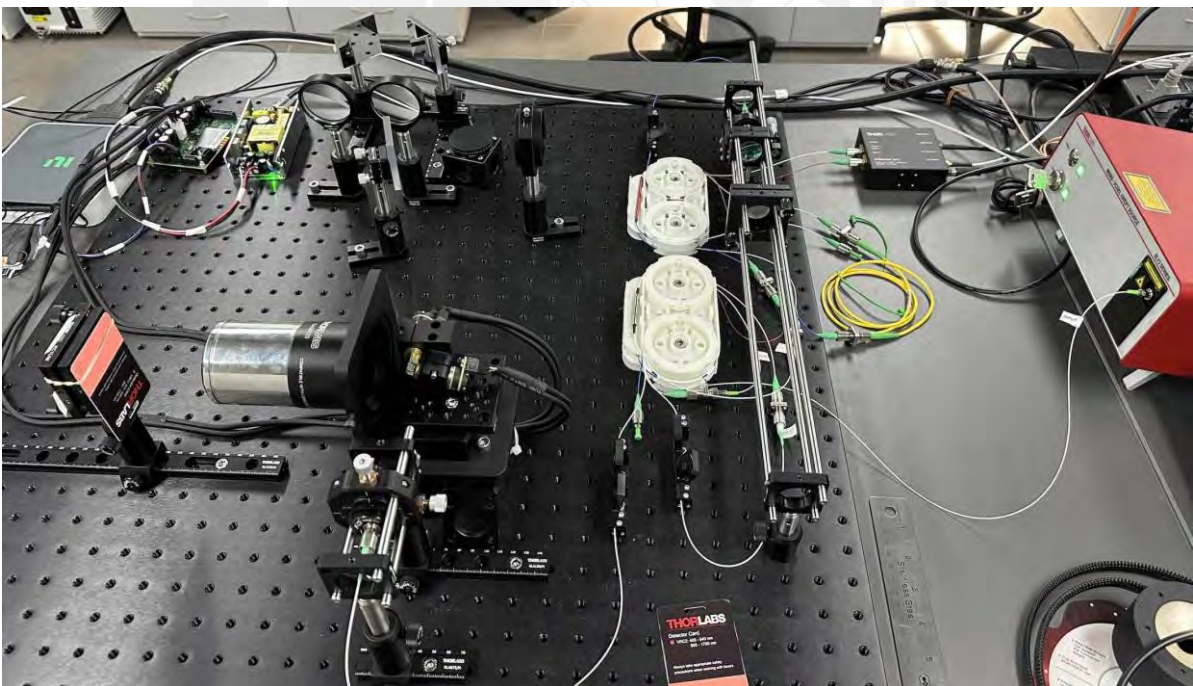


Figure 3.36: OCT system with a Mac-Zehnder interferometer configuration. The additional fiber coupler has two purposes; to reduce the intensity reflected from the reference arm and to match the optical path length (OPL). OPL is the length the light travels on the reference arm and at the sample arm. Both have to be almost the same length in order to be able to generate images.

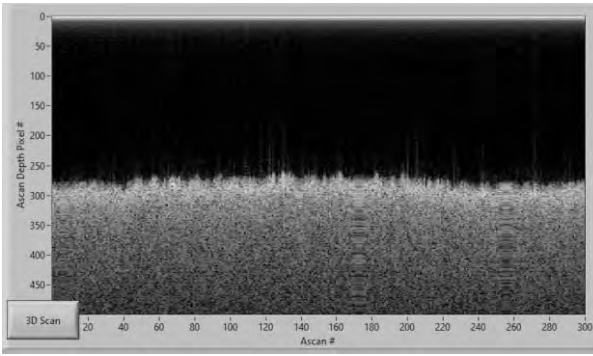


Figure 3.37: IR Card image generated with the modified OCT system. This image has better intensity and can be analyzed.

The same IR detector card was used to get images using the new design. The system was able to generate this well-defined image. Compared with figure 3.32 (a), figure 3.37 shows more light intensity, which is generated by having twice the optical power at the Dual Balanced Photodetector.

The image also shows a depth that, in this case, is about 200 samples. To translate this measure into a metric value, the system must be characterized.

A glass was scanned again to compare the resulted image, as well as a plastic model eye.

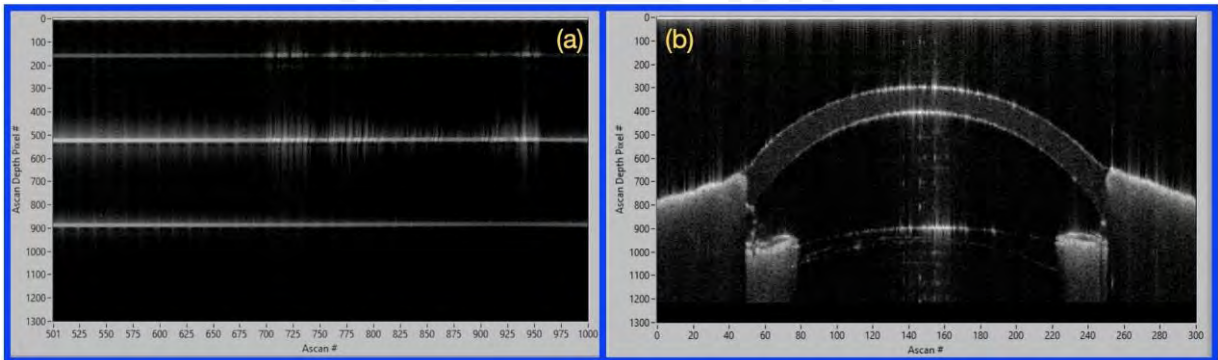


Figure 3.38: Figure (a) shows a glass object scanned with a crosshair pattern; the horizontal and vertical images are perfectly aligned. Figure (b) shows an image from a plastic model eye, scanned with a linear (horizontal) pattern.

3.3.1 Modified Design Results

- The system generates well-defined images for transparent and opaque samples.
- LabView application was corrected, so flat surfaces do not present distortion.
- A component list was generated, and it is included in the appendix section.

After the modifications were applied to the design of the system, the system was able to generate clear and well-defined images. The next step is to characterize the system.

Chapter IV

System Characterization and first images

Before the system can go into service, it must be properly aligned (optically) and characterized. The first procedure involves placing all optical elements in the best position and direction; the second procedure finds its parameters using well-known elements and processes.

4.1 Alignment

The optical components of the system can be classified into fiber optic and glass elements. Fiber-optical elements do not require alignment procedures because they have standard endings/connectors. In this system all fiber endings/connectors are FC/APC (Fiber-optic Connector / Angled Physical Contact); this type of connector has an end polished at an 8° which provides a very low back reflection. Lenses and mirrors are grouped as glass elements. These components usually have a focal point that must be met in order to achieve the results the manufacturer offers. In addition, light beams have to cross these points and maintain their altitude and distance parameters. The alignment procedure ensures that the light beam maintains its distance and direction as specified by the manufacturer.

4.1.1 Reference Arm Alignment

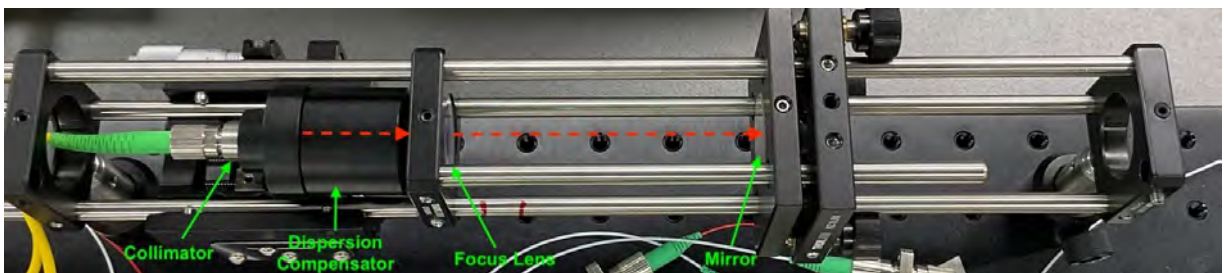


Figure 4.1: Reference arm components. The cubic stage (figure 3.11) was removed due to the OPL reduction on the second design. The dispersion compensating block was mounted in the translation stage, figure 3.13(b) forward face, back to back with the collimator. The focus lens, figure 3.12, is closed to the dispersion compensating block. As the laser beam has a 1300 nm wavelength, invisible for the human eye, infrared detector cards (IRC) were used to trace the beam.

The alignment procedure for the reference arm only requires the use of the IRC tracing the light beam from the collimator to the focus lens and from it to the mirror and the reverse trajectory. The reflected beam, from the mirror, was adjusted to point to the lens using the mirror holder tilt adjusters, figure 3.14 (b).

4.1.2 Sample Arm Alignment



Figure 4.2: Sample arm scanning Array

Figure 4.2 shows the scanning array on the Sample arm. It has two main components: the LSM05 scanning lens, Figure 3.17 (b) and the galvanometric mirror system (Figure 3.18).

To align this section, the galvo has to reflect the light beam on its superior mirror at the center point of the scanning lens.

The first step in this process was to remove the scanning lens; the light beam was traced using infrared detector cards.

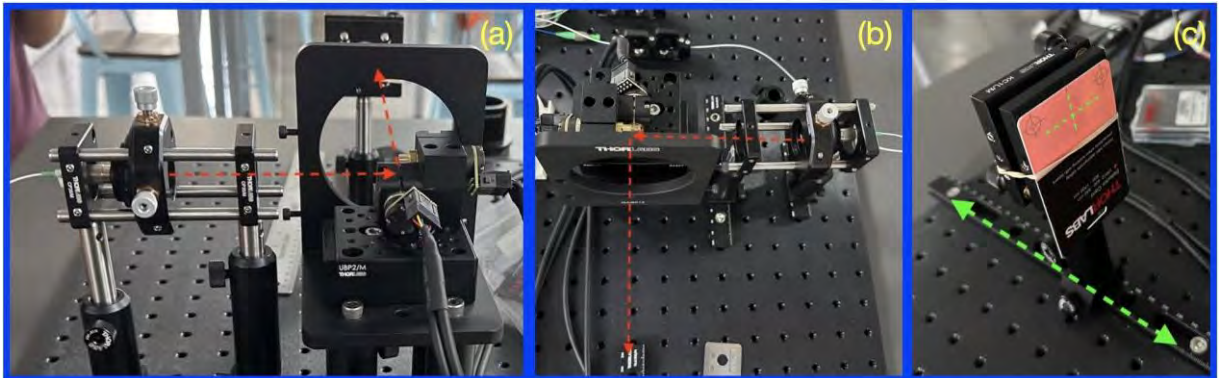


Figure 4.3: Sample arm alignment procedure. Figures (a) and (b) shows the route used by the laser beam through the mounting supports; the galvo system is mounted on top of two blocks, Thorlabs UBP2/M and BA2S7. Figure (c) shows the IR card, mounted on a metric rail, tracing the light beam elevation and lateral deviation. As the IR card "turns off" if the light beam remains on the same spot, two moving patterns were used to trace the center. An horizontal line pattern was used to verify the altitude remained the same. A vertical line pattern was used to verify the optical axis was maintain.

Once the optical alignment was completed, the lens was replaced in the mounting bracket. Then a mirror was installed instead of the IR card at the working distance of the scanning lens (93.8 mm).

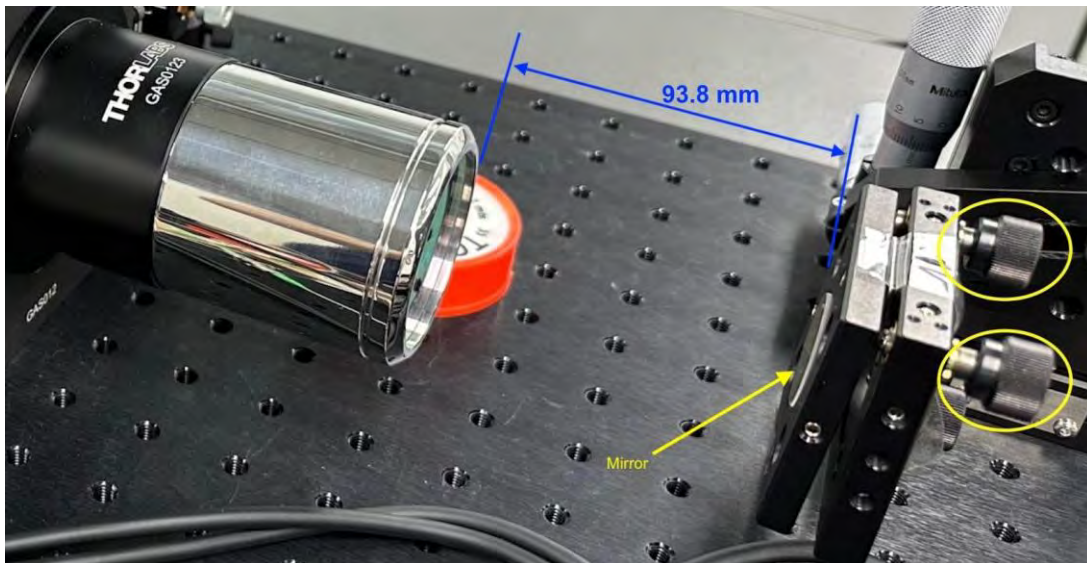


Figure 4.4: The mirror mounted as a sample has the same characteristics as the one located at the reference arm. The mirror mounting bracket is, also, the same type as the one used at the reference arm; it has three adjusters (yellow circles in figure 4.4) that allows the mirror to displace the reflected light beam $\pm 5^\circ$.

4.1.3 Working Distance

Once the previous steps have been completed, a verification of the lens working distance was performed. According to the manufacturer, this value is defined as the distance between the LSM05 lens and the sample (Figure 4.4) and is set to 93.8 mm.

The setup used was the same as that shown in figure 4.3 (c). The IR card is mounted on a moving support on a metric rail. The procedure starts by locating the IR card over the manufacturer-provided working distance. Using the LabView application to generate the image, the IR card is moved towards the lens and then away from the lens. When comparing the images generated by the IR card scans, the best ones by definition were generated when the IR card was placed at 83 mm. This value was set as the default for all new scanning procedures.

4.2 OCT Characterization

The characterization process is intended to find the system images parameters such as axial resolution, sensitivity (roll-off), among others. For this procedure, objects with well-known dimensions must be used, such as hex keys.

In each characterization step, multiple images will be generated, and their values, measured in pixels, will be compared with the dimensions of the object.

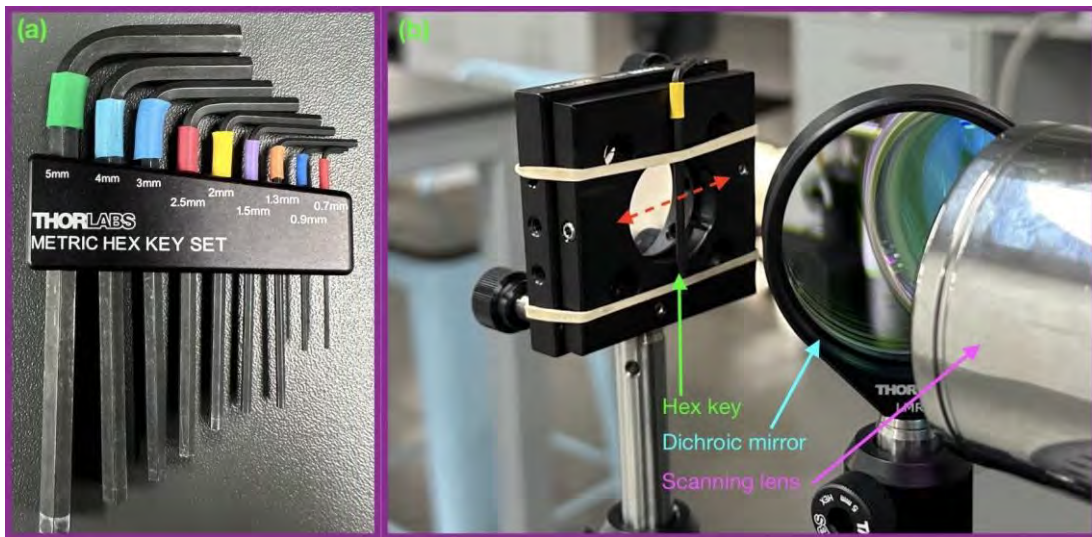


Figure 4.5: Figure (a): A metric hex key set used for the characterization procedure. Figure (b): The 2 mm hex key placed vertically for the horizontal characterization procedure. A dichroic mirror was placed between the hex key and the scanning lens; this mirror is transparent for the light beam wavelength used ($\lambda = 1300\text{nm}$).

A set of metric hex keys, also known as Allen wrenches, was used for the procedure. Figure 4.5 (b), the 2mm hex key was placed vertically to characterize the horizontal resolution. The hex keys were positioned facing the lens. The dichroic mirror is used for a patient sight alignment, and it is practically transparent for the infrared light beam used in the system.

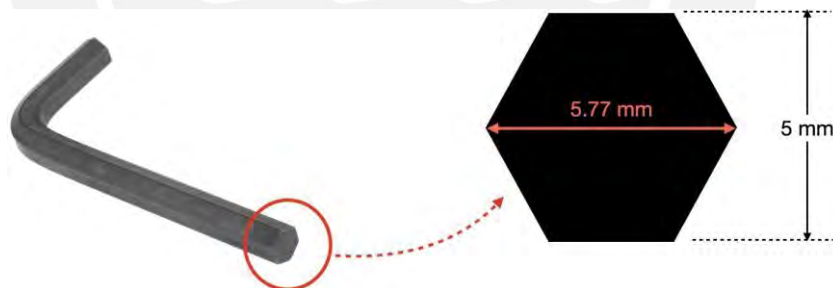


Figure 4.6: Hex Dimensions. In this case a 5 mm hex key was used to calculate the largest to the shortest diagonal relation (1.154). All the keys were used except the smallest one, because it was not possible to place it properly

4.2.1 Lateral Characterization

This procedure will determine the relationship between the pixels in the images generated by the system and the dimensions of the scanned sample (hex keys). Several hex keys with different dimensions were scanned facing the longest surface to the scanning lens. Starting with the 5mm hex key, placed in the same position as in Figure 4.5, the system generated the following image (Figure 4.7). The scan length was set to 15 mm with 300 samples (A-scans).

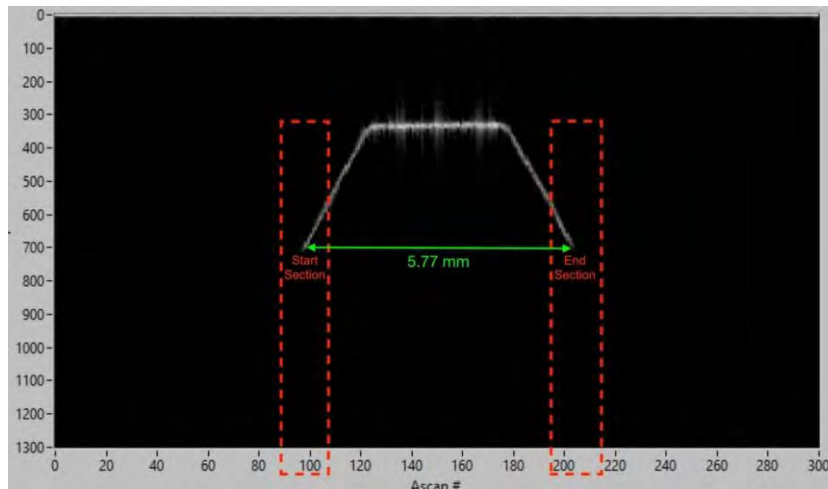


Figure 4.7: 5 mm hex key scanned image. Start and end sections are enclosed in red sections.

The red sections were zoomed in to get better accuracy in the measurements.

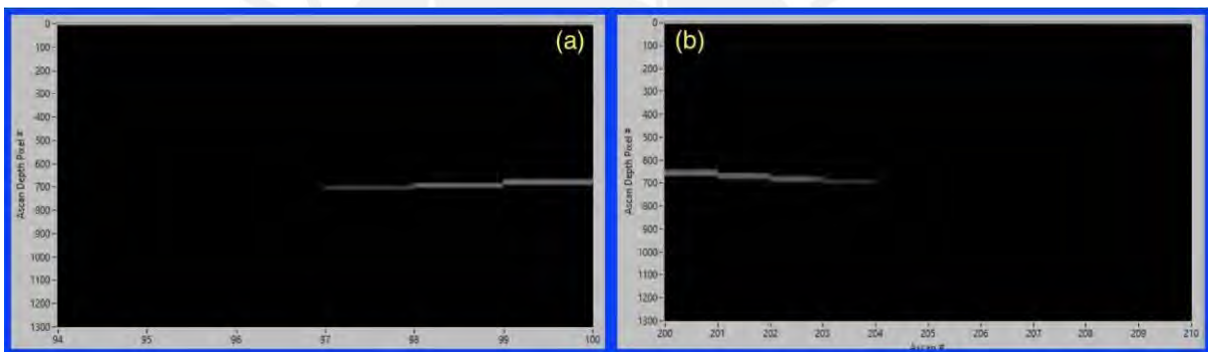


Figure 4.8: Zoomed in start and end pixels. Figure (a): the image starts on pixel 98 and ends on pixel 204, figure (b); its length, in pixels, is 106. Then 106 pixels are equivalent to 5.77mm or 1 pix = 54.43 μm (on a 15 mm section scan). The procedure was repeated with 15 mm, 12.5 mm, 10 mm, 7.5 mm, 5 mm and 2.5 mm scan ranges. The number of A-scans (pixels) per section scan was 300.

These measurements were repeated with vertically oriented hex keys, to find horizontal values (Figure 4.7), and then horizontally oriented hex keys to find vertical values. The values obtained were practically the same. For these measurements, the number of A-scans (pixels) per section scan was 500.

Table 4.1: Lateral Characterization Measures

Scanning range (mm)	Hex M	Start Px	End Px	Length (Px)	Length (mm)
15	5	89	266	177	5.773502692
12.5	5	59	272	213	5.773502692
10	5	110	376	266	5.773502692
7.5	5	67	422	355	5.773502692
5	5	Off scale			

2.5	5	Off scale			
1	5	Off scale			
15	4	171	312	141	4.618802154
12.5	4	157	327	170	4.618802154
10	4	137	349	212	4.618802154
7.5	4	104	387	283	4.618802154
5	4	37	461	424	4.618802154
2.5	4	Off scale			
1	4	Off scale			
15	3	188	294	106	3.464101615
12.5	3	178	304	126	3.464101615
10	3	163	321	158	3.464101615
7.5	3	138	349	211	3.464101615
5	3	87	404	317	3.464101615
2.5	3	Off scale			
1	3	Off scale			
15	2.5	193	281	88	2.886751346
12.5	2.5	184	289	105	2.886751346
10	2.5	170	302	132	2.886751346
7.5	2.5	148	323	175	2.886751346
5	2.5	101	365	264	2.886751346
2.5	2.5	Off scale			
1	2.5	Off scale			
12.5	2	209	292	83	2.309401077
10	2	201	306	105	2.309401077
7.5	2	189	328	139	2.309401077
5	2	163	373	210	2.309401077
2.5	2	89	495	406	2.309401077
1	2	Off scale			
15	1.5	213	265	52	1.732050808
12.5	1.5	207	270	63	1.732050808
10	1.5	199	278	79	1.732050808
7.5	1.5	185	291	106	1.732050808
5	1.5	159	317	158	1.732050808
2.5	1.5	80	398	318	1.732050808
1	1.5	Off scale			
15	1.3	224	269	45	1.5011107
12.5	1.3	221	275	54	1.5011107
10	1.3	216	283	67	1.5011107
7.5	1.3	209	298	89	1.5011107
5	1.3	193	328	135	1.5011107
2.5	1.3	148	418	270	1.5011107

1	1.3	Off scale			
15	0.9	221	252	31	1.039230485
12.5	0.9	217	255	38	1.039230485
10	0.9	211	259	48	1.039230485
7.5	0.9	202	265	63	1.039230485
5	0.9	183	279	96	1.039230485
2.5	0.9	129	321	192	1.039230485
1	0.9	Off scale			

The values of table 4.1 are taken to create a new table with the mean and standard deviation values.

Table 4.2: Length resolution

Scanning Range (mm)	px / μm (Average)	μm / px (Average)	Std. Dev. (%)
15.0	0.030	33.07	1.16%
12.5	0.036	27.47	0.95%
10.0	0.046	21.91	1.06%
7.5	0.061	16.48	1.18%
5.0	0.091	10.95	0.84%
2.5	0.181	5.53	2.25%

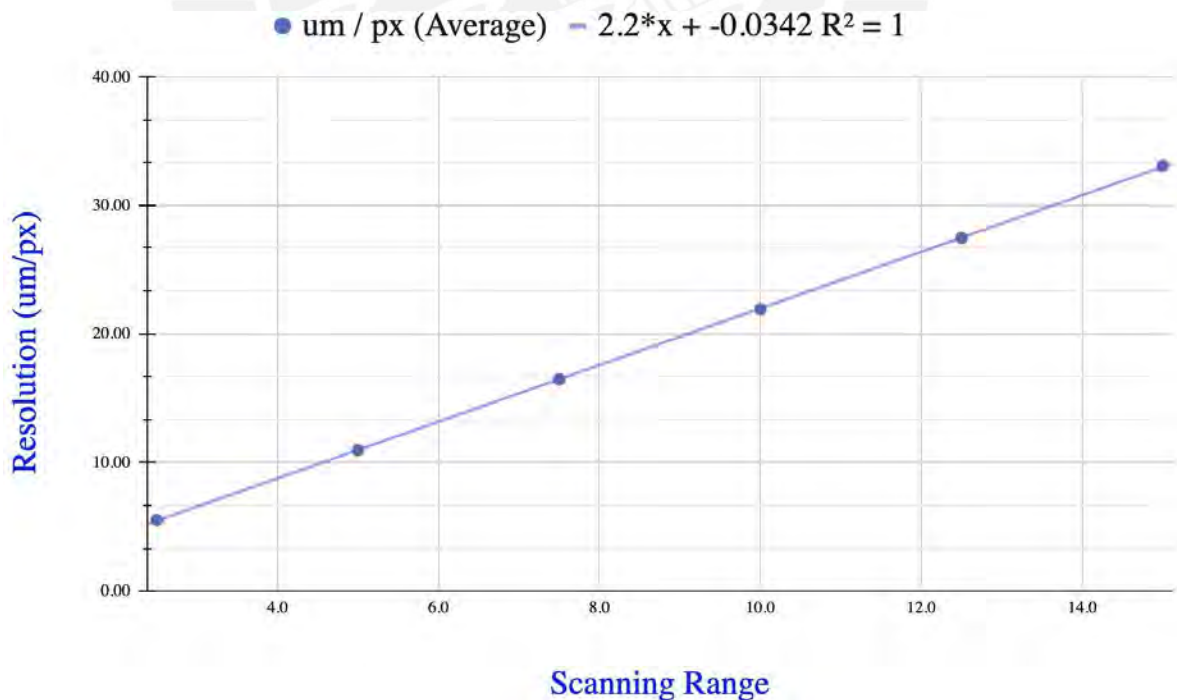


Figure 4.9: Horizontal resolution chart. From table 4.2, the best resolution belongs to sampled lengths of 2.5 mm; a 5.53 $\mu\text{m}/\text{px}$. The scattered plot shows the correlation between resolution ($\mu\text{m}/\text{px}$) and scanning range.

4.2.2 Depth Characterization

As in the previous section, this procedure determines the relationship between the pixels in the images generated and the dimensions of the scanned sample but in the axial dimension. For this procedure, a mirror is used as a sample object, located at the working distance obtained during the alignment of the system (Subsection 4.1.3).

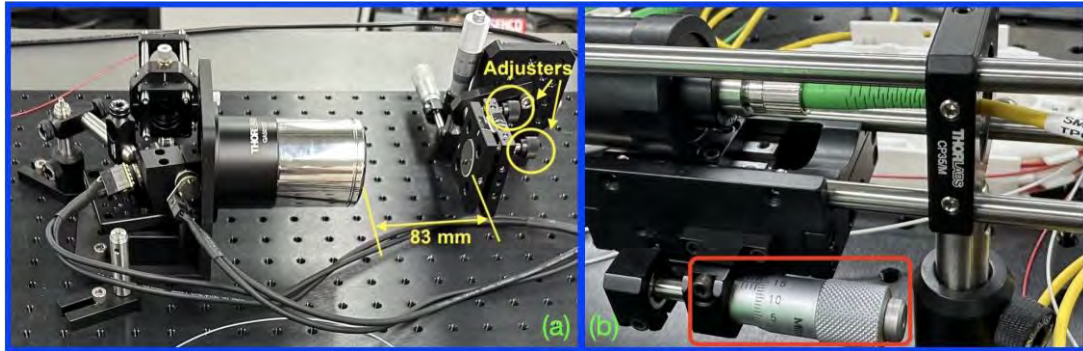


Figure 4.10: Depth Characterization procedure. Figure (a) shows the mirror in this procedure; the scattering overloads the signal, causing a blurred and thick image. Using the adjusters (yellow circles) located on the mirror mounting bracket, the mirror is slowly tilted until a clear and well defined signal is visible in the image. Figure (b) shows the reference micrometer used to slide away the reference collimator. A full 360° turn slides the collimator 500 μm .

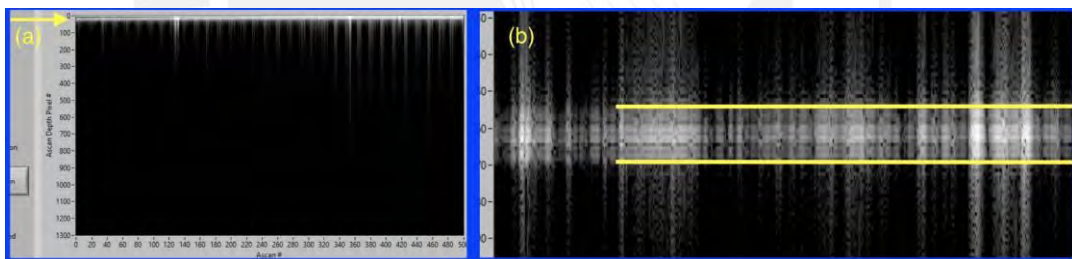


Figure 4.11: As mirror is used as sample, the resultant image is a line that represents a single frequency. Figure (a): the start point selected was the closest to the OPL, without distorting the signal. Figure (b): the line was zoomed in to measure its thickness.

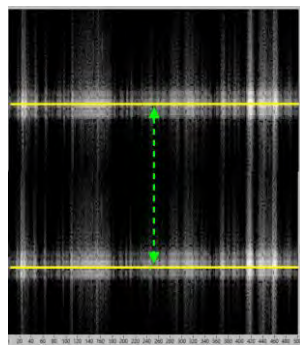


Figure 4.12: Image from the micrometer full rotation (500 μm)

Using a full rotation of the micrometer, the reference arm is shifted 500 μm away. The signal center (the mean value between the starting and ending pixels) is used to measure the pixel displacement.

The procedure is repeated until the end of the micrometer or the system limit is reached, as shown in figure 4.13 (b). In this case, the system limit was reached, as shown in figure 4.13 (a).

When the maximum depth is reached, the image will display no light information, represented by a black section.

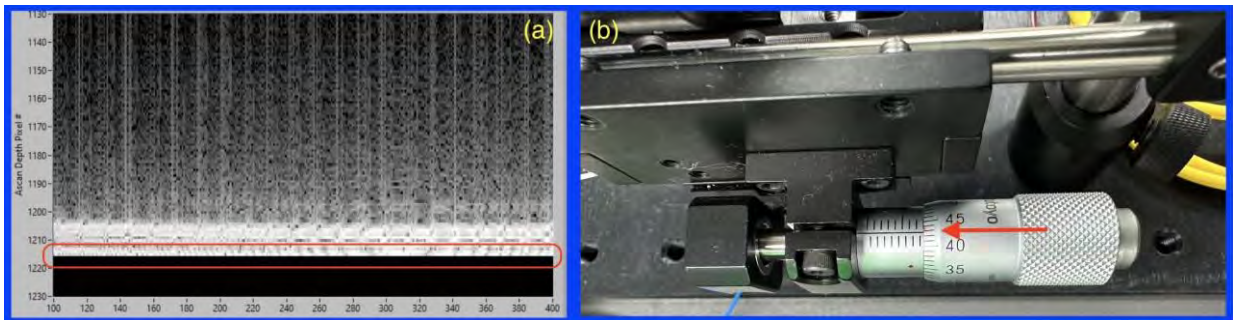


Figure 4.13: Figure (a): System depth limit. Figure (b): The micrometer used to slide the reference collimator.

The measurements obtained are included in the following table.

Table 4.3: Depth Characterization

Distance (μm)	Start Px	End Px	Length (Px)	Center	Distance (Px)
0	0	15	15	7.5	0
500	75	90	15	82.5	75.0
500	150	165	15	157.5	75.0
500	226	242	16	234.0	76.5
500	303	318	15	310.5	76.5
500	378	394	16	386.0	75.5
500	453	468	15	460.5	74.5
500	530	546	16	538.0	77.5
500	605	620	15	612.5	74.5
500	676	693	17	684.5	72.0
500	751	767	16	759.0	74.5
500	828	842	14	835.0	76.0
500	904	918	14	911.0	76.0
500	980	995	15	987.5	76.5
500	1056	1072	16	1064.0	76.5
500	1133	1148	15	1140.5	76.5

From table 4.3:
 Average length in pixels = 15.3125
 Average distance in pixels = 75.5
 Standard deviation = 1.3 (1.72%)

Table 4.4: Depth Resolution in air

$\frac{\mu\text{m}}{\text{px}}$	$\frac{\text{px}}{\mu\text{m}}$
6.16	0.1511

4.2.3 Axial Depth Adjustment

To calculate the Axial Resolution we use a well-known object, slides, to measure its thickness and compare the measures from the images with manual ones taken with a caliper.

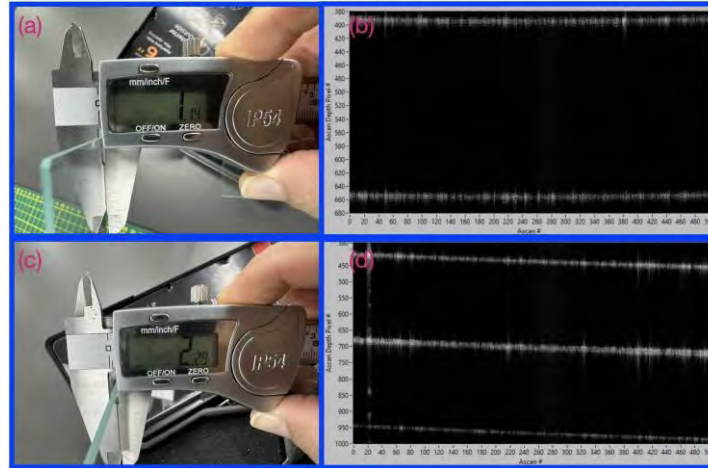


Figure 4.14: Figure (a) shows a slide measured with a caliper, providing a measurement of 1.14 mm deep. Figure (b) shows the scanned image from the same object; the surfaces are separated by 260 pixel that, using the value obtained in the procedure Depth Characterization 4.2.2, can be translated to 1.068 mm for glass with a refractive index (n) of 1.5. Figure (c) shows two adjacent slides measured with the caliper, with a 2.29 mm deep measurement. Figure (d) shows the scanned image that provides a 2.177 mm measurement.

According to figure 4.14, a 4.93% correction has to be applied to the $6.16 \mu\text{m}/\text{px}$ value. The new depth resolution value is: $6.46 \mu\text{m}/\text{px}$.

4.2.4 Lateral Resolution

The lateral resolution procedure finds the minimum detail of the system (resolution) that can be observed in the lateral areas. A 1951 USAF resolution target has been used to test the system's lateral resolution. The lateral resolution found was $34.97 \mu\text{m}$.

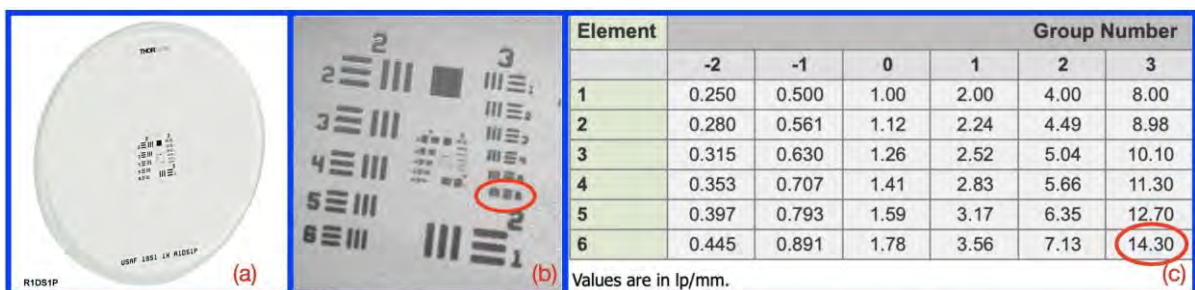


Figure 4.15: Figure (a): 1951USAf Resolution Target by Thorlabs. The resolution is determined by the smallest group of recognizable parallel lines. Figure (b) shows the resolution target image scanned by the system; the smallest group of recognizable lines belongs to group 3, element 6. Figure (c) provides a 14.30 line pairs per millimeter (lp/mm). This means that the minimum line width resolution is $35 \mu\text{m}$. - Figure (b) was generated with a MatLab script created by L.Barreto from PUCP GiBio [41]

4.2.5 Axial Resolution

The axial resolution procedure finds the minimum detail of the system (resolution) that can be observed on samples in the depth axis. From equation 3.1, the Axial Resolution (ΔZ) is defined by the light source according to:

$$\Delta Z = 2\ln(2) \frac{\lambda_0^2}{\pi\Delta\lambda}$$

The light source has a 100 nm of bandwidth and a central wavelength of 1,300 nm:

$$\Delta Z = 2\ln(2) \frac{(1300\text{nm})^2}{\pi 100\text{nm}} = 7.4574\mu\text{m}$$

For the practical measurement, the procedure is similar to the Subsection 4.2.2; a mirror is used as a sample. In this case, only one measurement is used, the closest one to the OPL with the best definition. An oscilloscope captures the interference signal; the captured data is analyzed to find the Full Width at Half Maximum value (FWHM). The FWHM represents the length of coherence of the light beam (Figure 2.8) and is the minimum length that can be measured (resolution) on the depth axis.

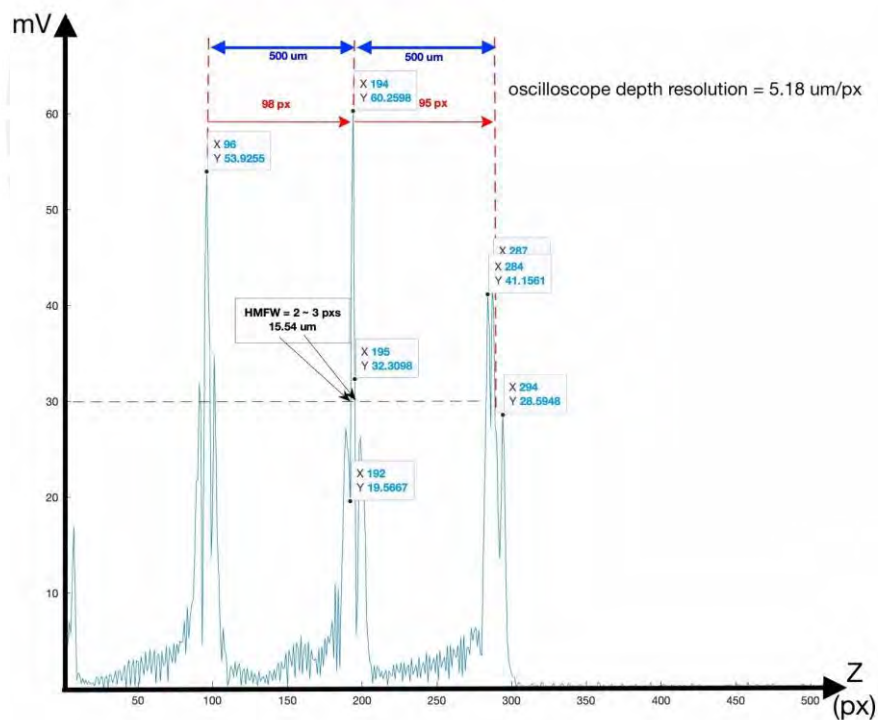


Figure 4.16: The interference signal was captured three times with a separation of 500 μm . The second signal, the one with the higher amplitude, was used for the calculation; the other two were used to calculate the oscilloscope depth resolution.

The axial resolution of the system measured on the system was 15.54 μm .

4.2.6 Axial Depth Range

This procedure determines how deep the system can penetrate in a sample, assuming that the sample tissue will not absorb all the signal power. Using the Depth Characterization procedure, Section 4.2.2, the reference arm is extended until the system limit is reached (Figure 4.13) at 7,900 μm (7.9 mm).

4.2.7 Roll-Off

This procedure calculates how fast the interference signal decays as light beams penetrate the sample. The procedure used in Section 4.2.2 was the basis for this measurement. The information was captured by an oscilloscope and processed by a script.

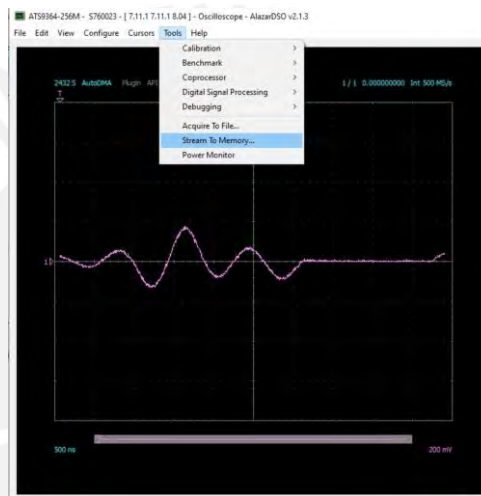


Figure 4.17: A measurement was taken every 500 μm but instead of measuring pixels in the image, the spectrum signal was captured in .csv format using the oscilloscope application provided with the ATS9364 acquisition card and then processed with a MatLab script. All acquired files were named P01 to P16. P00 is a measured taken at the first point, just as P01, but with sample and reference arm covered; this file will be used in a following subsection.

16 measurements were taken in the previous procedure, Depth Characterization. For this procedure, an additional measurement was taken, at the system limit (PLim). In addition, one more measurement was taken, at the starting point, but with reference and sample arms covered; this measurement will be used in the following procedure.

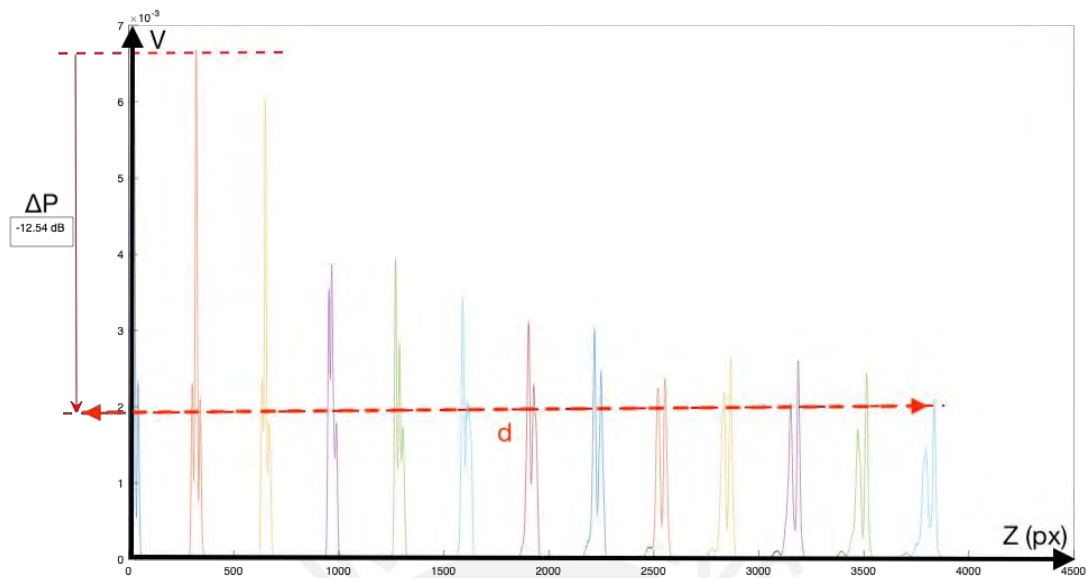


Figure 4.18: Roll-off Chart. 13 measurements are displayed in the chart. The signals with the highest and lower amplitudes were used for the calculation.

To calculate the roll-off value, the following formula is used:

$$\text{Roll-off} = \frac{\Delta P}{d} = \frac{-12.54\text{dB}}{7.5\text{mm}} = -1.672 \frac{\text{dB}}{\text{mm}}$$

- ΔP = Power decay
- d = Maximum axial distance (depth)

4.2.8 Sensitivity - Signal to Noise Ratio (SNR)

The signal-to-noise ratio compares the level of the sampled signal with the background noise. From the Roll-off subsection (4.2.7), the signal-to-noise ratio can be measured at the first point in two steps; the first with reference and sample arms covered and the second with normal conditions.

$$\text{SNR} = \frac{A_{\text{Signal}}}{A_{\text{Noise}}} = 2.3751 \times 10^3 \approx 67.51\text{dB}$$

4.2.9 Optical Power Safety

As every object can only support a maximum optical power, the system must comply with international standards and recommendations. For optical applications, in Table A.3 of IEC 60821-1:2014, Safety of Laser Products, the maximum power for an infrared light laser applied to human eyes is 15.61 mW. Using an optical power meter, the optical power is measured at the sample location.



Figure 4.19: An optical power meter, Thorlabs PM100D, was placed at the Sample arm. The value obtained was 5.33 mW, one third of the allowed power, according to the International Electrotechnical Commission (IEC) recommendation.

4.3 OCT Images

4.3.1 Glass slides

1 Slide Scanning

A single glass slide, used for microscopes, was scanned using a linear scanning pattern.

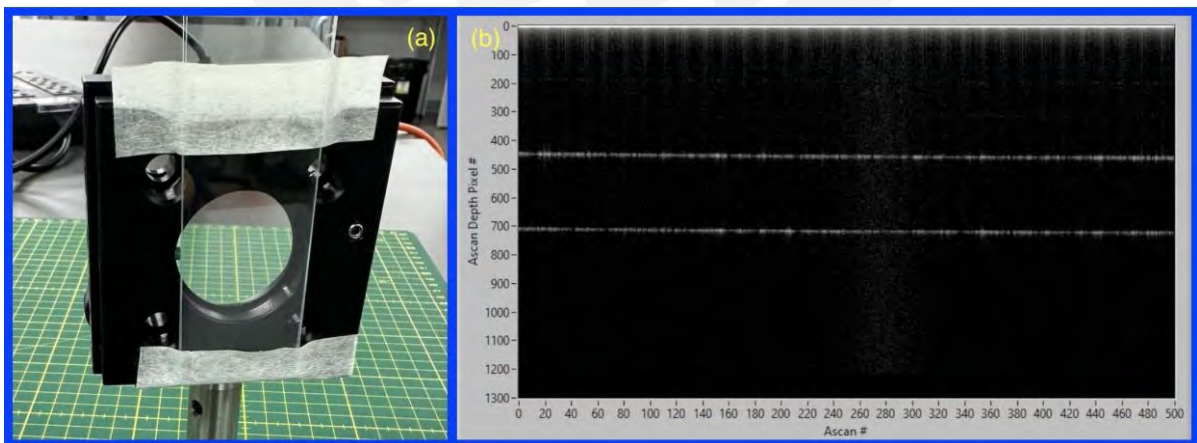


Figure 4.20: Figure (a) shows a glass slide used as sample. A linear scanning pattern was used with 500 A-lines per B-scan. Figure (b) shows the image generated by the system; two lines corresponding to the anterior and posterior surfaces. An amplified view showed the anterior surface located at pixel 400 and the posterior surface located at pixel 660 (depth = 260 px).

From depth characterization:

$$\frac{\mu\text{m}}{\text{px}} = 6.46 \quad \text{and} \quad n_{\text{glass}} = 1.5$$

$$\text{SlideT hickness} = 260 \times 6.46 \div 1.5 = 1,120\mu\text{m} = 1.12\text{mm}$$

2 Slides Scanning

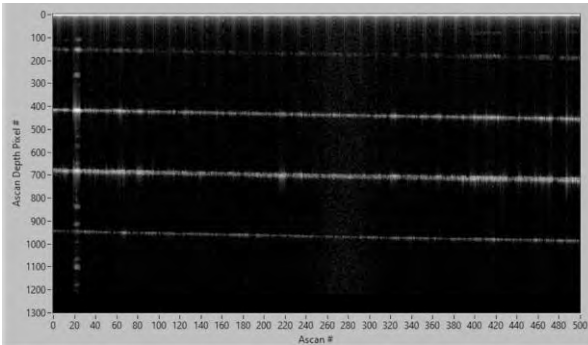


Figure 4.21: Two slides scanned

Figure 4.21 shows the image generated by 2 slides. Three clear lines are visible corresponding to the three interfaces, the anterior surface of the first slide, the union of the two surfaces of the two mirrors, and the posterior surface of the second slide. The first line was located at pixel 410 while the last surface was found at pixel 940, a 530 pixel thickness.

$$2\text{SlidesT hickness} = 2,283\mu\text{m} = 2.28\text{mm}$$

According to the manufacturer, each slide has between 1.0 and 1.2 mm thickness. The refractive index is not specified, so the general 1.5 value was assumed. A measurement with a caliper is provided with a measurement of 1.14 mm for the single slide and 2.29 mm for the two slides.

4.3.2 Synthetic Model Eye

A synthetic (plastic) eye model, Modell-Augen [42], manufactured by Dr. Eva Lakenau, was used as sample.

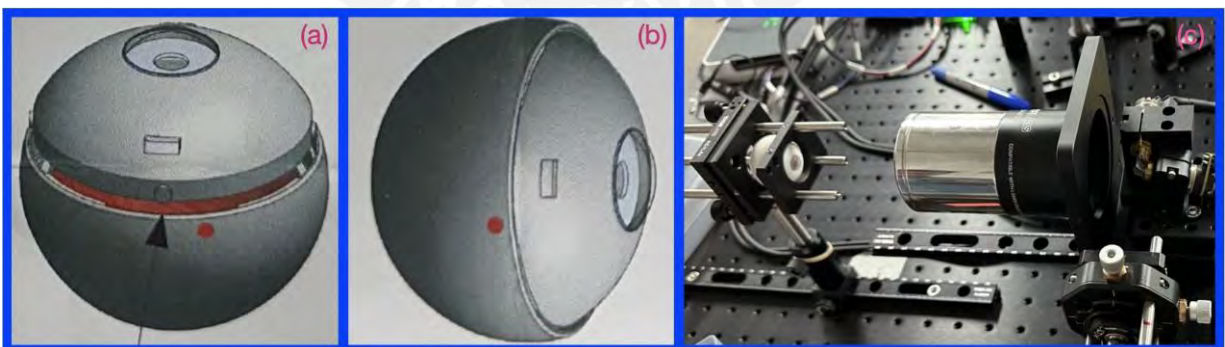


Figure 4.22: Figure (a) shows a synthetic model eye. This model has the same dimensions as a real human eye and can be set to use in normal or diffraction error configuration. Figure (b) shows the eye set in normal configuration facing the scan lens. Figure (c) shows the OCT system scanning the synthetic eye.

Two scan patterns were used to acquire the model images.

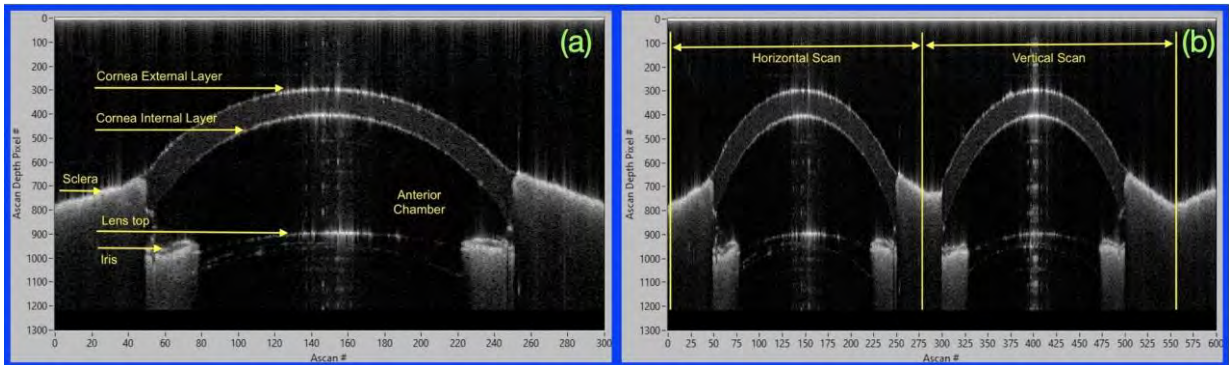


Figure 4.23: Figure (a) shows a linear scan performed on the synthetic eye model. Corneas' outer and inner layers are well defined. The sclera, iris and lens are also displayed. Figure (b) shows a crosshair scan performed to the same sample. Crosshair scan pattern takes two linear scans shifted 90° . These two scan patterns were taken using 300 samples per line. At the center of each eye image, the scattered light becomes stronger, causing the brighter effect.

The manufacturer did not provide dimensions that can be compared with the image generated by the OCT system. However, the shape of the generated image matched that of one image downloaded from the manufacturer's website.

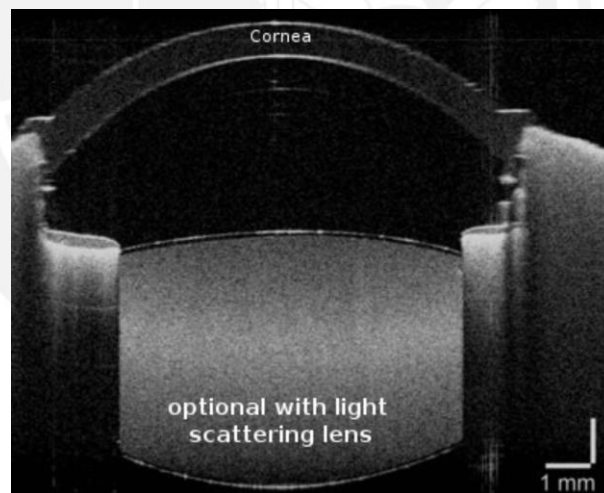


Figure 4.24: OCT image downloaded from the manufacturer's web site. The shape of the cornea matches the shape from Figure 4.23(a) - Image taken from Modell-Augen Manufaktur [42]

Chapter V

Results and Conclusions

5.1 Results

The general objective of this thesis has been achieved. The designed and implemented Swept Source OCT system has been able to scan inorganic samples as well as a synthetic eye model. The characterization procedure provided the system measurement parameters, which are good enough to work with the general objective: generate structural images of ocular and skin tissues.

5.1.1 Requirements

Several papers as well as medical information were used to elaborate requirements that were used to build the system design. The information gathered from medical sources provided limits and parameters for resolution and measurement speed. Information gathered from state-of-the-art technology complemented requirements elaboration.

5.1.2 Design

The design was based on the requirements collected in the previous process. A base design produced scanned images from transparent objects that will accommodate the cornea but not the skin. The final design introduced an interferometry model modification from Michelson-Morley to Mach-Zehnder. This original design only got 50% of the scattered light from the sample. The Mach-Zehnder array increased the sample intensity to almost 100%.

5.1.3 Implementation

The implementation process was conducted without major issues. An important restriction was discovered on the swept laser source; when the emitter received part of the emitted power, as feedback from the reference arm, the laser became inoperative. This issue was solved by adding an optical isolator.

In general terms, the implementation suffered several modifications addressed by the goal of getting a compact and modular system that can be used, in the future, in a medical environment. Optical alignment was performed every time a modification was introduced in the reference and

sample arms. The other components were fiber optic based, which does not require alignment procedures.

As a result of modifications and alignment procedures, the reference arm reduced its length from almost 300 mm to less than half.

5.2 System characterization summary

The implemented system has the following parameters:

5.2.1 Lateral Characterization

From table 4.2 the lateral (horizontal and vertical resolution is provided by the following equation:

$$\text{LatDens} = 2.2R \pm 0.0342$$

where R is the scanning range in millimeters (1 - 15), using 500 samples per range. From the characterization procedure 4.2.4, the lateral resolution value of the system obtained was 35 μm .

5.2.2 Depth (axial) characterization

From table 4.3:

Depth resolution for air ($n = 1.0003$):

$$\frac{\mu\text{m}}{\text{px}} = 6.46 \qquad \frac{\text{px}}{\mu\text{m}} = 0.1547$$

5.2.3 Axial maximum depth

From procedure 4.2.6, in the axial depth range, the maximum penetration the system can achieve is:

$$\text{AxialMaxDepth} = 7.9 \text{ mm}$$

5.2.4 Roll-off

The roll-off characteristic, the rate with which the signal decays, was calculated in the procedure 4.2.7:

$$\text{Roll - off} = -1.672 \frac{\text{dB}}{\text{mm}}$$

5.2.5 Sensitivity - Signal-to-noise ratio (SNR)

The SNR was calculated in the procedure 4.2.8.

$$\text{SNR} = 2.3751 \times 10^3 = 67.51\text{dB}$$

5.2.6 Axial Resolution

From the Light Source, the theoretical axial resolution (ΔZ) is: $\Delta Z = 7.46\mu\text{m}$

From the characterization procedure 4.2.5 the axial resolution value (depth) of the system obtained was $15.54\mu\text{m}$.

5.2.7 Summary Table

Table 5.1: OCT system parameters

Central Wavelength (λ_0)	1,300 nm
Wavelength Swept Range	100 nm
Sweep Rate	200 kHz
Optical power at sample	5.33 mW
Lateral Resolution	$35\mu\text{m}$
Depth Resolution	$6.46\mu\text{m}$
Depth Resolution	$0.1547\frac{\text{px}}{\mu\text{m}}$
Axial Resolution	$15.54\mu\text{m}$
Axial Depth Range	7.9 mm
Roll-off	$-1.672\frac{\text{dB}}{\text{mm}}$
SNR	67.51 dB

5.3 OCT Images

First OCT images were generated using synthetic samples. Glass slides and a synthetic model eye. Using the characterization parameters found in the characterization process, the samples' objects were measured.

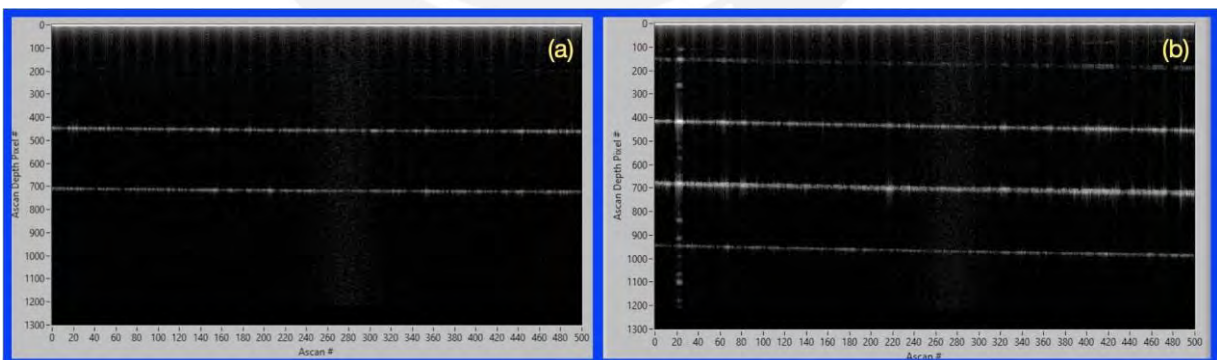


Figure 5.1: Figure (a): One glass slide was measured; using the summary table, its thickness was 1.1 mm. Figure (b): Two glass slides were measured; using the same summary table as on figure (a), the total thickness was 2.2 mm.

5.3.1 Images and dimensions verification

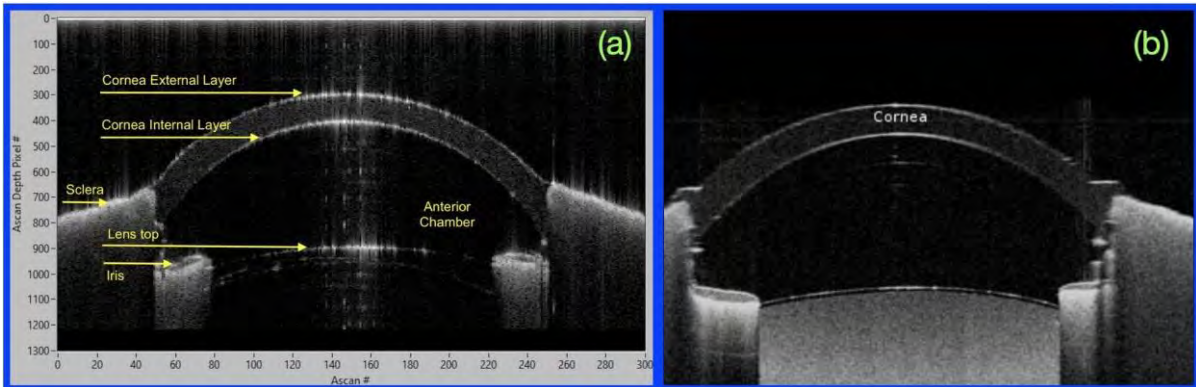


Figure 5.2: Figure (a): OCT system generated image from a scanned synthetic eye model. Figure (b): OCT's image, downloaded from the manufacturer web's site - Image (b) Image taken from Modell-Augen Manufaktur [42].

Lateral and depth characterization provided values that allow for the sizing of the samples. For depth/axial sizing, glass coverslides were used. These elements were also measured with a caliper in order to find their dimensions. An adjustment was also applied on the basis of those comparisons.

For lateral sizing, in addition to the hex keys, there was no other well-known element that could be used to compare its dimensions with the system generated image; that task will be performed in future work. However, the shape of the image formed by the system matches that provided by the manufacturer, generated with the same technique, on its website.

5.4 Discussion

The use of swept source optical coherence tomography to generate medical images, at the moment this document is being written, is well proven and documented. OCT can generate images with better resolution than ultrasound waves, even though it cannot penetrate tissues with the same depth.

However, elastography shows that the biomechanical properties of the keratoconus and skin cancer affected tissue changes before showing structural or morphological modifications.

Combining these two techniques appears to promise a new way to identify keratoconus in the very early stages, allowing patients to start treatment that can stop the disease. For skin cancer patients, identifying false negative cases can also allow patients to start treatment without waiting for a second visual inspection that can take 6 or more months.

5.5 Conclusions

- The objectives set for this thesis have been accomplished designing and implementing an optical coherence tomography system that can generate images with enough resolution to capture tissue details to identify its components.
- The system is able, based on the characterization procedure, to be integrated with an ultrasound elastography module and capture the tissue response to the ultrasound wave excitation.
- All components that were assembled can be redistributed and mounted in a mobile cabinet to be transported for clinical purposes.
- For OCT systems, a Michelson interferometer, with a 50:50 beam splitter, is not a viable configuration due to the intensity of the sampled signal that is lost.

5.6 Future Work

There are some future work that is projected with this system. The most important tasks are as follows:

- Turn the OCT system into an OCE system by integrating an ultrasound elastography module.
- Turn the OCT system from a lab environment into a clinical system
- Repeat the characterization process after any design modification.
- Acquire a precision caliper and a coverslide with a manufacturer-provided refraction index to repeat the characterization process.

In addition to integration of the ultrasound elastography module, some additional projects that can be implemented are as follows:

- Modify the sample arm to be able to scan the retina. This modification requires a different scan lens, but most of the rest of the components remain the same.
- Transform the sample arm into a mobile one. This modification requires the design and printing of a probe that holds the scanning lens and has a scan distance separator.

Bibliography

- [1] John Hopkins Medicine. Keratoconus, 2024. <https://www.hopkinsmedicine.org/health/conditions-and-diseases/keratoconus>.
- [2] INO. Mas de 5,000 trasplantes de cornea realizo el ino, 2023. <https://www.gob.pe/institucion/minsa/noticias/33374-mas-de-5-000-trasplantes-de-cornea-realizo-el-ino>.
- [3] N.Falgayrettes, E.Patoor, F.Cleymand, YZevering, and JM.Perone. Biomechanics of keratoconus: Two numerical studies. *PLOS ONE*, 2023. <https://journals.plos.org/plosone/article/file?id=10.1371/journal.pone.0278455>.
- [4] M.M.Doyley and K.J.Parker. Elastography: general principles and clincial applications, 2014. <https://www.ncbi.nlm.nih.gov/pmc/articles/PMC3896304/>.
- [5] US National Cancer Institute. Skin cancer treatment, 2023. <https://www.cancer.gov/types/skin/patient/skin-treatment-pdq>.
- [6] Natural Eye Care. Human eye parts, 2024. <https://www.naturaleyecare.com/blog/eye-anatomy-disease/>.
- [7] Dupage Optical. Normal vs keratoconus, 2024. <https://www.dupageoptical.com/services/keratoconus/>.
- [8] Trucos de belleza. ¿cómo la piel funciona como un órgano vital para el cuerpo humano?, 2023. <https://trucosdebelleza.net/como-la-piel-funciona-como-un-organo-vital-para-el-cuerpo-humano/>.
- [9] Unisima. Diferencia de los rayos uva y uvb, 2023. <https://unisima.com/salud/radiacion-uva-uvb/>.
- [10] CDC US Centers for Dicease Control and Prevention. Uv radiation ray types, 2023. <https://www.cdc.gov/nceh/features/uv-radiation-safety/index.html>.
- [11] World Health Organization. How common is skin cancer?, 2023. [https://www.who.int/news-room/questions-and-answers/item/radiation-ultraviolet-\(uv\)-radiation-and-skin-cancer](https://www.who.int/news-room/questions-and-answers/item/radiation-ultraviolet-(uv)-radiation-and-skin-cancer).

-
- [12] M.Arnold, D.Singh, M.Laversanne, J.Vignat, S.Vaccarella, F.Meheus, A.E.Cust, E.de Vries, D.C.Whiteman, and F.Bray. Global Burden of Cutaneous Melanoma in 2020 and Projections to 2040. *JAMA Dermatology*, 158(5):495–503, May 2022. <https://jamanetwork.com/journals/jamadermatology/fullarticle/2790344>.
- [13] Prevención y Control de Enfermedades CDC MINSA Peru Centro Nacional de Epidemiología. Cancer distribution in peru 2022 q1, 2023. <https://www.dge.gob.pe/portal/docs/vigilancia/sala/2022/SE37/cancer.pdf>.
- [14] US National Cancer Institute. Melanoma diagnose, 2023. <https://www.cancer.gov/types/skin/patient/melanoma-treatment-pdq>.
- [15] F.Alfageme Roldán. Application of elastography in dermatology, 2016. https://www.esaote.com/uploads/tx_esaotedocuments/WP_Dermatology-Elastography_160000131_V01_LR.pdf.
- [16] Cleveland Clinic. Corneal topography, 2023. <https://my.clevelandclinic.org/health/diagnostics/24819-corneal-topography>.
- [17] Saurabh Kushwaha. Corneal topography, 2020. <https://www.slideshare.net/slideshow/corneal-topography-238992848/238992848#1>.
- [18] B.Yücekul, H.B.Dick, and S.Taneri. Systematic detection of keratoconus in oct: corneal and epithelial thickness maps, 2022. <https://pubmed.ncbi.nlm.nih.gov/35714335/>.
- [19] Roca Perú. Cirrus hd oct, 2023. <https://www.rocaperu.com/uploads/productos/carl-zeiss/tomografo-de-coherencia-optica/cirrus-500/cirrus-5000-smart-scan.pdf>.
- [20] A.Curatolo, J.S.Birkenfeld, E.Martinez-Enriquez, J.A.Germann, G.Muralidharan, J.Palací, D.Pascual, A.Eliasy, A.Abass, J.Solarski, K.Karnowski, M.Wojtkowski, A.Elsheikh, and S.Marcos. Multi-meridian corneal imaging of air-puff induced deformation for improved detection of biomechanical abnormalities. *Biomed. Opt. Express*, 11(11):6337–6355, Nov 2020. <https://opg.optica.org/boe/abstract.cfm?URI=boe-11-11-6337>.
- [21] F. Zvietcovich, J. Birkenfeld, A. Varea, N. Alejandre-Alva, J. Merayo-Llives, and S. Marcos. Human cornea biomechanics and subclinical keratoconus detection using ultrasonic wave-based optical coherence elastography, 06 2023. <https://iovs.arvojournals.org/article.aspx?articleid=2790645>.
- [22] The Skin Cancer Foundation. Abcde annual exam, 2023. <https://www.skincancer.org/early-detection/annual-exams/>.
- [23] C.Niemann, D.M.Owens, P.Schettina, and F.M.Watt. Dual Role of Inactivating Lef1 Mutations in Epidermis: Tumor Promotion and Specification of Tumor Type. *Cancer Research*, 67(7):2916–2921, 04 2007. <https://doi.org/10.1158/0008-5472.CAN-06-3427>.

-
- [24] American Cancer Society. Tests for melanoma skin cancer, 2023. <https://www.cancer.org/cancer/types/melanoma-skin-cancer/detection-diagnosis-staging/how-diagnosed.html>.
- [25] M.Mogensen, T.M.Joergensen, B.M. Nürnberg, H.A.Morsy, J.B.Thomsen, L.Thrane, and G.B.E.Jemec. Assessment of optical coherence tomography imaging in the diagnosis of non-melanoma skin cancer and benign lesions versus normal skin. *DermSurgery Digest*, 35(6):965–972, 2012. <https://doi.org/10.1117/1.JBO.17.12.126006>.
- [26] CH.Liu, S.Assassi, S.Theodore, C.Smith, A.Schill, M.Singh, S. Aglyamov, C.Mohan, and K.V.Larin. Translational optical coherence elastography for assessment of systemic sclerosis. *J. Biophotonics*, 12(12):e201900236, December 2019. <https://www.ncbi.nlm.nih.gov/pmc/articles/PMC7184265/>.
- [27] A.Saad, Y.Lteif, E.Azan, and D.Gatinel. Biomechanical Properties of Keratoconus Suspect Eyes. *Investigative Ophthalmology & Visual Science*, 51(6):2912–2916, 06 2010. <https://doi.org/10.1167/iovs.09-4304>.
- [28] Optical+Biomedical Engineering Laboratory. Introduction to oct. <https://obel.ee.uwa.edu.au/research/fundamentals/introduction-oct/>.
- [29] Y.Lin, D.Li, W.Liu, Z.Zhong, Z.Li, Y.He, and S.Wu. A measurement of epidermal thickness of fingertip skin from oct images using convolutional neural network. *Journal of Innovative Optical Health Sciences*, 14(01):2140005, 2021. <https://doi.org/10.1142/S1793545821400058>.
- [30] Sadaf Afreen. Skin and its histology applied, 06 2024. <https://www.slideshare.net/slideshow/skin-and-it-s-histology-applied-dentistry-pptx/269728274>.
- [31] David Huang, Eric Swanson, Charles Lin, Joel Schuman, William Stinson, Warren Chang, Michael Hee, Thomas Flotte, Kenton Gregory, Carmen Puliafito, and James Fujimoto. Optical coherence tomography. *Science*, 254:1178, 12 1991.
- [32] Joseph A. Izatt, Michael A. Choma, and Al-Hafeez Dhalla. *Theory of Optical Coherence Tomography*, pages 65–94. Springer International Publishing, Cham, 2015.
- [33] F.Zvietcovich and K.V.Larin. Wave-based optical coherence elastography: the 10-year perspective. *Progress in Biomedical Engineering*, 4(1):012007, jan 2022. <https://iopscience.iop.org/article/10.1088/2516-1091/ac4512/meta>.
- [34] F.Zvietcovich, A.Nair, Y.S.Ambekar, M.Singh, S.R.Aglyamov, M.D.Twa, and K.V. Larin. Confocal air-coupled ultrasonic optical coherence elastography probe for quantitative biomechanics. *Opt. Lett.*, 45(23):6567–6570, Dec 2020. <https://opg.optica.org/ol/abstract.cfm?URI=ol-45-23-6567>.
- [35] Caerwyn Ash, Michael Dubec, Kelvin Donne, and Tim Bashford. Effect of wavelength and beam width on penetration in light-tissue interaction using computational methods. *Lasers in Medical Science*, 32, 11 2017. <https://doi.org/10.1007/s00191-017-0600-4>.

[//www.researchgate.net/publication/319652066_Effect_of_wavelength_and_beam_width_on_penetration_in_light-tissue_interaction_using_computational_methods](https://www.researchgate.net/publication/319652066_Effect_of_wavelength_and_beam_width_on_penetration_in_light-tissue_interaction_using_computational_methods).

- [36] Thorlabs. S110 and s113 series mems-vcsel swept sources manual, 2023. <https://www.thorlabs.com>.
- [37] E. Hecht. *Optics*. Pearson Education, Incorporated, 2017. <https://books.google.com.pe/books?id=ZarLoQEACAAJ>.
- [38] ScannerMax. Saturn-1 system - custom. <https://scannermax.com/products/saturn-1-system>.
- [39] Alazartech. Ats9364 - 12 bit, 1 gs/s. <https://www.alazartech.com/en/product/ats9364/661/>.
- [40] National Instruments. Pcie-6738. <https://www.ni.com/en-us/shop/model/pcie-6738.html>.
- [41] GiBio. Biophotonics and biomedical optics research group at pucp, 2024. <https://gibio.pucp.edu.pe>.
- [42] E.Lankenau. Modell-auge manufaktur, 2024. <https://modell-auge-manufaktur.de>.

Appendix I

Component List

Table 0.2: Source Light

Item	Description	Qty	Manufacturer
1	SL132120 Swept-Wavelength Laser Source 1300nm MEMS-VCSEL	1	Thorlabs
2	IO-H-1310APC Fiber Isolator	1	Thorlabs

Table 0.3: Reference Arm

Item	Description	Qty	Manufacturer
3	F260APC Fiber Collimator	1	Thorlabs
4	AC254-100-C Achromatic Doublet	1	Thorlabs
5	PF10-03-P01 Protected Silver Mirror	1	Thorlabs
6	LSM05DC Dispersion Compensating Block for the LSM05	1	Thorlabs
7	AD11F - SM1 Threaded Adapter for Ø11 mm Cylindrical Components	1	Thorlabs
8	CT1A 1/2" Translation Stage for 30 mm Cage Systems	1	Thorlabs
9	CP35 - 30 mm Cage Plate with Ø1" Double Bore	1	Thorlabs
10	KC1/M Kinematic 30 mm-Cage-Compatible Mount for Ø1" Optic	2	Thorlabs
11	ER8-P4 - Cage Assembly Rod, 8" Long, Ø6 mm, 4 Pack	2	Thorlabs
12	ER6-P4 - Cage Assembly Rod, 6" Long, Ø6 mm, 4 Pack	2	Thorlabs
13	PH2-P5 - Ø1/2" Post Holder, 5 Pack	2	Thorlabs
14	TR2-P5 - Ø1/2" Optical Post, SS, 5 Pack	2	Thorlabs

Table 0.4: Sample Arm

Item	Description	Qty	Manufacturer
15	F260APC Fiber Collimator	1	Thorlabs
16	KAD11F - SM1-Threaded Kinematic Pitch/Yaw Adapter for Ø11 mm Cylindrical Components	1	Thorlabs
17	CXY1A - 30 mm Cage System, XY Translating Lens Mount for Ø1" Optics CXY1A	1	Thorlabs
18	LSM05 Scan Lens	1	Thorlabs
19	GAS012 - Scan Lens and Galvo Mirror System Mounting Bracket	1	Thorlabs
20	GAS0123 - Scan Lens Thread Adapter for GAS012 and LSM05	1	Thorlabs
21	ScannerMAX Saturn-1B Full System	1	ScannerMax
22	UBP2/M Universal Base Plate, 65 mm x 65 mm x 10 mm	1	Thorlabs
23	BA2S7 Spacer 2" x 3", 1.000" Thick	1	Thorlabs
24	ER6-P4 - Cage Assembly Rod, 6" Long, Ø6 mm, 4 Pack	1	Thorlabs
25	CP35 - 30 mm Cage Plate with Ø1" Double Bore	1	Thorlabs
26	RLA150/M - Dovetail Optical Rail, 150 mm, Metric	2	Thorlabs

Table 0.5: Interferometer

Item	Description	Qty	Manufacturer
27	TW1300R5A2 - 2x2 Wideband Fiber Optic Coupler	3	Thorlabs
28	CIR-1310-50-APC - OCT Fiber Optic Circulator, 1280 - 1400 nm, SMF, FC/APC	1	Thorlabs
29	Fiber Polarization Controller, 2 Mini Paddles, No Fiber, FPC020	3	Thorlabs
30	PDB480C-AC - Fiber Coupled Balanced Amp. Photodetector, 1.6 GHz, InGaAs, 1300 nm	1	Thorlabs

Table 0.6: Mechanical

Item	Description	Qty	Manufacturer
31	MB7575/M - Aluminum Breadboard, 750 mm x 750 mm x 12.7 mm, M6 Taps	1	Thorlabs
32	ADAF3 - FC/APC to FC/APC Mating Sleeve	15	Thorlabs
33	BA1S/M-P5 - Mounting Base, 25 mm x 58 mm x 10 mm, 5 Pack	3	Thorlabs

Table 0.7: Tools

Item	Description	Qty	Manufacturer
34	VRC2 - VIS/IR Detector Card, 400 - 640 nm, 800 - 1700 nm	2	Thorlabs
35	VRC2CPT -30 mm Cage System Alignment Plate with Visible and IR Disk (400 - 640 nm, 800 - 1700 nm)	1	Thorlabs
36	VRC2SM1 - SM1-Threaded Visible and IR Alignment Disk (400 - 640 nm, 800 - 1700 nm)	1	Thorlabs
37	PM100D - Compact Power and Energy Meter Console, Digital 4" LCD	1	Thorlabs
38	CCHK/M - 9-Piece Color-Coded Hex Key Set, Metric	1	Thorlabs
39	CCHK - 11-Piece Color-Coded Hex Key Set, Imperial	1	Thorlabs
40	DIGC6 - Digital Calipers	1	Thorlabs